Development and assessment of ultra-high performance fibre-reinforced composite panels

by

Shahin Mahdi

Thesis submitted to The University of Adelaide in fulfilment of the requirements for the degree of Doctor of Philosophy

at

The University of Adelaide

Faculty of Engineering, Computer & Mathematical Sciences

School of Civil, Environmental & Mining Engineering

THE UNIVERSITY
of ADELAIDE

January 2022

This thesis is dedicated to my mother and father, Ladan and Zekrollah, for their unyielding

support and devotion

TABLE OF CONTENTS

ABSTRACT

Ultra-high performance concrete (UHPC) is a newly-developed and advanced cementitious material which provides superior strength, durability, and life-span in comparison to conventional concrete. However, under tension it is susceptible to large cracking followed by brittle failure, and this is undesirable in flexural members and frame systems. This is minimised with the addition of steel fibres, resulting in the development of ultra-high performance fibre-reinforced concrete (UHPFRC). UHPFRC provides superior tensile strength and strain hardening properties, and the inclusion of steel fibres provides additional ductility in the post-cracking region, a desirable mechanical property in the design of composite slabs and panels. This thesis presents a collection of journal articles outlining the development and structural assessment of various UHPFRC composite panels jointly with a range of regular and advanced materials.

In the first section of this thesis, the bubble deck and box girder structure systems are used to conceptualise, develop, and produce two new forms of ultra-high performance concrete (UHPC) and ultra-high performance fibre-reinforced concrete (UHPFRC) composite panels for which their structural performance is investigated. An experimental program is performed to observe the one-way bending behaviour of sandwich and box-celled panel systems, and analytical and numerical solutions are established to predict the panel behaviour at the serviceability and ultimate limit states. The section highlights the effectiveness of both systems as viable in structural engineering applications and in particular, the ductility of the box-celled panel.

The second section of the thesis focuses on investigating the feasibility of the box-celled panel system as a wind-resistant structural element. Panels implementing helically ribbed glass fibre-reinforced polymer (GFRP) and steel reinforcement are produced and tested under three-point flexure in both directions to understand the full-range flexural behaviour of the system. The panels display high load capacity and ductility and their behaviour dependent on the reinforcement detail, with GFRP reinforced specimens exhibiting the largest flexural capacity. The results are used to assess the proposed system for compliance with current code provisions for both combined loading actions and permissible deflections when considered a main wind force resisting system (MWFRS). The panels are shown to be efficient as a MWFRS, with load and deflection criteria lying within the elastic region for both flexure directions.

Having observed the reinforcement to be influential on the structural performance of the composite panels, an experimental program is performed to evaluate its bond-slip behaviour within UHPFRC. The behaviour of the helically ribbed GFRP and steel reinforcement embedded in UHPFRC is observed experimentally for various cover conditions and then used in conjunction with existing bond-slip models to develop a multi-variable bond-slip

relationship. The results are compared to the steel reinforcement followed by a parametric study to observe the model variation for its key variables.

The final section of the thesis concentrates on the experimental study of curved and skewed UHPFRC slab systems accompanied by analytical and numerical modelling procedures. Asymmetric and curved slab specimens are cast at various skew and curvature angles and tested under statically indeterminate conditions. Closed-form solutions are developed to predict deflections at the ultimate state, and a thorough finite-element analysis is performed to observe the full-range structural performance. A parametric study is performed to examine the variation of deflection, shear, bending and torsion along the slab length for varying skew and curvature angles. In the section, it is shown that the models can be successfully applied to predict the behaviour UHPFRC asymmetrically skewed and curved slabs.

STATEMENT OF ORIGINALITY

I certify that this work contains no material which has been accepted for the award of any other degree or diploma in my name, in any university or other tertiary institution and, to the best of my knowledge and belief, contains no material previously published or written by another person, except where due reference has been made in the text. In addition, I certify that no part of this work will, in the future, be used in a submission in my name, for any other degree or diploma in any university or other tertiary institution without the prior approval of the University of Adelaide and where applicable, any partner institution responsible for the joint-award of this degree.

I acknowledge that copyright of published works contained within this thesis resides with the copyright holder(s) of those works.

I also give permission for the digital version of my thesis to be made available on the web, via the University's digital research repository, the Library Search and also through web search engines, unless permission has been granted by the University to restrict access for a period of time.

I acknowledge the support I have received for my research through the provision of an Australian Government Research Training Program Scholarship.

LIST OF PUBLICATIONS/MANUSCRIPTS UNDER REVIEW

S. Mahdi, M.S. Mohamed Ali, A. H. Sheikh, M. Elchalakani, and T. Xie. "An Investigation Into the Feasibility of Normal and Fibre-Reinforced Ultra-High Performance Concrete Multi-Cell and Composite Sandwich Panels." *Journal of Building Engineering* (2021): 102728.

S. Mahdi, M.S. Mohamed Ali, A. H. Sheikh, and M. Elchalakani. "Experimental Investigation Into the Structural Behaviour of Ultra-High Performance Fibre-Reinforced Concrete Box-Celled Composite Panels." Submitted to *Composite Structures* (under review).

S. Mahdi, A. H. Sheikh, and M.S. Mohamed Ali. "Experimental investigation on the bond-slip behaviour of helically ribbed GFRP embedded in ultra-high performance concrete." Submitted to *Journal of Composites for Construction* (under review).

M.S. Mohamed Ali, S. Mahdi, A.H. Sheikh, M. Elchalakani, and T. Xie. "Structural performance and analysis of asymmetrically skewed and curved ultra-high performance fibre reinforced concrete slabs." *Engineering Structures* (2021): 113574.

ACKNOWLEDGEMENTS

THIS PAGE HAS BEEN LEFT INTENTIONALLY BLANK

INTRODUCTION AND GENERAL OVERVIEW

Composite structures are an ever-advancing type of structural members spanning over five thousand years, beginning with the development of plywood and straw fibre-reinforced mud by the Mesopotamians (Mehra et al. 2021). The rapid rise of technology has led to the advancement of advanced materials and their structural applications, with one such application being the development of composite panels and slabs. Concrete is by far the most used cementitious material in the world and its recent application to composite slab and panel construction has evolved over the last five decades.

One of these evolutions is the improvement of the mechanical properties of concrete used in the composite construction process, one which brought forward the advent of ultra-high performance concrete in 1972 (Yudenfreund et al. 1972) and subsequent studies by Graybeal (2006) to considerably improve upon initial findings. Ultra-high performance concrete (UHPC) is characterised by a superior strength, durability, and life-span in comparison to conventional concrete. Ultra-high performance concrete attains a compressive strength between 120 MPa to 800 MPa depending on the packing density of the concrete mix (de Larrard and Sedran 1994). However, under tension it is susceptible to large cracking followed by brittle failure, and this is undesirable in flexural members and frame systems. This is minimised with the addition of discontinuous steel fibres, resulting in the development of ultra-high performance fibre-reinforced concrete (UHPFRC). UHPFRC provides superior tensile strength and strain hardening properties, and the inclusion of steel fibres provides additional ductility in the post-cracking region, a desirable mechanical property in the design of composite slabs and panels.

The demand on concrete-based composite panels and slabs are more than ever before, owing to the significant increase in stiffness-to-mass ratios and reduction in dead load. As a result, concrete-based composite slabs and panels are a suitable replacement to reinforced concrete (RC) slabs and walls. The demand to build low-carbon footprint and energy-efficient structures coupled with the benefits of concrete-based composites and advantages of UHPFRC highlights a necessity to study the design of structurally- and energy-efficient single- and multi-layer UHPFRC composites panels and slabs for their application in multi-story buildings and bridge deck structures.

The box girder and bubble deck systems are systems which are widely used in the construction industry due to their high load bearing capacity, torsional rigidity, and significant reduction of excess cementitious material, all of which are highly advantageous characteristics for designing composite slabs. Neither system has been investigated as a pre-cast panel system, hence there is a need to assess their feasibility and structural behaviour for developing new lightweight composite panel systems.

Skewed and curved decks are also of importance due to the rapid increase of cantilevered slabs for floors and balconies of multi-storey buildings, and bridges of curved and skewed nature of high space limitation and mountainous regions. Due to their geometry, skewed and curved slabs are susceptible to multiple modes of failure, and are typically steel RC decks. However, the large annual maintenance costs of RC bridge decks exceed $13 billion dollars (NACE International 2020), and the economic impact and subsequent safety concerns have focused research towards developing bridge decks and slabs with prolonged lifespans for which

UHPFRC can satisfy. Neither skewed nor curved UHPFRC composite slabs have been investigated for this purpose and are therefore imperative to explore their feasibility for.

The objectives of this thesis are to:

- Design, produce, and test two new UHPC and UHPFRC composite pre-cast panels using the box girder and bubble deck systems in an experimental,

- Perform both analytical and numerical analyses to assess both panels at the serviceability and ultimate limit states,

- Identify the most effective of the two systems and further improve the structural efficiency of the panel in an experimental study,

- Assess the feasibility of the panel as a main wind force resisting system (MWFRS),

- Better understand the bond behaviour of the reinforcement used in the panel systems, and

- Investigate the use of UHPFRC in the development of asymmetrically and curved composite slabs.

This thesis is a compilation of manuscripts that are published or under review in internationally recognised journals. Each chapter is a presentation of each manuscript for which each chapter addresses the above objectives. The chapters are in the following format: a background statement, addressing the objective of the chapter and the manuscript that accomplishes those objectives, the statement of authorship which highlights the contributions made by each other, and lastly the manuscript.

The first chapter of the thesis focuses on the conceptualisation, development, and production of two new forms of ultra-high performance concrete (UHPC) and ultra-high performance fibre-reinforced concrete (UHPFRC) composite panels. An experimental program is performed on six panel specimens to observe the one-way bending behaviour. Three UHPC-FRP based bubble deck sandwich panel and three box-celled UHPC-steel profile panel specimens of varying configurations are fabricated and tested under three-point flexure. In addition to the experimental investigation, analytical studies are undertaken where two methods, namely elementary sandwich panel theory (EST) and advanced sandwich theory (AST), are applied at the serviceability limit state, whereas a segmental sectional analysis is implemented to predict the box-cell panel behaviour at the serviceability limit state. Additionally, finite-element analyses are performed to the box-cell panels to simulate their elastic and inelastic structural performance. The chapter highlights the effectiveness of the box-cell composite panel and is identified as the system to further improve upon to meet the research objectives.

The second chapter of the thesis explores the enhancement of the box-celled composite panel from the outcomes found in the previous chapter for its purpose as a wind-resistant structural panel. Six box-celled UHPFRC composite panels with varying arrangements of reinforcement are fabricated and subjected to monotonically increasing loads at their mid-spans. A thorough assessment of their flexural and deflection capacities by code provisions of renowned design standards are performed to assess the suitability of the panel system as a wind-resistant structural panel. The panels are shown to be efficient as a MWFRS, with load and deflection criteria lying within the elastic region for both directions of flexure. The most effective section arrangement based on the code provision criteria, failure behaviour, and strength-to-weight ratio determined in the study is with the addition of helically ribbed GFRP reinforcement to the panel.

The third chapter of the thesis studies the performance of helically ribbed GFRP as an effective form of reinforcement when embedded in UHPFRC. An experimental program is performed to evaluate its bond-slip behaviour within UHPFRC. Seven helically ribbed GFRP reinforcement specimens in addition to seven high-strength steel reinforcement specimens, are cast in varying locations within a UHPFRC block and tested under pull-out conditions. The local bond-slip relationships of the GFRP and steel specimens are experimentally evaluated, and existing theoretical models are assessed to develop a new multi-variable bond-slip model for helically ribbed GFRP embedded in UHPC. The results are compared to the steel reinforcement and then a parametric study is performed to observe the model variation for its key variables.

The fourth chapter of the thesis explores the feasibility of UHPFRC as a material used in the production of curved and skewed UHPFRC slabs. Two asymmetrically skewed slabs with skew angles of 25° and 45° and two horizontally curved slabs with curvature angles of 60° and 90° are fabricated and subjected to concentrated loading at several locations along the slab length. In addition to the experimental program, closed-form solutions based on the method of virtual work and Castigliano's second theorem are established to predict support reaction forces and mid-span deflections of the skewed and curved slabs within the linear elastic state. Additionally, closed-form solutions are developed based on yield-line theory in tandem with a mechanics-based moment-rotation model to predict deflections at the ultimate state, and a thorough finite-element analysis applying non-linear material and damage modelling is accomplished to obtain the full-range behaviour of the slabs. Lastly, a parametric study is performed to assess the effects of skew and curvature angle on deflection, shear, bending and torsion along the slab lengths. The generic analytical procedures and finite-element model are

compared against experimental results obtained from the study and results show that the models can be applied to UHPFRC asymmetrically skewed and curved slabs.

The final chapter of the thesis presents concluding remarks and recommendations for future research to outcomes in the thesis. Possible extensions explored include the interfacial bond action between screw anchors and UHPC/foam layers in the proposed box-celled composite panels as well as the behaviour of box-celled UHPFRC multi-cell panels under combined actions and structural performance under different support conditions.

REFERENCES

de Larrard, F., & Sedran, T. (1994). "Optimization of ultra-high-performance concrete by the use of a packing model." *Cement and concrete research*, 24 (6), 997-1009.

Graybeal, B. A. (2006). "Material property characterization of ultra-high performance concrete (No. FHWA-HRT-06-103)." *United States. Federal Highway Administration. Office of Infrastructure Research and Development.*

Mehra, A. K., Saini, R., & Kumar, A. (2021). "The effect of fibre contents on mechanical and moisture absorption properties of gourd sponge/coir fibre reinforced epoxy hybrid composites." *Composites Communications*, 25, 100732.

NACE International, Highway and Bridges. https://www.nace.org/resources/industries-nace-serves/highways-bridges, 2020 (accessed 24 October 2021).

Yudenfreund, M., Odler, I., & Brunauer, S. (1972). "Hardened portland cement pastes of low porosity I. Materials and experimental methods." *Cement and Concrete Research*, 2 (3), 313-330.

THIS PAGE HAS BEEN LEFT INTENTIONALLY BLANK

CHAPTER 1

Background

In this chapter, the bubble deck and box girder structural systems are used to conceptualise, develop, and produce two new forms of ultra-high performance concrete (UHPC) and ultra-high performance fibre-reinforced concrete (UHPFRC) composite panels for which their structural performance is investigated. An experimental program is executed to observe the flexural behaviour of the sandwich and box-celled panel systems, and analytical and numerical models are established to predict the panel behaviour at the serviceability and ultimate limit states.

List of manuscripts

Mahdi, S., Ali, M. M., Sheikh, A. H., Elchalakani, M., & Xie, T. (2021). "An Investigation Into the Feasibility of Normal and Fibre-Reinforced Ultra-High Performance Concrete Multi-Cell and Composite Sandwich Panels." *Journal of Building Engineering*, 102728.

Statement of Authorship

Title of Paper	An Investigation Into the Feasibility of Normal and Fibre-Reinforced Ultra-High Performance Concrete Multi-Cell and Composite Sandwich Panels
Publication Status	☑ Published ☐ Accepted for Publication ☐ Submitted for Publication ☐ Unpublished and Unsubmitted work written in manuscript style
Publication Details	Mahdi, S., Ali, M. M., Sheikh, A. H., Elchalakani, M., & Xie, T. (2021). "An Investigation Into the Feasibility of Normal and Fibre-Reinforced Ultra-High Performance Concrete Multi-Cell and Composite Sandwich Panels." *Journal of Building Engineering*, 102728.

Principal Author

Name of Principal Author (Candidate)	Shahin Mahdi
Contribution to the Paper	Conceptualisation, methodology, model development, and manuscript writing and revision
Overall percentage (%)	50
Certification	This paper reports on original research I conducted during the period of my Higher Degree by Research candidature and is not subject to any obligations or contractual agreements with a third party that would constrain its inclusion in this thesis. I am the primary author of this paper.
Signature		Date	29/12/2021

Co-Author Contributions

Name of Co-Author	Mohamed Sadakkathulla Mohamed Ali
Contribution to the Paper	Supervision, conceptualisation, methodology, and manuscript revision (25%)
Signature		Date	29/12/2021

Name of Co-Author	Abdul Hamid Sheikh
Contribution to the Paper	Supervision, methodology and manuscript revision (15%)
Signature		Date	29/12/2021

Name of Co-Author	Mohamed Elchalakani		
Contribution to the Paper	Conceptualisation and manuscript revision (5%)		
Signature		Date	29/12/2021

Name of Co-Author	Tianyu Xie		
Contribution to the Paper	Data curation and model development (5%)		
Signature		Date	29/12/2021

An Investigation Into the Feasibility of Normal and Fibre-Reinforced Ultra-High Performance Concrete Multi-Cell and Composite Sandwich Panels

S. Mahdi[1*], M.S. Mohamed Ali[2], A.H. Sheikh[3], M. Elchalakani[4], T. Xie[5]

[1]Mr. Shahin Mahdi (Corresponding author)
Ph.D. Candidate
School of Civil, Environmental and Mining Engineering
The University of Adelaide
South Australia 5005
AUSTRALIA
Email: shahin.mahdi@adelaide.edu.au

[2]Dr. Mohamed Sadakkathulla Mohamed Ali
Senior Lecturer
School of Civil, Environmental and Mining Engineering
The University of Adelaide
South Australia 5005
AUSTRALIA
Email: mohamed.mohamedsadakkathulla@adelaide.edu.au

[3]Associate Professor Abdul Hamid Sheikh
Associate Professor
School of Civil, Environmental and Mining Engineering
The University of Adelaide
South Australia 5005
AUSTRALIA
Email: abdul.sheikh@adelaide.edu.au

[4]Dr. Mohamed Elchalakani
Senior Lecturer
School of Civil and Infrastructure Engineering
The University of Western Australia
Perth 6009
AUSTRALIA
Email: mohamed.elchalakani@uwa.edu.au

[5]Dr. Tianyu Xie
Research Assistant
School of Civil and Infrastructure Engineering
RMIT University
Melbourne 3000
AUSTRALIA
Email: anson.xie@rmit.edu.au

An Investigation Into the Feasibility of Normal and Fibre-Reinforced Ultra-High Performance Concrete Multi-Cell and Composite Sandwich Panels

S. Mahdi[1*], M.S. Mohamed Ali[2], A.H. Sheikh[3], M. Elchalakani[4], T. Xie[5]

ABSTRACT

Inspired by the concept of box girders and bubble deck systems, the present study investigates and develops new forms of composite structures and their behaviours are investigated. The sandwich system implements two basalt fibre-reinforced polymer (BFRP) mesh reinforced ultra-high performance concrete (UHPC) plates as face sheets and a combination of normal strength mortar (NSM) and expanded Polystyrene (EPS) foam as core layers in varying configurations. The box-cell system is produced by UHPC cast into galvanised steel roofing sheet profiles with anchor screws and EPS foam positioned in-situ to produce a box-celled panel. Both systems have three variations for which the structural responses of these panels as one-way slabs under three-point flexure are studied. In addition to the experimental investigations, the sandwich panel theory (EST), advanced sandwich theory (AST), segmental sectional analysis and finite-element analysis are applied to predict the behaviour of the panels at their serviceability limit states. The findings indicate that partially replacing the core with EPS in the sandwich system can effectively reduce the self-weight of the slab without compromising its load capacity under flexure. Moreover, the box-cell system is the most effective when steel fibres are added to the UHPC mix by increasing ductility and preventing early delamination of the steel profile from the UHPC. The modified EST, AST, and sectional analysis can successfully simulate the behaviour of the composite panels within their linear elastic material conditions and the finite-element analysis can accurately model the full-range behaviour of the box-cell composite panels.

1. INTRODUCTION

The ever-increasing demand of innovative and efficient construction of multifunctional buildings requires designs which are energy-efficient and beneficial for a sustainable built-environment with a low-carbon footprint. Based on the current statistics alone, the construction, operation and maintenance of buildings are responsible for 50% of the global energy consumption and greenhouse gas emissions worldwide [1]. To address these issues, there is an increasing focus for the research on the construction of energy and structurally efficient composite structures.

Typically, a sandwich panel is constructed using two face sheets to encase or sandwich an inner, comparatively lighter insulating layer referred to as a core. This results in a stiff, light and efficient structural element, capable of being used in multi-unit residential, commercial and bridge-deck construction [2]. Traditionally, reinforced concrete layers are utilised as the face sheets in a sandwich panel system to maintain the load bearing capacity and conversely, a light material such as expanded polystyrene (EPS) foam is adopted to achieve [3, 4]. As widely recognised, precast sandwich panels are sustainable, convenient for construction and can also reduce fabrication and transportation costs [5, 6], and thus have attracted considerable attention with regards to research and development over the last few decades.

Box girder deck slab systems for bridges are efficient in optimising the self-weight of the structures whilst maintaining a comparatively high load bearing capacity and a higher torsional

rigidity [7]. In recent times the box girder deck slab concept has been extended for the construction of box-cell panels. The removal of excess cementitious material which creates the boxed shape for box-cell panels has a minimal effect on the section strength, as the major flexural compression and tension stresses occur in the top and bottom flange regions, and thus makes the box-celled structures effective for resisting both sagging and hogging bending moments [8]. In bubble deck systems, shown in Fig. 1, the core layer is fabricated by eliminating superfluous cementitious material and replacing it with hollow EPS foam balls and this has been extensively researched in construction of roofing systems and structural deck slabs [9-11]. The major advantage of this system is the reduction of volume of concrete about 50% in comparison to a standard slab without compromising the flexural strength [12]. Both box girder and bubble deck slab configurations have not been adopted for constructing composite precast panel systems and hence there is a need to investigate their structural behaviour for the development of new lightweight composite panel systems.
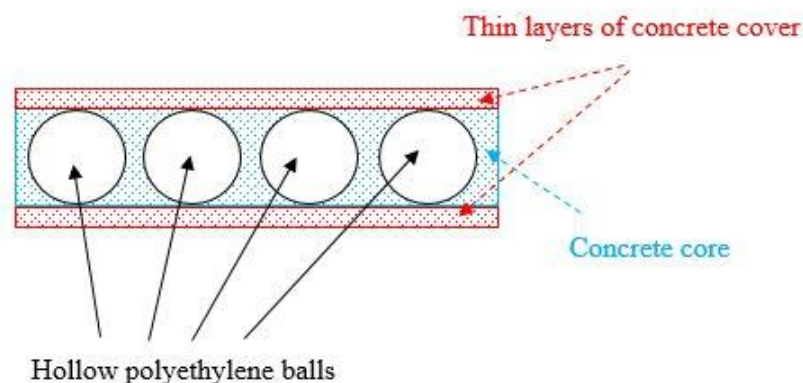

Figure 1 – Bubble deck system.

Cementitious materials such as normal strength concrete (NSC) and normal strength mortar (NSM) are prevalent in the design and construction of composite panel design. However, NSM and NSC both have mechanical disadvantages such as low tensile strength and comparatively

14

low compressive strength. Therefore, there is a need to improve the mechanical properties of the cementitious material or provide appropriate reinforcement in the tensile region in designing composite panels, and this has given rise to the development of ultra-high performance concrete (UHPC). UHPC provides superior compressive strength, larger tensile ductility and better durability [13-15]. Previous studies [16-18] have investigated the mechanical advantages of UHPC using more refined materials and manufacturing methods, whereas recent research focuses on refining UHPC mix designs using conventional materials and manufacturing methods [13, 14, 19-21]. Recent investigations on UHPC has diverged towards minimising its mechanical disadvantages through the addition of steel fibres, resulting in the development of ultra-high performance fibre-reinforce concrete (UHPFRC). Regarded as an advanced cementitious material and although denser than UHPC, UHPFRC in comparison provides superior tensile strength, ductility and strain hardening characteristics [22]. The presence of the steel fibres also provides higher ductility in the post-cracking behaviour as microcracks in the UHPC are bridged by the fibres and this minimises crack widths in the tensile region [23-25]. Additionally, the presence of steel fibres provides higher ductility in compression [26], and these properties are desirable in designing one-way composite panels.

Steel and fibre reinforced polymers (FRP) are commonly used materials in the tensile reinforcement of cement/concrete based composite. Both steel and FRP reinforcement are superior in tensile strength and provide high bond strength to resist reinforcement slip in the tensile region. However, FRP reinforcement failure is brittle and composite panels which use FRP will have little ductility whereas steel in composite panels provide significant ductility. Design of composite panels typically use tensile reinforcement in the interior of the structure, however composite panel design has transitioned to using steel as a layer in the composite

15

panel. Profiled steel sheets in composite panel construction are advantageous as it can be used as permanent formwork for in-situ casting and act as tensile reinforcement for slabs and panels under flexure without having to provide interior reinforcement [27]. Subsequently, the load capacity of a composite panel is governed by the bond strength between the layers of the composite panel and determines whether the panel will fail in a brittle or ductile mode [28].

In the present study, six new panels were developed with a focus on studying the advantages of UHPC and UHPFRC in box-cell and sandwich panel design. Three UHPC-FRP based sandwich panels and three box-celled UHPC-steel profile composite panels of varying configurations were fabricated and tested under flexure. In addition to the experimental investigations, analytical studies were undertaken, where two classical methods namely elementary sandwich panel theory (EST) and advanced sandwich theory (AST) for simulating the behaviour of sandwich panels at the serviceability limit state, were applied with further modifications to accommodate the effects of composite core materials, whilst a segmental sectional analysis was used to simulate the serviceability limit state of box-cell panels. Additionally, finite-element analyses were performed to the box-cell panels to simulate their elastic and inelastic structural performance.

2. EXPERIMENTAL PROGRAM

2.1. Panel design principles

The new composite systems were developed to maintain the load bearing capacity and ductility, reduce the self-weight and tendency of corrosion of the structural elements under extreme environments and enable a quick and economical process of construction. The experimental

program has been devised to evaluate the structural performance of three different types of panel configurations for the sandwich and box-cell panel systems.

2.2.   One-way slab test specimens

2.2.1. *Slab configurations*

Figs. 2 (a) to (e) illustrate the configurations and components of the sandwich and box-cell panel systems investigated in the present study. The panels were designed as one-way slabs, with the sandwich panel dimensions of 1500 mm × 720 mm × 70 mm with a clear span of 1440 mm, and box-cell panel dimensions of 1500 mm × 700 mm × 70 mm with a clear span of 1420 mm.
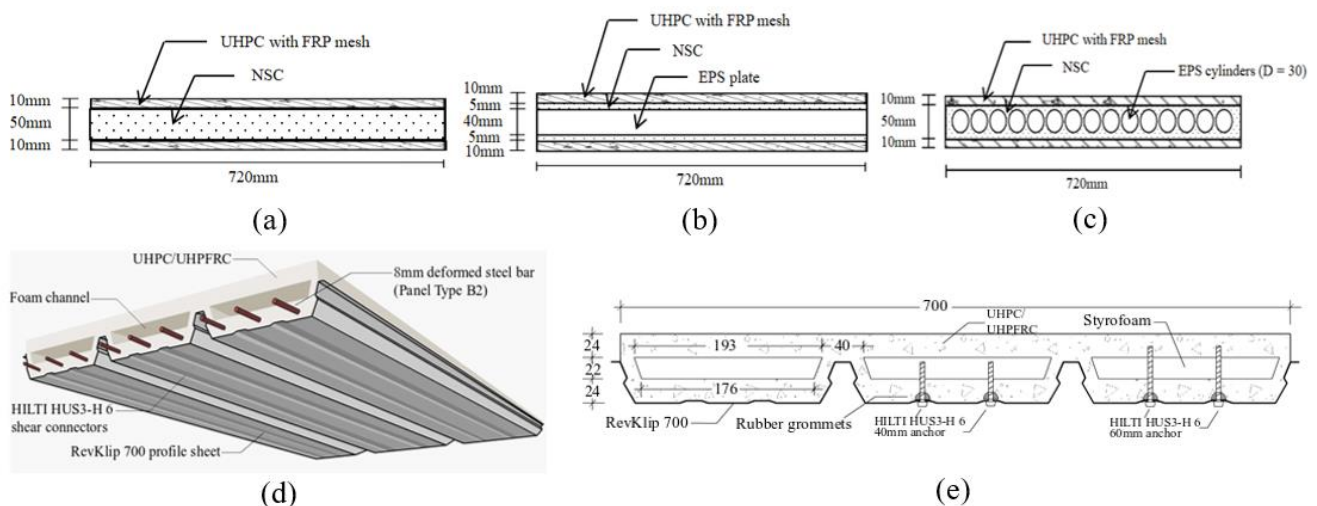
Figure 2 - Slab configurations: a) AI section arrangement; b) AII section arrangement; c) AIII section arrangement; d) Type B panel arrangement; and (e) Type B section arrangement.

The sandwich panel top and bottom face sheets were all basalt FRP (BFRP) mesh reinforced UHPC composite panels of 10 mm thickness with differing configurations of the core materials utilised. Note that within each face sheet, the BFRP mesh was embedded within the centre of the UHPC plate. For specimen AI, the core material was purely C30 grade normal strength

17

mortar (NSM). Specimens AII and AIII panel cores were constructed by combining expanded Polystyrene (EPS) foam and NSM in different configurations. As reported in Shams et al. [29], owing to excessive tensile stress exerted in the adhesive zone, the delamination between the face sheets and the core materials (particularly due to the smooth surface of EPS foam) tends to occur. To address this shortcoming, when designing AII and AIII panels, the NSM was used as a bulking agent as well as a shear connector between the core and face sheets to integrate with the EPS materials and to prevent premature delamination between the face sheets and core. An EPS foam board (Fig. 3 (a)) was used in specimen AII panel with drilled holes of 40 mm diameter and at 120 mm spacing to allow the bulking agent (i.e. NSM) to penetrate through. Instead of using an EPS form board, EPS cylinders (Fig. 3 (b)) were adopted for specimen AIII. These cylinders are 30 mm in diameter and 1440 mm in length, which were placed horizontally along the length of the panel to partially replace the NSM. As shown in Figs. 2 (b) and (c), the top and bottom of the EPS materials were covered by a 5 mm layer of NSM and the bond between NSM and BFRP mesh reinforced UHPC face sheets was achieved using a highly flowable two-component mortar-based solvent free epoxy resin adhesive which offers an adhesive bond shear strength of over 4 MPa without reacting with cementitious materials (i.e. UHPC or NSM).
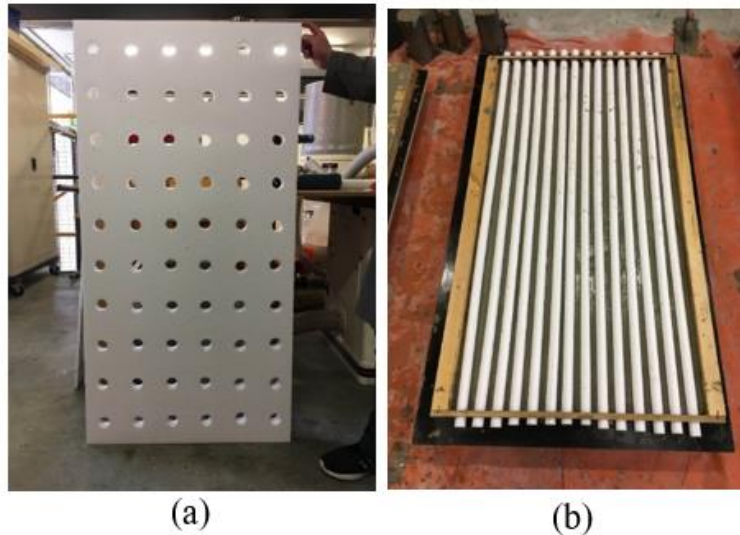
Figure 3 - Differing configurations of EPS foam in the core layer: a) EPS foam board with drilled holes; and b) horizontally placed EPS foam cylinders.

A prefabricated steel profile was used for the box-cell panels as the profile allowed enough cover on the top and bottom to allow for the placement of reinforcement within the mix (specimen BII), and for the reduction of possible flowability issues in the crevices of the cast sections. The section was proportioned into three sections based on the placement of the EPS trapezoidal prisms; the upper layer of 24 mm thickness, the central layer (where the EPS prisms are cast) of 22 mm thickness, and the bottom layer of 24 mm thickness. To enable the combined action of the cementitious portion of the slab and steel profile, 40 mm screw anchors were drilled through the roof sheet prior to pouring with 60 mm screws to anchor the foam further at centre-to-centre spacings of 564 mm. The thread of the screw anchor provided the necessary bond strength post-curing of the UHPC/UHPFRC. For the reference specimen (specimen BI), the cementitious material was purely UHPC with no added reinforcement. For the BII panel specimen, 9 steel deformed bars of 8 mm in diameter were placed in the bottom layer, or trenches, of the UHPC portion of the box-cell panel (Figs. 2 (d) and (e)). Three bars were placed

in each trench, at centre-to-centre spacings of 42 mm. The panel BIII was built with the same sectional configuration as panel BI but UHPC was replaced with UHPFRC.

2.2.2. *Manufacturing process of the panel systems*

To facilitate the fabrication of the panels, each of their components including the face sheets, EPS foam for the differing configurations and systems, steel profile and screw anchors, UHPC, UHPFRC and NSM were prepared individually and then assembled.

For the sandwich panels (specimens AI, AII, and AIII), a layer of UHPC of about 5 mm thickness was initially poured into the formwork and then the top surface was evenly levelled. Following the placement of the BFRP mesh, another 5 mm layer of UHPC was poured over the BFRP mesh to complete the construction process of one face sheet. This process ensured that the BFRP mesh remained in the centre of the panel. The core layer prepared for the control specimen (panel AI) was simply cast using a 1500 mm $\times$ 720 mm $\times$ 50 mm NSM slab. When preparing the core layers for the remaining sandwich panels (panels AII and AIII), an intermediate layer of NSM with 5 mm thickness was initially poured into the formwork. Following this, either EPS foam board with drilled holes or EPS foam cylinders were carefully placed on the top of the NSM layer and the rest of NSM was subsequently poured over. Like the BFRP mesh within the UHPC face sheet, this process ensured the EPS cylinders and board remained in the centre of the NSM layer. Due to the excellent flowability of the NSM prepared, only gentle vibrations were applied to ensure a perfect bonding of NSM layer with EPS foam. After 28-day casting, the prefabricated components including the face sheets and cores were glued together using the epoxy resin adhesive. The specimens were additionally cured for another 7 days under ambient conditions to allow enough time for the bond strength to develop.

For the box-cell panels (specimens BI, BII, and BIII), the steel profile sheets were prepared by drilling 40 mm screw anchors at 94 mm increments along the length of the profile, specifically placed through the trough sections. Additionally, 60 mm screw anchors were placed at 564 mm increments (replacing 40 mm anchors), to ensure that the foam remains anchored during the pouring process (Figs. 2 (d) and (e)). Once the concrete hardened, the thread of the screw provided necessary bonding between the concrete and steel. Rubber grommets were fitted to each screw to maintain the screws remained in an upright position and ultimately to ensure there was a seal and no possibility of seepage from the hole created through the perforation of the profile via the screw anchor. The steel profile was too thin to bear the UHPC/UHPFRC on its own as formwork, therefore additional formwork was prefabricated to help support the roof sheet from underneath during the curing process. Once the concrete mix was ready, it was poured inside the preconstructed timber/steel profile formwork to a thickness of approximately 24 mm to produce the bottom layer. The EPS trapezoidal prisms were then placed on top of the bottom layer of concrete and locked in place by the screw anchors, with the longer screw anchors placed to prevent the EPS prisms from producing a camber due to the uplift caused by the poured concrete. Once the EPS prisms were secured, the remaining concrete was poured into the formwork up to a height of approximately 70 mm, forming both the central and upper layers of the panel. The panels were allowed 28 days under ambient conditions to cure before demoulding.

2.2.3. *Test setup and instrumentation*

The three sandwich panels were tested as one-way slabs and each of them was simply supported at each short edge and the load was applied at the mid-span of each slab through a heavily stiffened spread steel beam, as shown in Fig. 4. To measure the deflections of each slab, a total

of four LVDTs were used, including three placed underneath each of the slabs and another one mounted on the loading ram to measure its vertical displacement (Fig. 4).

Figure 4 - Sandwich panel test elevation.

Furthermore, specimen BI was tested under simply supported conditions at the short edges but with a circular patch load applied through a 115 mm diameter spherical seat, whereas the other two specimens (specimens BII & BIII) were tested similarly but the load was applied at the middle span of each slab through a steel I-beam, as shown in Fig.5. To measure the deflections of each slab, an LVDT was mounted on the loading ram and 8 laser sensors were placed (3 at the quarter and three-quarter spans, and 2 at the midspan), as can be seen in Fig. 5. Additionally, strain gauges were bonded to the top and bottom surfaces of the slabs.
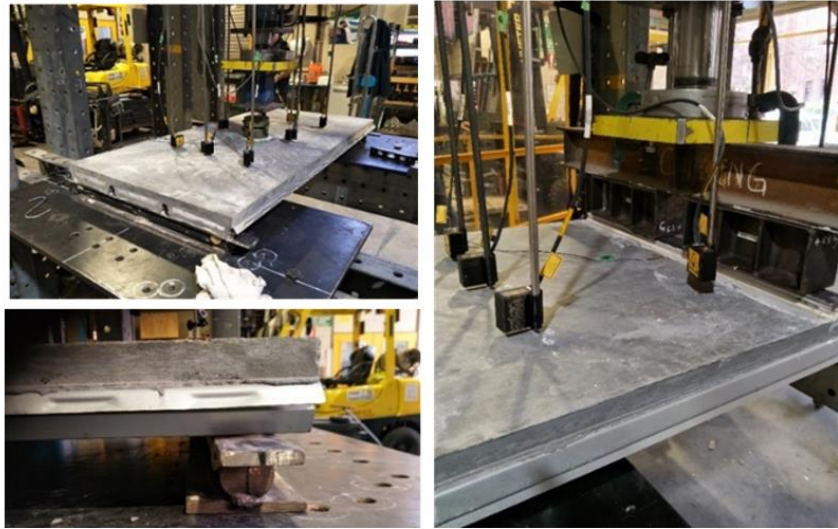
Figure 5 - Box-cell panel test elevation.

A universal testing machine with 1000 kN load capacity was used to apply monotonically increasing load at the mid-span of each of the slabs at a rate of 5 kN/min until the peak load was attained and thereafter the loading was transitioned to displacement control at a displacement rate of 0.1 mm/min until failure in order to obtain the complete load-defection relationship.

2.3. Testing of material properties

2.3.1. *Compression tests*

The mix proportions of the separate UHPC batches, UHPFRC and NSM are summarized in Table 1.

Material	Sulfate Resistant Cement (kg)	Silica Fume (kg)	Sand (kg)	Water (kg)	Superplasticiser (kg)	Steel fibre (kg)	*w/b* ratio	*w/c* ratio
UHPC (for Type A panels)	0.79	0.21	1.00	0.12	0.06	-	0.12	0.152
NSM	0.8	-	1.28	0.4	-	-	0.5	0.5
UHPC (For specimens BI & BII)	1	0.226	1	0.19	0.045	-	0.155	0.19
UHPFRC (For specimen BIII)	1	0.226	1	0.19	0.045	0.165	0.155	0.19

Table 1 – Mix proportions of cementitious materials.

The UHPC mix designs used for the sandwich (UHPC1) and box-cell panels (UHPC2) vary due to a change in the cement manufacturer. The cement used for the manufacturing of box-cell panels were of an equal parts mix of Portland clinker and granulated blast furnace slag whereas the cement used for the sandwich panels used a much lower proportion of slag.

To obtain the compressive stress-strain relationships of the UHPC, UHPFRC and NSM, uniaxial compression tests were conducted on cylindrical specimens with 75 mm diameter and 150 mm height as per ASTM C469/C469M-14 [30]. The compressive behaviour of EPS foam was obtained using 75 mm cubic specimens. The results of the cylinder tests and compressive stress-strain curves of the UHPC, UHPFRC, NSM and EPS foam are shown in Table 2 and Figs. 6 (a) and (b).

Mixture	Specimen	Peak Load (kN)	Compressive strength, f'_c (MPa)	Mean	Standard Deviation	Coefficient of Variation
UHPC1	B1C1	510.5	114.9	116.1	2.93	0.0256
	B1C2	503	113.3			
	B1C3	535.5	120.2			
UHPC2	B2C1	443.5	99.1	100.8	4.22	0.0419
	B2C2	467.5	105.8			
	B2C3	441	99.3			
	B2C4	473	107.1			
	B2C5	436	98.2			
	B2C6	421	95.3			
UHPFRC	B3C1	493	111.0	109.9	3.01	0.0273
	B3C2	470	105.8			
	B3C3	503	113.0			

Table 2 – Cylinder compression test results for UHPC and UHPFRC.
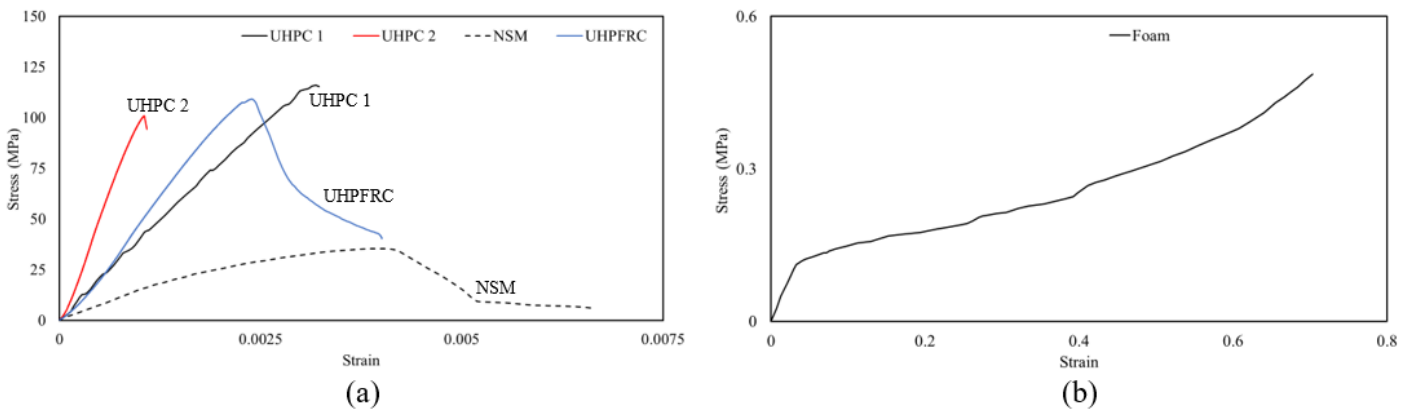

(a)

(b)

Figure 6 - Compressive stress-strain relationships of: a) C30 NSM, UHPC batch 1 (used for sandwich slab), UHPC batch 2 (used for box-cell slab) and UHPFRC; and (b) EPS foam.

2.3.2. *Direct tensions tests*

The direct tensile stress-strain behaviours of the UHPC, UHPFRC, BFRP mesh, EPS, BFRP mesh reinforced UHPC composite, and steel reinforcing bars were also experimentally established. Two types of dog-bone shaped specimens were used for the direct tension tests of UHPC, UHPFRC and BFRP mesh reinforced UHPC composite and the specimens were tested under displacement control at a constant rate of 0.025 mm/s. Their typical failure modes under direct tension are illustrated in Figs. 7 (a) to (d).
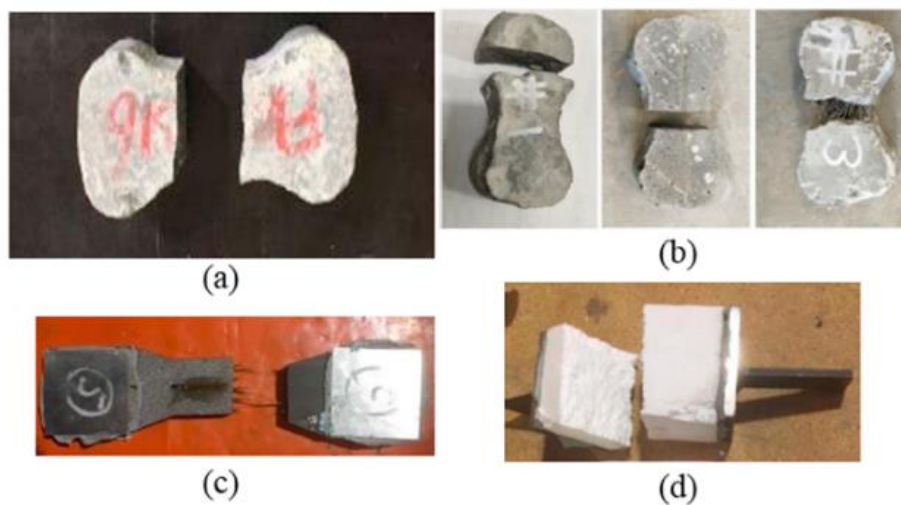

Figure 7 - Typical tensile failure modes of: a) UHPC (sandwich panel batch); b) UHPC & UHPFRC (box-cell panel batch); c) UHPC-BFRP mesh composite; and d) EPS foam.

EPS foam flatwise tensile behaviour was determined using cubic specimens with dimension of 75 mm and the typical failure mode of the EPS foam under direct tension is shown in Fig. 7 (d). The BFRP mesh with 10 mm × 10 mm mesh size was fabricated using unidirectional fibre strip of 10 mm width and 0.18 mm thickness and the tensile properties of the BFRP material were obtained flat coupon tests as per ASTM D3039M-08 [31]. The test results of the dog-bone specimens are shown in Table 3 and the representative tensile stress-stain curves of UHPC, UHPFRC, EPS, steel reinforcement and BFRP mesh reinforced UHPC composite are illustrated in Figs. 8 (a) and (b).

Mixture	Specimen	Peak Load (kN)	Compressive strength, f'_c (MPa)	Mean	Standard Deviation	Coefficient of Variation
UHPC1	B1D1	3.19	3.56	3.70	0.17	0.045
	B1D2	3.54	3.95			
	B1D3	3.27	3.65			
UHPC2	B2D1	1.84	2.05	2.05	0.204	0.099
	B2D2	2.07	2.31			
	B2D3	2.09	2.33			
	B2D4	1.62	1.81			
	B2D5	1.67	1.86			
	B2D6	1.75	1.95			
UHPFRC	B3D1	3.09	3.44	3.30	0.11	0.034
	B3D2	2.85	3.18			
	B3D3	2.93	3.27			

Table 3 – Dog-bone tensile test results for UHPC and UHPFRC.
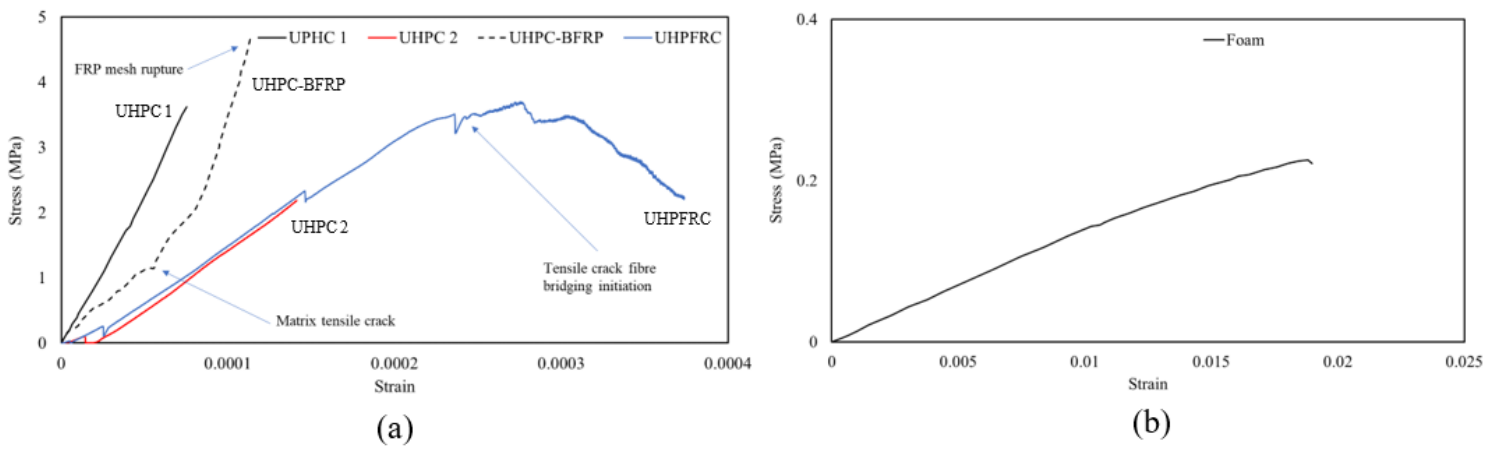

Figure 8 - Tensile stress-strain relationships of: a) UHPC (sandwich panel), UHPC-BFRP mesh composite, UHPC (box-cell panel), and UHPFRC; and b) EPS foam.

2.3.3. *Summary of results*

The key properties of each component are summarized in Table 4 and were obtained through the material testing and include their elastic modulus (E), Poisson's ratio (v), compressive and tensile strength (f'_c and f_t, respectively), and shear modulus (G) which is calculated as $G = E/2(1 + v)$.

Material	Compressive strength, f'_c (MPa)	Tensile strength, f_t (MPa)	Poisson's ratio, v	Elastic modulus, E (GPa)	Shear modulus, G (GPa)
UHPC (for Type A panels)	116.1	3.70	0.213	44.8	18.5
NSM	35.2	-	0.202	15.6	6.5
UHPC-BFRP composite	-	4.72	-	-	-
BFRP	-	2200*	-	97.0*	-
EPS foam	-	0.225	0.105*	6.09	2.8
UHPC (For specimens BI & BII)	100.8	2.05	0.18	61.8	10.3
UHPFRC (for Specimen BIII)	109.9	3.30	0.19	46.4	10.8
N8 steel deformed bars	-	500*	0.3*	200*	76.9*
RevKlip 700 0.42 Zincalume	-	550*	0.3*	200*	76.9*

*Manufacturer reported properties

Table 4 – Summary of material properties.

3. EXPERIMENTAL RESULTS AND DISCUSSION

3.1. Observations of one-way slab tests

3.1.1. *Sandwich panel observations*

The failure modes of the three sandwich panels are shown in Figs. 9 (a) - (c). The observed failure modes of panels AI and AIII were typical flexural failure modes with a major tensile

crack initially appearing on the bottom face sheet at mid-span and then gradually propagating towards the neutral axis position. Consequently, panels AI and AIII both failed due to the tensile fracture of the lower concrete face sheet and crushing of the upper concrete face sheet. Note that the change in the configuration of the core layer resulted in no distinct difference in the failure mode of the sandwich panels. However, panel AII experienced an unexpected premature failure due to the delamination occurring at the interface between the NSM and the EPS foam plate in the core, immediately after the formation of the major tensile crack. This premature failure was further inspected, and details are shown in Fig. 10. No debonding was observed between the NSM and UHPC whilst debonding occurred between the EPS and NSM and primarily due to the smooth surface of the EPS board.
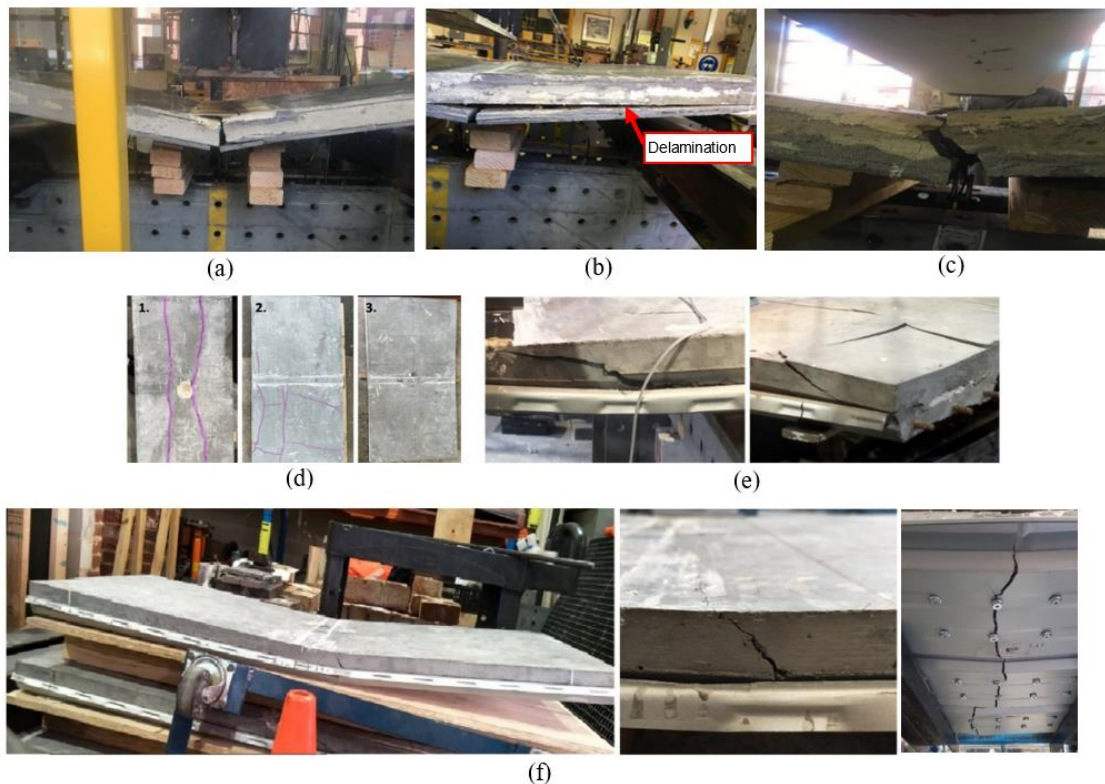

Figure 9 - Failure modes of: a) Type AI panel; b) Type AII panel; c) Type AIII panel; d) Top view of crack patterns of all Type B panels; e) Type BII panel; and f) Type BIII panel.
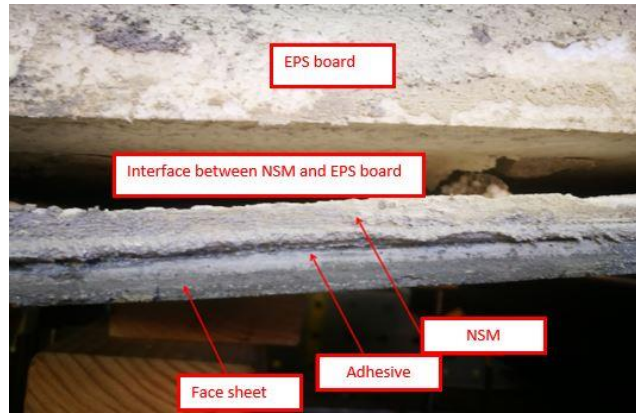
Figure 10 – Thorough inspection of the failure mode of Type AII panel.

3.1.2. *Box-cell panel observations*

The failure modes of all box-cell panels are shown in Figs. 9 (d) - (f). The observed failure mode of specimen B1 was not due to flexural failure, but due to the formation of longitudinal yield line cracks which propagated from the centre (where the circular patch load was applied) towards the corners of the panels. The failure was initiated due to punching shear, but it was worsened by the propagation of longitudinal flexural cracks propagating towards the corners. Additionally, delamination between the concrete and steel profile was observed after the formation of the longitudinal flexural cracks. Panel BII encountered tensile cracking at the mid-span and surface crushing on the top face observed in a wave-like pattern (Figs. 9 (d) and (e)). The initial crack widened with the increased applied load, however the shear connectors (screw anchors) had begun to loosen from the concrete component during the test. At failure, the crack completely widened associated with the formation of several secondary cracks and the concrete face almost debonded completely from the steel profile. Panel BIII encountered some tensile cracking at the mid-span, but no visible crushing on the top face and retained its structural integrity throughout the loading procedure until failure. Additionally, the bond between the steel profile and UHPFRC was near-intact, with only minor debonding occurring at failure. The panel failed due to fracturing of the steel profile at the load point propagating through the

screw anchor perforations, but there was no major tensile cracking or crushing of the UHPFRC or major debonding of the profile from the concrete, indicating high reserve capacity in the UHPFRC had loading extended past the failure point.

3.2. Load-deflection relationships

The experimentally recorded load-deflection relationships of the panels are illustrated in Figs. 11 (a) and (b) and for the panels AI and AIII this nearly followed the same linear ascending trend until the peak load. Moreover, the panel produced using EPS foam cylinders exhibited a slightly lower flexural stiffness for the initial ascending branch, owing to the lower stiffness of the EPS foam compared to that of the NSM. Panels AI and AIII also exhibited a sudden drop in their load bearing capacity immediately after reaching the peak load and no significant yielding plateau was observed due to the absence of tensile steel reinforcement. With the incorporation of EPS foam in its core, specimen AIII exhibited more ductile behaviour compared to that of specimen A1, demonstrating a longer descending branch with a shallower slope for the load-deflection response. Fig. 11 (a) indicates that prior to debonding of the NSM to EPS form board interface for the panel AII specimen, it exhibited significantly lower flexural stiffness in comparison to the other Type A panel specimens.
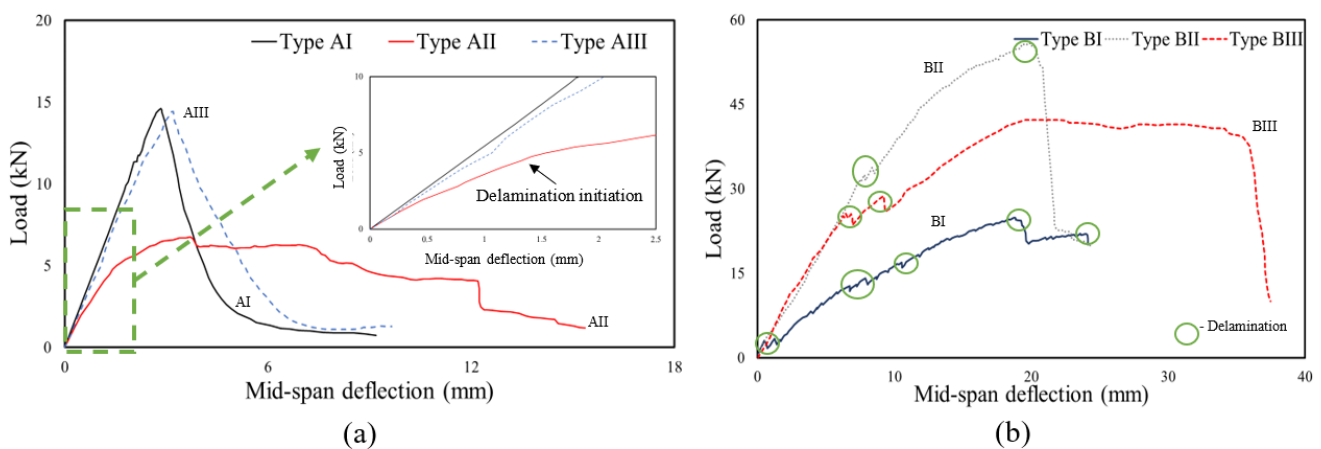

Figure 11 - Load-deflection relationships of: (a) Type A; and (b) Type B panel systems.

Fig. 11 (b) illustrates the varying flexural stiffness between the three B panel specimens, all exhibiting differing structural performances owing to their varying applied loading conditions (specimen BI as a circular patch load versus specimens BII & BIII as a line load) and their panel system configurations. Panels BI and BII exhibited similar post-peak behaviour; once debonding occurred between the steel profile and concrete section, the load-carrying capacity drastically decreased, and is much more evident for panel BII. Subsequently, both panels have a lower ductility in comparison to panel BIII. Whilst the steel profile failed in tension, the concrete remained intact and there was significant bond between the UHPFRC and steel profile as opposed to panels BI and BII which both encountered delamination, Fig. 11 (b) indicates that panel BIII exhibited a significant ductility, owing to sustenance of the load capacity with increase deformation before failure. This is due to the steel fibres present in the concrete and the stronger bond between the steel profile and UHPFRC. Intuitively, panel BII exhibited the largest peak load and strength-to-weight ratio, owing to the presence of the reinforcement. However, strength and strength-to-weight ratio are not necessarily key indicators in the design of such panels, and this is evident in the failure mode of panel BII in comparison to the other Type B panels, where at the onset of delamination, there was a significant decrease in capacity before failure. The strength-to-weight ratios for Type A and B panels are compared in Table 5.

Composite panel type	Specimen	Peak load (kN)	Self-weight (kg/kN)	Strength-to-weight ratio
Sandwich	AI	14.6	170.65/1.67	8.7
	AII	6.7	90.88/0.89	7.5
	AIII	14.2	130.09/1.28	11.1
Box-cell	BI	25.1	114.00/1.12	22.4
	BII	56.0	116.55/1.14	49.1
	BIII	42.6	117.78/1.16	36.7

Table 5 – Comparison of strength-to-weight ratios of composite panels.

4. ANALYTICAL MODELS AND FINITE-ELEMENT ANALYSIS

The first three types of panels (Figs. 1 (a) - (c)) having a sandwich construction with uniform thickness are analysed by two different analytical techniques popularly known as Elementary Sandwich Panel Theory (EST) and the Advanced Sandwich Panel Theory (AST). Both these techniques were proposed by Allen [32] which are widely accepted for the elastic analysis of sandwich panels. The multi-cell composite panel (Fig. 1 (d)), which having a relatively complex structural configuration, is analysed with elastic segmental sectional analysis, an analytical technique proposed by [33]. All these panels are analyses at their serviceability limit states by the above-mentioned methods with some modifications needed for these panels. Additionally, a detailed finite-element analysis of the multi-cell composite panel (Fig. 1 (d)) is performed using a well-regarded finite element (FE) code ABAQUS to simulate the response of the structure both in elastic and inelastic range.

4.1. Sandwich panels

4.1.1. *Elementary sandwich panel theory (EST)*

The EST is first applied to estimate the load-deflection response of the sandwich panels (Type A). In order to accommodate the properties of multi-material composite core, the EST is modified as it was originally developed by Allen [32] for a homogeneous core material. A basic assumption of EST is the core resists shear force, and the face sheets carry membrane forces applied by the bending moment. Taking the mid-plane of the panel as the reference axis, the flexural rigidity (D) of the sandwich panel can be expressed as [32]:

$$D = E_f(bt^3/6) + E_f(btd^2/2) + E_c(bc^3/12) \tag{1}$$

where E_f and E_c are the elastic moduli of the face sheets and the core materials respectively, t is the thickness of the face sheet, b is the width of the panel cross-section, c is the core thickness, and d is the distance between the centroids of top and bottom face sheets. For the

composite core comprising of foam and NSM, the homogenised elastic modulus can be determined using the rule of mixture as:

$$E_c = E_{cf}F_{cf} + E_{cm}F_{cm} \tag{2}$$

where E_{cf} and E_{cm} are the elastic moduli of the foam and the NSM respectively while F_{cf} and F_{cf} are their respective volumetric fractions. Once the flexural stiffness is obtained, the deflection of a simply supported sandwich panel subjected to a mid-span point load P at serviceability limit state can then be determined as:

$$\Delta_{total} = \Delta_1 + \Delta_2 \tag{3}$$

where Δ_1 and Δ_2 are the contributions due to bending and shear deformations as follows.

$$\Delta_1 = \frac{PL^3}{48D} \tag{4}$$

$$\Delta_2 = \frac{PL}{4U} \tag{5}$$

where U is the shear rigidity that can be expressed as [32]:

$$U = G_c \frac{bd^2}{c} \tag{6}$$

It is to be noted that the shear modulus of the composite core needs to be modified in a similar manner as:

$$G_c = G_{cf}F_{cf} + G_{cm}F_{cm} \tag{7}$$

4.1.2. *Advanced sandwich panel theory (AST)*

The advanced sandwich panel theory (AST) aims to improve the contribution of shear deformation by amending Eq. (5) to accommodate other effects in a comprehensive manner [32] as:

$$\Delta_2 = \frac{PL}{4U}\left(1 - \frac{I_f}{I}\right)\varphi_1 \tag{8}$$

where I is the second moment area of a face sheet about the centroidal axis of the panel, I_f is the sum of the second moment areas of the face sheets about their own centroid, and the coefficient φ_1 can be calculated as follows.

$$\varphi_1 = 1 - \frac{\sinh\theta + \tanh\theta(1-\cosh\theta)}{\theta} \tag{9}$$

$$\theta = \frac{L}{c}\left[\frac{G_c}{2E_f}\frac{c}{t}\left(1 + \frac{3d^2}{t^2}\right)\right]^{0.5} \tag{10}$$

where L is the length of the sandwich panel.

4.2. Box-cell panels

4.2.1. *Segmental sectional analysis*

The segmental sectional analysis is used to predict the load-deflection response of box-cell panels (Type B). In this technique, the cross-section of the panel is first divided into a finite number of slices along its depth and an initial guess of the neutral axis position and curvature is made. Based on the assumption that plane section remains plane before and after bending, the strains at each slice are determined, which are used to calculate the corresponding stresses (tensile/compressive) by the nonlinear stress-strain relationships of different materials. Additionally, it assumes full shear interaction between the material layers and the analysis is based on one-way bending of the panel neglecting the contribution of self-weight. With these stresses, the compressive and tensile forces acting on the cross-section are calculated to check the force equilibrium. If this is not achieved, the process is repeated by adjusting the neutral axis depth until the sectional force equilibrium is achieved. The moment acting on the section is then calculated and used to evaluate the corresponding load P acting on the panel under three point bending. The curvature is incrementally increased, and the above process is repeated to obtain the nonlinear moment-curvature relationship for the entire range of loading P up to its peak. The application of the segmental analysis is suitable to composite sections and previous research has used it successfully for the analysis of UHPFRC composite beams [33]. The schematic description of the process for a generic scenario is shown in Fig. 12.
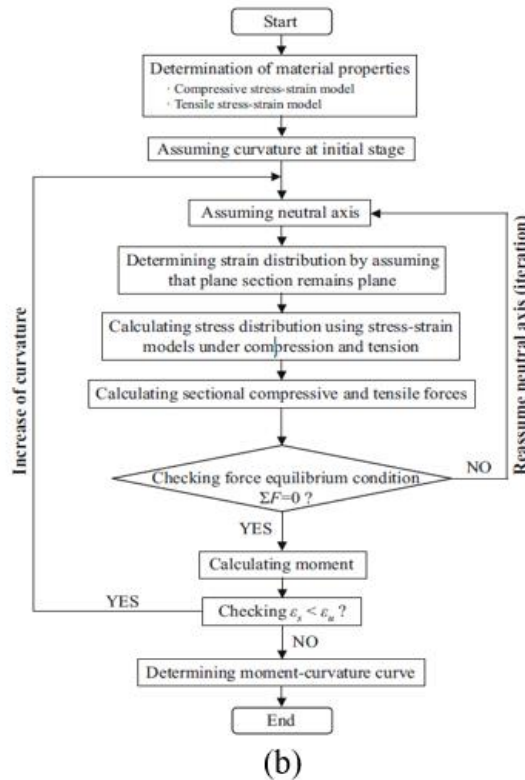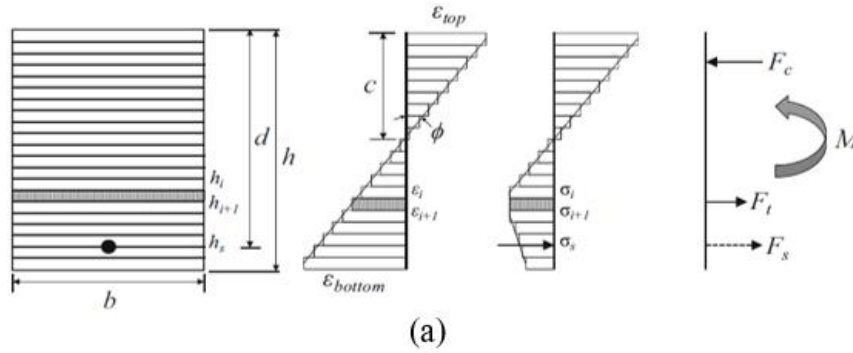
Figure 12 – Segmental sectional analysis for a typical beam section: (a) Schematic description of stress and strain distributions within cross-section; and (b) Algorithm for segmented sectional analysis [33].

For the evaluation of stress as stated above, the Hognestad [34] model is adopted for the constitutive behaviour of concrete in compression while a simple bilinear model is used for tension. Based on that model [34], the compressive stress prior to reaching the ultimate stress can be given as:

$$\sigma_c = f_c \left[\frac{2\varepsilon_c}{\varepsilon_0} - \left(\frac{\varepsilon_c}{\varepsilon_0} \right)^2 \right] \, for \, 0 \leq \varepsilon_c < \varepsilon_{c0} \tag{11}$$

The stress in post-peak region can be easily determined as it [34] has a linear constitutive relationship for that range. The steel bars and profile sheets are modelled by elastic perfectly plastic constitutive law. The yield (f_y) strength of steel profiles is taken as 550 MPa and as 500 MPa for reinforcement bars (both provided by supplier). It is to be noted that the complex shape of the section requires proper care to accommodate the variation of geometry of individual strips.

4.2.2. *Finite-element analysis*

The analysis of the box-cell panels using segmental approach is relatively simply for predicting the load-deflection response of these structures but the technique is based on many simplifications in addition to its applicability to simple load and boundary conditions. To predict a more realistic behaviour of these panels accurately under any complex scenario, a detailed finite-element analysis has been undertaken using a highly capable commercially available FE code (ABAQUS).

The individual parts of the panel made of different materials are modelled with 3D tetrahedral solid elements with reduced integration and hourglass control. A convergence study is made to determine the optimum mesh sizing for this problem. The FE meshing as well as attachments used for application of loading and boundary conditions are shown in Figs. 13 (a) – (d).
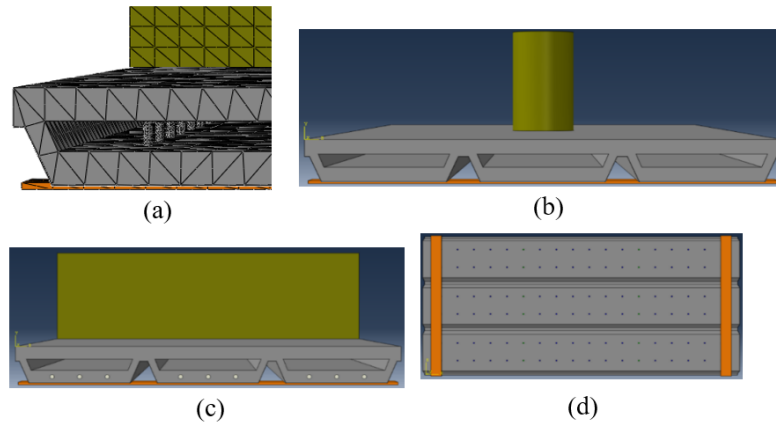
Figure 13 – Finite-element modelling of: a) Tetrahedral element mesh and sizing; b) BI panel; c) BII panel; and d) BIII panel.

The steel parts (profile sheets, reinforcing bars and screw anchors) are modelled using elastoplastic material model (von Mises), whilst the concrete parts (UHPC/UHPFRC) are modelled using the concrete damage plasticity (CDP) model which considers stiffness degradation using damage variables coupled with plastic deformations. The CDP model is the modified form [35] of the initial model proposed by Lubliner et al. [36] by amending the yield function and incorporating the fracture energy cracking criterion of Hillerborg et al. [37]. From the three concrete materials models of ABAQUS (concrete smeared crack (CSC), brittle crack concrete (BCC) and CDP), the CDP model is selected as it is a comprehensive model for accurately simulating the post-peak behaviour and can capture the inelastic behaviour of UHPC and UHPFRC both in tension and compression, incorporating damage, and compression hardening and tension stiffening behaviours [38].

The implementation of the CDP model requires values for the following parameters: Poisson's ratio (v), dilation angle (ψ) for controlling plastic strain increment direction, eccentricity (ε) for adjusting flow potential geometry from straight line to a hyperbola, biaxial stress ratio ($\sigma_{bsr} =$

σ_{b0}/σ_{c0}), shape factor (K_c) for adjusting deviatoric plane geometry, and viscosity parameter (μ) for minimising convergence problem through regularisation. The values of these key parameters are found from tests conducted by Singh et al. [39] for UHPC and Shafieifar et al. [40] for UHPFRC. Values for some parameters are identical for both materials ($e = 0.1$, $\mu = 0.0001$, $K_c = 0.67$) whereas other parameters are: v (UHPC) = 0.18, v (UHPFRC) = 0.19, ψ (UHPC) = 56°, ψ (UHPFRC) = 35°, σ_{bsr}(UHPC) = 0.67 and σ_{bsr}(UHPFRC) = 1.16. The stiffness recovery due to crack closing/opening at the tension-compression transition is accommodated by the stiffness recovery parameters (W) which is taken as 0.2 (20%) for both tension (W_t) and compression (W_c) recoveries. The uniaxial stress-strain curve (in compression and tension) of UHPC and UHPFRC (Fig. 14) is used by the CDP model in our finite-element simulation and are modifications of the experimental test results (Figs. 6 and 8) using techniques devised by Nayal and Rasheed [41].
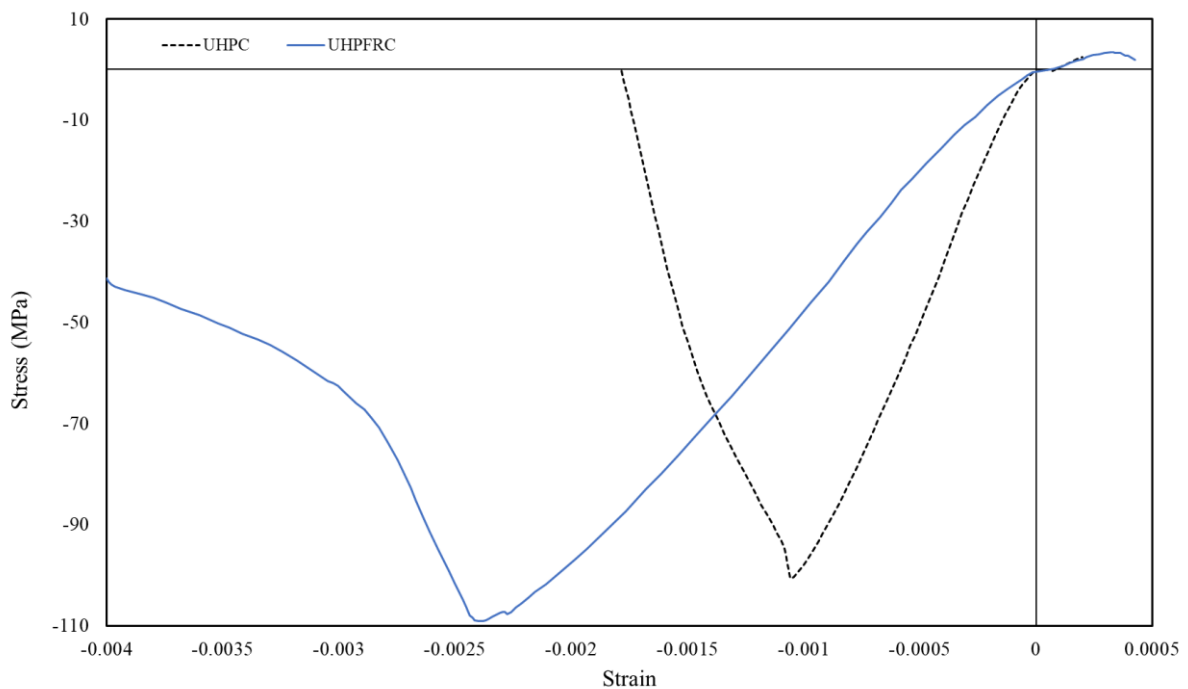

Figure 14 – Uniaxial stress-strain relationship of UHPC and UHPFRC in tension and compression region.

4.3.   Model validation and comparisons

The results of the experimental and numerical results are summarised in Table 4 and the experimental, analytical and finite-element modelled load-deflection responses are shown in Figs. 15 and 16.
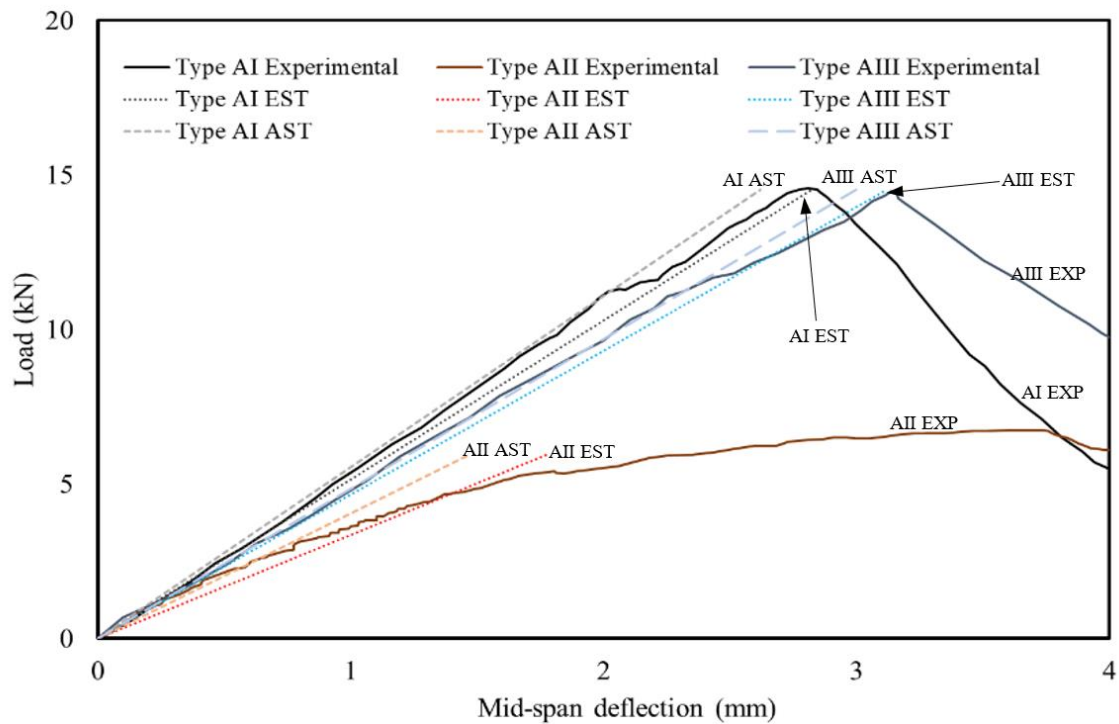

Figure 15 - Comparisons of experimental and analytical results for the sandwich.

Figs. 15 (a) to (c) shows comparisons between the experimental results and predictions using both the EST and AST. It can be seen from these figures that both methods accurately predict the load-deflection relationship of the sandwich panels at their serviceability limit states, however there is a slight overestimation of the deflection by the modified EST. This is due to the AST being able to account for the contribution due to shear deformations. The comparisons shown in Fig. 15 (b) indicates that due to the higher volumetric ratio of the EPS foam used in the core of the sandwich panel, the AII panel exhibited a lower flexural stiffness compared to

the other two panels at their serviceability limit states. Table 4 summarises the salient results

of the analytical models and shows that they correlate very well with the test results. The

predicted deflections match very closely with the experimental values for the matching applied

load for both the EST and AST. Furthermore, Fig. 15 (b) shows the predicted stiffness of both

the EST and AST agrees well with the experimental load-deflection response in the linear
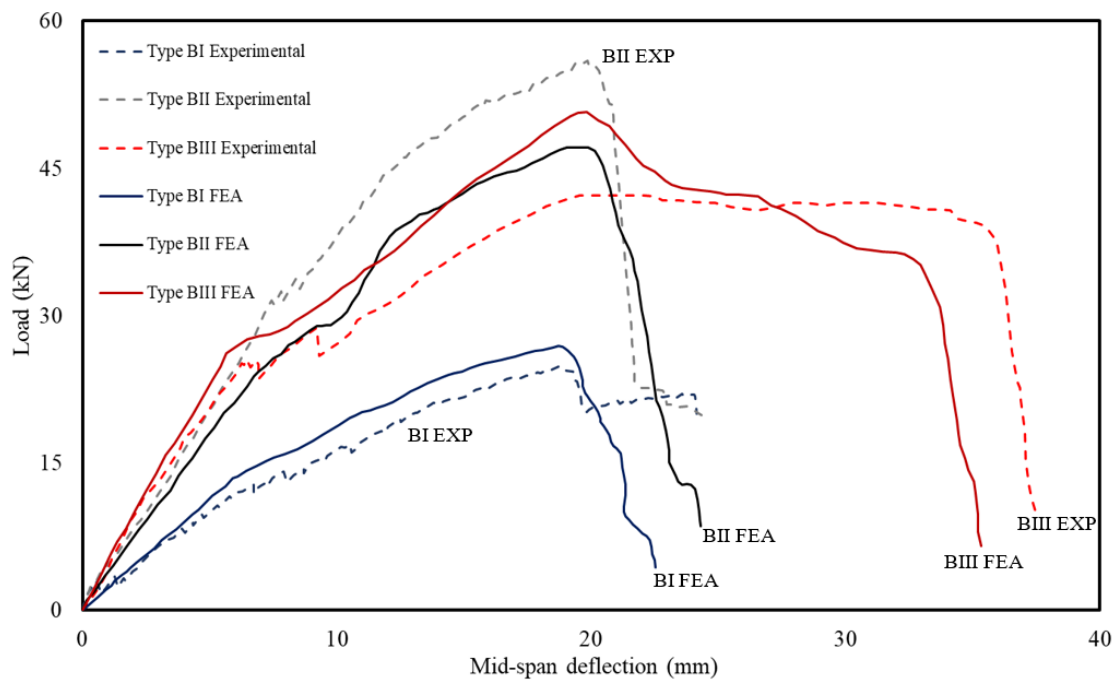
range.

Figure 16 - Comparisons of experimental and finite-element analysis results for the box-cell panel.

Fig. 16 display the results from the sectional and finite-element analyses, and the results are

found in Table 6. The sectional analysis provides an accurate prediction of the peak load and

only for the case of panel BIII vary more significantly than the other two panels with regards

to the predicted peak load. The finite-element analyses, both with regards to the predicted peak

loads, associated deflection and load-deflection responses compare well across all three Type

41

B panels. Notably the post-peak predictions and load-deflection results by the FE analysis accurately model both the reserve load capacity reduction and the sustained load-deflection response after the peak loads. Additionally, the panel stiffnesses highlight the accuracy of both the EST, AST and finite-element analysis in predicting the behaviour of the panels in the elastic region.

| | Experimental | | | Numerical | | | | | |
| | | | | EST | | | AST | | |
Specimen	Peak load (kN)	Deflection (mm)	Stiffness (kN/mm)	Peak load (kN)	Deflection (mm)	Stiffness (kN/mm)	Peak load (kN)	Deflection (mm)	Stiffness (kN/mm)
AI	14.6	2.80	5.4	14.6	2.79	5.2	14.6	2.65	5.7
AII	6.7	3.70	4.0	6.7	2.01	3.3	6.7	1.64	4.0
AIII	14.2	3.17	4.9	14.2	3.11	4.6	14.2	2.99	4.9
				Sectional			FEA		
BI	25.1	18.7	2.0	30.0	-	-	26.9	18.7	2.3
BII	56.0	19.9	4.3	57.9	-	-	47.1	19.0	3.8
BIII	42.6	19.5	4.0	29.1	-	-	50.7	19.7	4.5

Table 6 – Comparison of experimental, numerical and analytical results

Visual comparison of the damage prediction and stress distributions by the FE analysis for the Type B specimens are shown in Figs. 17-19. Fig. 17 (a) shows the crack pattern propagating from the centre to the end of panel BI and the finite-element analysis supports this with the damage distribution calculated in Fig. 17 (a). Figs. 17 (b)-(c) highlight the large stress distribution at the top and bottom surfaces of the panels and correlate well with the damage at the loading point in Fig. 17 (a). Panel BII undergoes cracking through the UHPC section in Fig. 18 (b) and the stress distribution shown in Fig. 18 (c) clearly shows the large concentration of stresses along the same area. Fig. 19 (a) and (c) display the cracking of the steel profile and the low crushing of concrete near the loading point and Figs. 19 (b) and (d) support this in

highlighting the location of tensile stress concentration along the steel profile and the compressive stresses near the loading point.
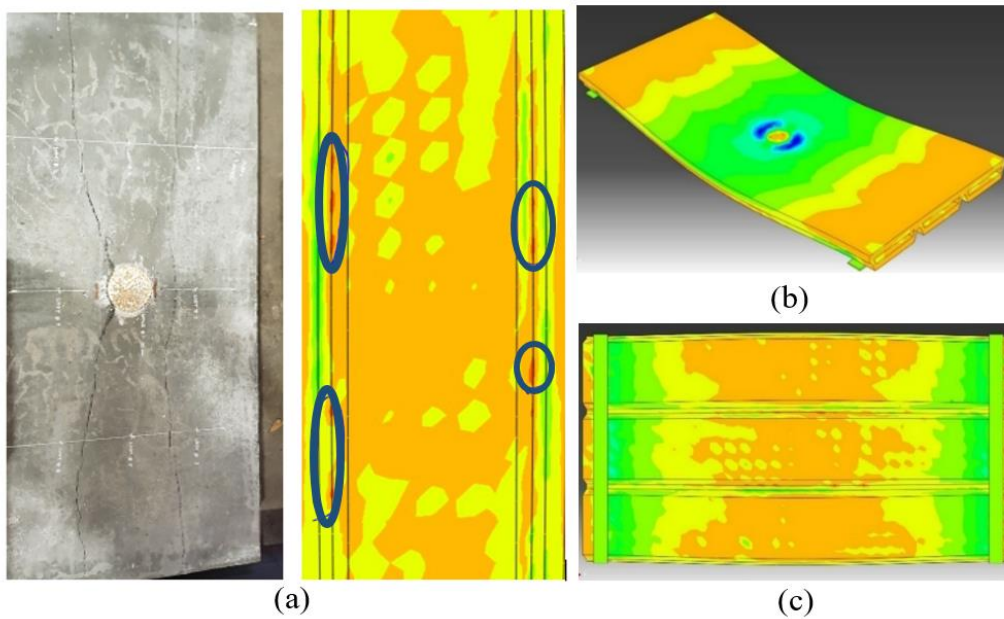

(a)   (b)   (c)

Figure 17 – Finite-element analysis of Panel BI: a) Top surface damage contour comparison; b) Top surface normal stress; and c) Bottom surface normal stress.
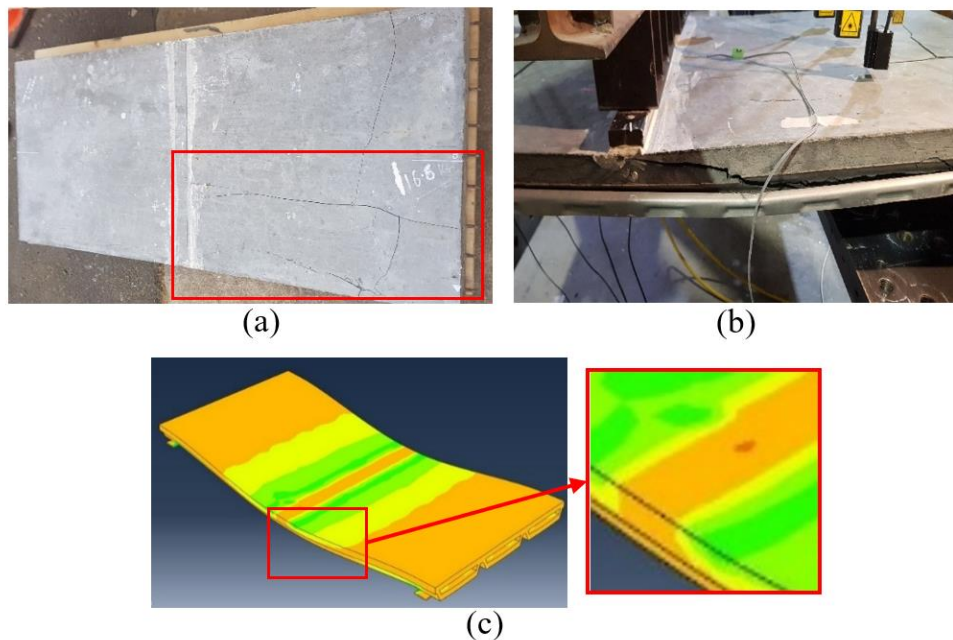

(a)   (b)

(c)

Figure 18 – Finite-element analysis of Panel BII: a) Top surface damage; b) Top surface sectional cracking; and c) Top surface normal stress concentration comparison.
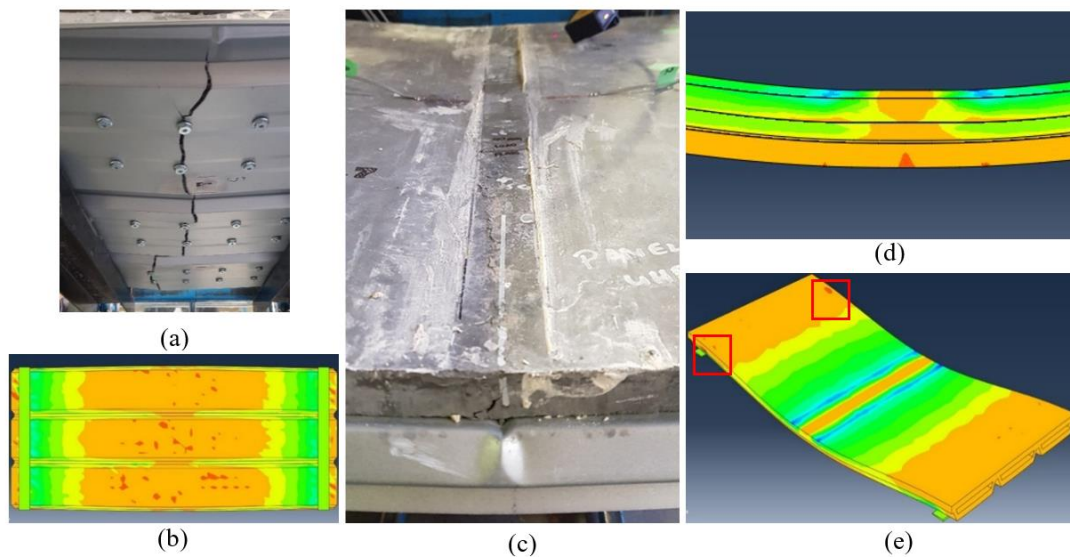
Figure 19 – Finite-element analysis of Panel BIII: a) Bottom surface damage; b) Bottom surface normal stress; c) Top surface loading region damage; (d) Panel centre stress distribution; and (e) support normal stress concentrations.

5. CONCLUSIONS

The objective of the present study was to develop novel multi-cell systems based on the box-cell and sandwich panel systems. The newly-developed panel systems were fabricated by combining the high strength and ductility of BFRP mesh-reinforced UHPC face sheets, NSM and EPS foam in differing configurations for the sandwich panels, and UHPC, UHPFRC and steel deformed bars for the box-cell panels. The panels were predominantly tested as one-way slabs and the structural behaviour of the 6 panels were simulated at their serviceability limit states and modelled using the modified EST, AST, segmental sectional analysis, and finite-element analysis. Based on the experimental and theoretical investigations, it can be concluded that the design philosophy of the two systems can be easily adopted for designing composite multi-cell panels.

44

UHPFRC is suitable for the construction of box-cell panels and further research is warranted to study the feasibility of using a thicker steel profile to prevent tensile failure. The presence of steel fibres in the concrete prevents global failure of the panel, so it is highly recommended to investigate differing steel fibre volumes for the box-cell panel system. It is recommended to increase the embedment depth or increase the amount of shear connectors along the length of the panel to avoid delamination of the steel profile from the concrete. The sectional analysis is a feasible method in predicting the load capacity of box-cell panels, and the finite-element analysis is a viable method of simulating the complete structural performance of the panels.

Additionally, partially replacing NSM using horizontally orientated EPS cylinders can effectively reduce the self-weight of the sandwich panel without significantly compromising its mechanical properties under flexure, and C30 grade NSM can provide adequate bond strength between the core and face sheets. For the core layer of a sandwich panel combining both NSM and EPS foam board, the smooth surface of an EPS foam board is not beneficial for creating a strong mechanical bond between it and the adjacent NSM layer. It is recommended to provide an adhesive layer between the EPS and the NSM for improving the interfacial bond strength. The modified EST method can accurately predict the load-deflection behaviour of sandwich panels at the serviceability limit state, and the AST being more accurate in generating the elastic behaviour load-deflection behaviour.

REFERENCES

1.   Omer, A.M., Energy, environment and sustainable development. Renewable and sustainable energy reviews, 2008. 12(9): p. 2265-2300.

2.   Kulpa, M. and T. Siwowski, Stiffness and strength evaluation of a novel FRP sandwich panel for bridge redecking. Composites Part B: Engineering, 2019. 167: p. 207-220.

3.   Mohamed, M., et al., Manufacturing and characterization of polyurethane based sandwich composite structures. Composite Structures, 2015. 123: p. 169-179.

4.   Norris, T.G. and A. Chen, Development of insulated FRP-confined Precast Concrete Sandwich panel with side and top confining plates and dry bond. Composite Structures, 2016. 152: p. 444-454.

5.   Choi, W., S.-J. Jang, and H.-D. Yun, Design properties of insulated precast concrete sandwich panels with composite shear connectors. Composites Part B: Engineering, 2019. 157: p. 36-42.

6.   Mastali, M., et al., Development of innovative hybrid sandwich panel slabs: Experimental results. Composite Structures, 2015. 133: p. 476-498.

7.   Upadyay, A. and V. Kalyanaraman, Simplified analysis of FRP box-girders. Composite structures, 2003. 59(2): p. 217-225.

8.   Amir-sayyafi, E., A. Chowdhury, and A. Mirmiran. A super lightweight hurricane-resistant thin-walled box-cell roofing system. in International Symposium on Structural Engineering. 2016.

9.   Harding, P., BubbleDeck–Advanced structure engineering. BubbleDeck article, 2004: p. 4-7.

10.   Ranjitham, M., N. Manjunath, and S. Dhivyabharathi, Numerical and Experimental study on Bubble Deck Slab with M-SAND. Construction Materials and Management: p. 228.

11.   Lai, T., Structural behavior of BubbleDeck® slabs and their application to lightweight bridge decks. 2010, Massachusetts Institute of Technology.

12.   Saifulla, M. and M. Azeem, Comparative Seismic Performance of a Conventional Slab and Flat Slab over a Bubble Deck Slab.

13.   Xie, T., et al., Characterizations of autogenous and drying shrinkage of ultra-high performance concrete (UHPC): An experimental study. Cement and Concrete Composites, 2018. 91: p. 156-173.

14.   Visintin, P., et al., Experimental investigation of moment redistribution in ultra-high performance fibre reinforced concrete beams. Construction and Building Materials, 2018. 166: p. 433-444.

15.   Sobuz, H.R., et al., Flow and Strength Characteristics of Ultra-high Performance Fiber Reinforced Concrete: Influence of Fiber Type and Volume-fraction. Journal of Civil Engineering and Construction, 2017. 6(1): p. 15-21.

16.   Graybeal, B.A., Material property characterization of ultra-high performance concrete. 2006, United States. Federal Highway Administration. Office of Infrastructure ….

17.   Graybeal, B.A., Tensile mechanical response of ultra-high-performance concrete. Advances in Civil Engineering Materials, 2015. 4(2): p. 62-74.

18.   Richard, P. and M. Cheyrezy, Composition of reactive powder concretes. Cement and concrete research, 1995. 25(7): p. 1501-1511.

19.   Sobuz, H., et al., Manufacturing ultra-high performance concrete utilising conventional materials and production methods. Construction and Building materials, 2016. 111: p. 251-261.

20.   Sturm, A., et al., New Testing Approach for Extracting the Shear Friction Material Properties of Ultra-High-Performance Fiber-Reinforced Concrete. Journal of Materials in Civil Engineering, 2018. 30(10): p. 04018235.

21.   Sturm, A., et al., Time-dependent tension-stiffening mechanics of fiber-reinforced and ultra-high-performance fiber-reinforced concrete. Journal of Structural Engineering, 2018. 144(8): p. 04018122.

22.   Habel, K., E. Denarié, and E. Brühwiler, Experimental investigation of composite ultra-high-performance fiber-reinforced concrete and conventional concrete members. ACI Structural Journal, 2007. 104(1): p. 93.

23.   Yoo, D.-Y., S.-T. Kang, and Y.-S. Yoon, Enhancing the flexural performance of ultra-high-performance concrete using long steel fibers. Composite Structures, 2016. 147: p. 220-230.

24.   Yoo, D.-Y., et al., Material and bond properties of ultra high performance fiber reinforced concrete with micro steel fibers. Composites Part B: Engineering, 2014. 58: p. 122-133.

25.   Wu, Z., et al., Effects of steel fiber content and shape on mechanical properties of ultra high performance concrete. Construction and building materials, 2016. 103: p. 8-14.

26.   Hannawi, K., et al., Effect of different types of fibers on the microstructure and the mechanical behavior of ultra-high performance fiber-reinforced concretes. Composites Part B: Engineering, 2016. 86: p. 214-220.

27.   Wright, H., H. Evans, and P. Harding, The use of profiled steel sheeting in floor construction. Journal of Constructional Steel Research, 1987. 7(4): p. 279-295.

28.   Rafiei, S., et al., Profiled sandwich composite wall with high performance concrete subjected to monotonic shear. Journal of Constructional Steel Research, 2015. 107: p. 124-136.

29.   Shams, A., et al., Innovative sandwich structures made of high performance concrete and foamed polyurethane. Composite Structures, 2015. 121: p. 271-279.

30.   ASTM, ASTM C469/C469M-14: 2002. Standard Test Method for Static Modulus of Elasticity and Poisson's Ratio of Concrete in Compression. West Conshohocken, PA, US: ASTM International.

31.   ASTM, ASTM D3039/D3039M–08, Standard Test Method for Tensile Properties of Polymer Matrix Composite Materials. West Conshohocken, PA, US: ASTM International.

32.   Allen, H.G., Analysis and design of structural sandwich panels: the commonwealth and international library: structures and solid body mechanics division. 2013: Elsevier.

33.   Yoo, D.-Y., N. Banthia, and Y.-S. Yoon, Flexural behavior of ultra-high-performance fiber-reinforced concrete beams reinforced with GFRP and steel rebars. Engineering Structures, 2016. 111: p. 246-262.

34.   Hognestad, E., Study of combined bending and axial load in reinforced concrete members. 1951, University of Illinois at Urbana Champaign, College of Engineering ….

35.   Lee, J. and G.L. Fenves, Plastic-damage model for cyclic loading of concrete structures. Journal of engineering mechanics, 1998. 124(8): p. 892-900.

36.   Lubliner, J., et al., A plastic-damage model for concrete. International Journal of Solids and Structures, 1989. 25(3): p. 299-326.

37.   Hillerborg, A., M. Modéer, and P.-E. Petersson, Analysis of crack formation and crack growth in concrete by means of fracture mechanics and finite elements. Cement and concrete research, 1976. 6(6): p. 773-781.

38.   Verma, M., et al., On low-energy impact response of ultra-high performance concrete (UHPC) panels. Materials & Design, 2016. 92: p. 853-865.

39.   Singh, M., M. Sadakkathulla, and A. Sheikh. Structural behaviour of ultra-high performance fibre reinforced concrete columns subjected to eccentric loading. 2015. International Association for Bridge and Structural Engineering.

40.   Shafieifar, M., M. Farzad, and A. Azizinamini, Experimental and numerical study on mechanical properties of Ultra High Performance Concrete (UHPC). Construction and Building Materials, 2017. 156: p. 402-411.

41.   Nayal, R. and H.A. Rasheed, Tension stiffening model for concrete beams reinforced with steel and FRP bars. Journal of Materials in Civil Engineering, 2006. 18(6): p. 831-841.

THIS PAGE HAS BEEN LEFT INTENTIONALLY BLANK

CHAPTER 2

Background

In this chapter, the box-celled composite system is investigated further as a wind-resistant structural element. Panels implementing helically ribbed glass fibre-reinforced polymer (GFRP) and steel reinforcement are produced and tested under three-point flexure in both directions to understand the full-range flexural behaviour of the system. The outcomes of the experimental are used to then assess the proposed system for compliance with current code provisions for both combined loading actions and permissible deflections when considered a main wind force resisting system (MWFRS).

List of manuscripts

Mahdi, S., Sheikh, A. H., Ali, M. M. & Elchalakani, M. (2021). "Experimental Investigation Into the Structural Behaviour of Ultra-High Performance Fibre-Reinforced Concrete Box-Celled Composite Panels." Submitted to *Composite Structures*.

Statement of Authorship

Title of Paper	Experimental Investigation Into the Structural Behaviour of Ultra-High Performance Fibre-Reinforced Concrete Box-Celled Composite Panels
Publication Status	☐ Published ☐ Accepted for Publication ☑ Submitted for Publication ☐ Unpublished and Unsubmitted work written in manuscript style
Publication Details	Mahdi, S., Sheikh, A. H., Ali, M. M. & Elchalakani, M. (2021). "Experimental Investigation Into the Structural Behaviour of Ultra-High Performance Fibre-Reinforced Concrete Box-Celled Composite Panels." Submitted to *Composite Structures*.

Principal Author

Name of Principal Author (Candidate)	Shahin Mahdi			
Contribution to the Paper	Conceptualisation, methodology, model development, data curation, and manuscript writing and revision			
Overall percentage (%)	55			
Certification	This paper reports on original research I conducted during the period of my Higher Degree by Research candidature and is not subject to any obligations or contractual agreements with a third party that would constrain its inclusion in this thesis. I am the primary author of thi			
Signature			Date	29/12/2021

Co-Author Contributions

Name of Co-Author	Abdul Hamid Sheikh			
Contribution to the Paper	Supervision, conceptualisation, methodology, and manuscript revision (20%)			
Signature			Date	29/12/2021

Name of Co-Author	Mohamed Sadakkathulla Mohamed Ali			
Contribution to the Paper	Supervision, conceptualisation, methodology, and manuscript revision (20%)			
Signature			Date	29/12/2021

Name of Co-Author	Mohamed Elchalakani		
Contribution to the Paper	Manuscript revision (5%)		
Signature		Date	29/12/2021

Experimental Investigation Into the Structural Behaviour of Ultra-High Performance Fibre-Reinforced Concrete Box-Celled Composite Panels

S. Mahdi[1*], A.H. Sheikh[2], M.S. Mohamed Ali[3], M. Elchalakani[4]

[1]Mr. Shahin Mahdi (Corresponding author)
Ph.D. Candidate
School of Civil, Environmental and Mining Engineering
The University of Adelaide
South Australia 5005
AUSTRALIA
Email: shahin.mahdi@adelaide.edu.au

[2]Associate Professor Abdul Hamid Sheikh
Associate Professor
School of Civil, Environmental and Mining Engineering
The University of Adelaide
South Australia 5005
AUSTRALIA
Email: abdul.sheikh@adelaide.edu.au

[3]Dr. Mohamed Sadakkathulla Mohamed Ali
Senior Lecturer
School of Civil, Environmental and Mining Engineering
The University of Adelaide
South Australia 5005
AUSTRALIA
Email: mohamed.mohamedsadakkathulla@adelaide.edu.au

[4]Dr. Mohamed Elchalakani
Senior Lecturer
School of Civil and Infrastructure Engineering
The University of Western Australia
Perth 6009
AUSTRALIA
Email: mohamed.elchalakani@uwa.edu.au

Experimental Investigation Into the Structural Behaviour of Ultra-High Performance Fibre-Reinforced Concrete Box-Celled Composite Panels

S. Mahdi[1*], A.H. Sheikh[2], M.S. Mohamed Ali[3], M. Elchalakani[4]

ABSTRACT

The present study investigates and advances on existing research on the structural performance of box-celled composite structures for its use as a wind-resistant roof system. The box-celled panel system is produced by casting ultra-high performance fibre-reinforced concrete (UHPFRC) into galvanised steel roofing profiled sheets with anchor screws and expanded polystyrene foam (EPS) placed in-situ to produce a light-weight system. Three reinforcement-based variations of the design are investigated and two panels for each variation are cast to produce six specimens. The structural responses of the variations as one-way panels under three-point flexure are experimentally studied for both positive and negative bending moment capacities. Test specimens showed flexural failure with significantly ductility and post-failure load capacity, and anchor screws preventing full delamination of steel profile and shear failure. Analysis based on the test results confirmed that the proposed system is compliant to various design standards based on upper limits for combined loading actions, and permissible deflections, highlighting its optimal performance.

Keywords: ultra-high performance fibre-reinforced concrete (UHPFRC); composite system; box-cell; steel profiled sheet; fibre-reinforced concrete; composite panel.

1. INTRODUCTION

The significant demand on pre-cast concrete composite panels is ever-increasing for commercial and residential structures and demand has particularly grown over the course of

the last few decades due to the structural advantages composite panels have over conventional concrete panels. [1]. Composite concrete panels can be designed to have excellent thermal conductivity, high strength-to-weight ratios, rapid construction techniques, architectural appeal, and eliminates the need for formwork [2]. Concrete composite panels are typically designed as sandwich structures where reinforced concrete layers, known as wythes, wedge a light rigid core which provides thermal insulation [3, 4]. A lesser-known form of composite structure is the box-celled panel where the advantages of box-girder structures are extended to pre-cast composite panel design.

Box-girder structures have been universally deployed due to a high torsional stiffness, lower propensity for flange/web buckling, high positive and negative bending moment capacity, and a high strength-to-weight ratio [5]. This concept has recently extended to the construction of box-cell panels and is illustrated in Fig. 1.

Figure 1 – Extension of the concrete box-girder slab to a pre-cast box-celled panel section.

The advantages of the girder system are transferrable to the concept of box-cell panels and become more significant when used as wind-resistant elements which encounter uplift, torsion and buckling [6, 7]. The box-cell panel system remains structurally efficient with the presence of the trapezoidal void and has minimal effect on the sectional capacity for both positive and negative bending as the major flexural compression and tension stresses occur in the top and bottom flange [8]. Moreover, the voids can be used to run electrical, water and other infrastructure services. The concept of the wind-resistant box-cell panel was first investigated

by Sayyafi et al. [8, 9] for devising a light-weight hurricane-resistant thin-walled box-cell roofing system using ultra-high performance concrete (UHPC). However, the failure mode in flexure for both positive and bending moment are brittle due to the nature of UHPC in tension. There is a lack of research in the adoption of other materials in the construction of pre-cast composite wind-resistant panel systems and hence there is a need to investigate the development of new box-cell composite panel systems.

Pre-cast composite structures are characterised by the cementitious material used in their construction and are typically made with normal strength concrete (NSC) or normal strength mortar (NSM). However, NSM and NSC both have mechanical disadvantages such as low tensile strength and comparatively low compressive strength, low permeability, and brittle failure. To improve upon these disadvantages, significant research has been performed over the last three decades in concrete technology which culminated in the development of ultra-high performance concrete (UHPC) by Richard and Cheyrezy [10, 11]. UHPC is characterised by a significant compressive strength owing to a high packing density and a reduction in water-to-cement ratio [12, 13]. Additionally, UHPC provides superior tensile strength, larger ductility, and durability compared to other cementitious materials [14]. Current research on UHPC has focused on improving mix designs to both reduce the cost and/or improve the mechanical properties, which can be achieved by material addition/replacement, simplifying manufacturing techniques and implementing conventional and more accessible materials [15-17]. One significant advancement is the addition of steel fibres to UHPC to create ultra-high performance fibre-reinforced concrete (UHPFRC). The addition of steel fibres improves upon the brittle nature of UHPC in tension, significantly increasing ductility, and improves strain hardening characteristics [18, 19]. Moreover, the steel fibres provide high post-cracking ductility as micro-cracks that form are bridged by the fibres, and this reduces crack widths in

the tensile region [20]. These mechanical properties are advantageous and desirable in designing pre-cast composite systems.

Pre-cast concrete composite panels are traditionally reinforced with steel or fibre-reinforced polymers (FRP) in regions of large tensile and compressive stress. Steel and FRP are desirable as reinforcing materials due to their high tensile and bond strength, however the optimisation of composite panel layers is limited by minimum cover requirements for the prevention of corrosion and bond failure [21]. This can be overcome by the adoption of profiled steel sheets as the lower layer in pre-cast concrete composite panels. Profiled steel sheets in concrete composite panel design are beneficial as they act as both permanent formwork for in-situ casting and tensile reinforcement without providing for reinforcement in the cementitious layers [22].

The above has emphasised the need for the development of a new and innovative pre-cast composite panel system which can incorporate the concepts and materials outlined. To address the these, this study aims to:

(1) Study the structural behaviour of one-way UHPFRC box-cell panels with varying reinforcement placement and material types through an experimental program,

(2) Evaluate the behaviour of the panels by comparing strength-to-weight performance and ductility,

(3) Assess the suitability of the panel system by calculating limits for maximum deflections and allowable loads for various building codes and guidelines, and

(4) Make recommendations for future use and design of similar composite panel systems.

To realise the above objectives, six box-cell composite panels with varying arrangements of reinforcement were fabricated and subjected to monotonically increasing line loads at their mid-spans. The deflections and strains along the top and bottom surfaces of the panels were measured for the increasing load. A thorough investigation was performed to assess the suitability of the panels as wind-resistant structural panels, assessing their flexural and deflection capacities to code provisions of prominent design standards. This research is an extension to previous research at the University of Adelaide [23], where the structural performance of UHPFRC composite box-cell panels were first investigated.

2. EXPERIMENTAL PROGRAM

2.1. Panel design

Six UHPFRC panels of varying reinforcement arrangements of dimensions 1500 mm × 700 mm × 70 mm were cast and tested under one-way bending to evaluate the structural performance of the box-celled panels in both positive and negative bending directions. The cross-sectional configuration of the panels examined in the present study are illustrated in Fig. 2.
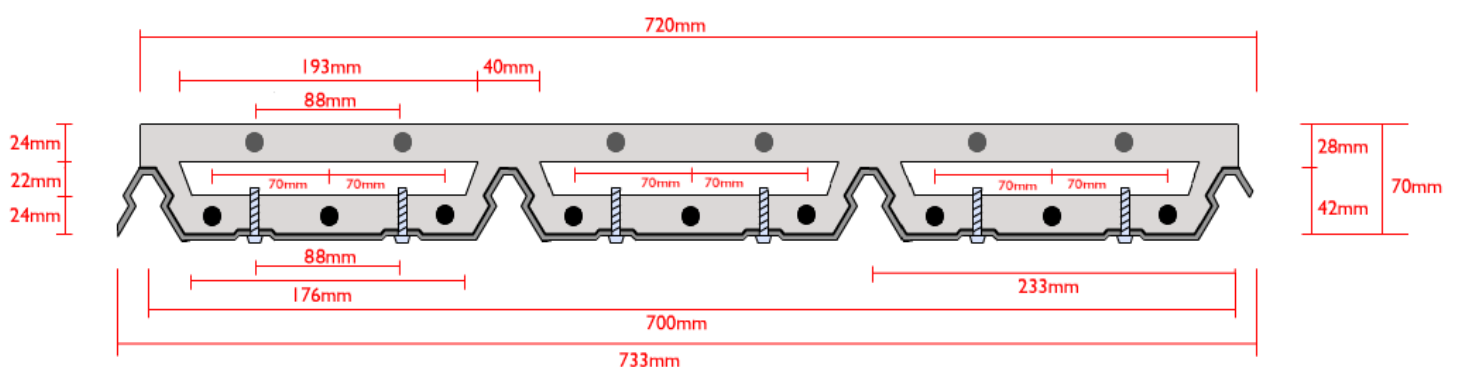

Figure 2 – Cross-sectional configuration of the UHPFRC composite box-cell slabs.

The panel consisted of a steel profile sheet encasing a UHPC slab comprising of multiple layers created by the in-situ placement of expanded polystyrene (EPS) foam prisms within the sectional channels of the sheet. The prefabricated steel profiled sheet (RevKlip 700 0.48 Zincalume) was selected for the panel construction as it provided the necessary depth for reinforcement placement within the upper and lower section layers whilst providing sufficient rigidity for the manufacturing process. The section was proportioned into an upper layer of 24 mm thickness, a central layer (where the EPS sits) of 22 mm thickness, and a bottom layer of 24 mm thickness. The box-cell concept was improved upon by the placement of EPS foam prisms at the location of voids. EPS foam is a lightweight material synonymous with structural insulated panels (SIP) and other composite sandwich systems and is excellent at providing stiffness, thermal insulation and affordability as a conventional material [24]. Moreover, it is pliable and allows penetration of conduit for electrical, gas and other service lines. Screw anchors were placed through the profiled sheet prior to pouring at centre-to-centre spacings of 94 mm. The anchors were embedded through the steel sheet, lower concrete layer, foam prism and a portion of the upper concrete layer to act as shear connectors, ensuring the reduction of slip between the multiple components of the composite panel. The need for providing adequate shear strength is significant in composite structures as it impacts on composite action and load capacity of the structure, and this is more significant for longer spanning and continuous structures [25].

2.2. Test matrix

The test matrix for the tests performed on the six UHPFRC panels is shown in Table 1 and displays the variation of loading direction and reinforcement arrangement for the tests performed.

61

Specimen	Panel dimensions (mm)			Loading face	Reinforcement placement		Reinforcement ratio, ρ_s (%)
	Length	Width	Thickness		Lower layer	Upper layer	
B1-1	1500	733	70	UHPFRC	-	GFRP bar	0.65
B1-2	1500	733	70	Steel Sheet	-	GFRP bar	0.65
B2-1	1500	733	70	UHPFRC	Steel rebar	GFRP bar	1.62
B2-2	1500	733	70	Steel Sheet	Steel rebar	GFRP bar	1.62
B3-1	1500	733	70	UHPFRC	GFRP bar	GFRP bar	1.62
B3-2	1500	733	70	Steel Sheet	GFRP bar	GFRP bar	1.62

Table 1 – Test matrix of one-way box-cell UHPFRC panels.

The first specimen tested, B1-1, had a reinforcement ratio (ρ_s) of 0.65% of the panel cross-sectional area and was achieved by the placement of 6 longitudinal GFRP bars of 8 mm diameter placed in the upper layer of the panel. The second specimen, B1-2, was identical in cross-section to specimen B1-1 but was loaded on the steel face as opposed to the concrete face. This was performed to obtain the 3-point bending capacity of the panel system for both hogging and sagging moments. The third and fourth specimens, B2-1 and B2-2, were similar to specimens B1-1 and B1-2 however the reinforcement ratio of both panels were 1.62% as a result of an additional 9 longitudinal steel bars of 8 mm diameter placed in the lower UHPFRC layer, within the troughs of the steel profile channel. The fifth and sixth specimens, B3-1 and B3-2, are identical to specimens B2-1 and B2-2 however the steel reinforcement is substituted for GFRP. Like specimen B1-1, specimens B2-1 and B3-1 are loaded on the concrete face, and conversely specimens B2-2 and B3-2 are loaded on the steel face. The size of the reinforcement was chosen as it could be placed within the section layers and provide adequate clear cover.

2.3. Materials

2.3.1. *UHPFRC*

A modified version of a UHPFRC mix design developed at the University of Adelaide (mix reference) was used for the current study and the mix proportions are shown in Table 2.

Materials	Mix proportions
Sulfate Resistant Cement	1
Silica Fume	0.226
Sand	1
Water	0.18
Superplasticiser	0.045
Steel fibre	0.185
Water-to-binder ratio (w/c)	0.147

Table 2 – Mix proportions of materials used in UHPFRC mix for current study.

Steel fibres of 13 mm length and 0.2 mm diameter were added to the concrete mix to provide additional compressive strength and ductility. The fibres have a nominal Young's modulus (E_s) and ultimate strength (f_{ult}) of 210 GPa and 2850 MPa, respectively.

To establish the compressive strength (f'_c) and Young's modulus (E_c) of the UHPFRC mix, nine cylinders of 100 mm diameter and 200 mm height were cast, cured and tested in accordance with AS1012.9:2014 [26]. The average 28-day compressive strength was determined to be 110.6 MPa with a standard deviation of 6.1 MPa and a coefficient of variation of 0.058. Moreover, eighteen additional cylinder specimens were cast and tested to measure the compressive strength at 7, 14, 21, 28, 32 and 50 days to establish a maturity curve for the designed UHPFRC mix shown in Fig. 3.
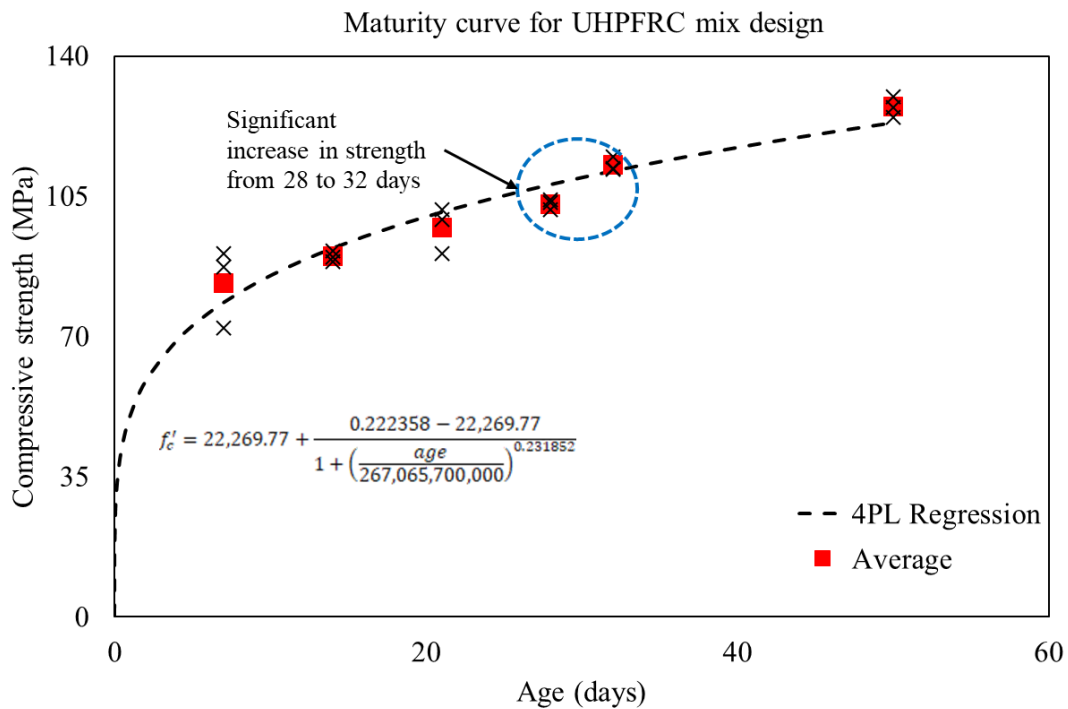
Figure 3 – Maturity curve for UHPFRC mix design.

The maturity curve highlights a relatively lower compressive strength within the first 28 days before rising significantly after 28 days. The cement predominantly (50% - 70%) consists of Ground Granulated Blast Furnace Slag (GGBFS) and this typically results in a delayed onset of strength owing to inadequate alkalinity and hydration of the cement paste [27, 28]. Fig. 3 also displays the regression model for the maturity relationship using a 4-parameter logistic curve with an RMS of 103.4 MPa and R^2 value of 0.992, highlighting the goodness of the regression fit. The average stress-strain relationship of the UHPFRC in compression is shown in Fig. 4.

Figure 4 – Stress-strain relationship of UHPFRC in compression.
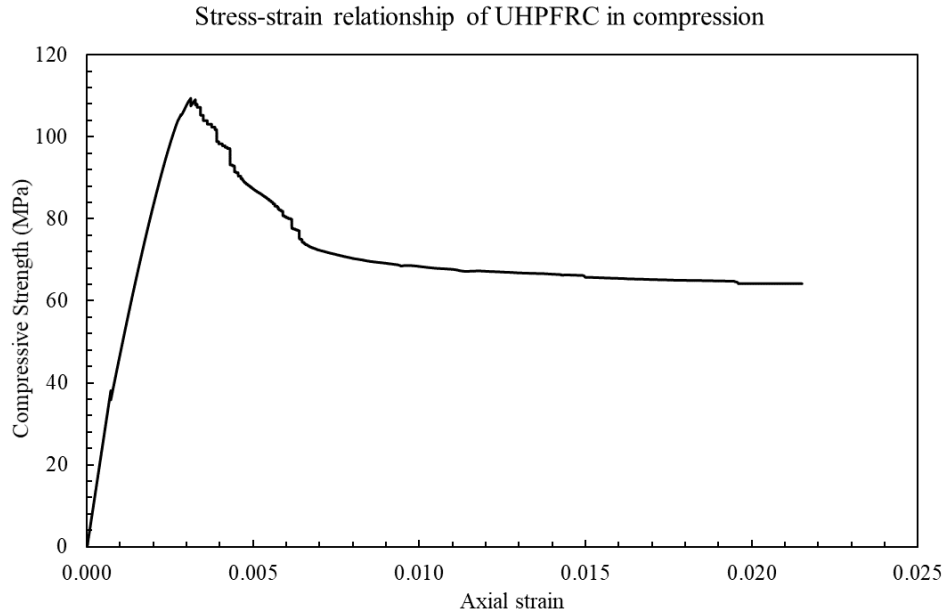
Figure 4 – Stress-strain relationship of UHPFRC in compression.

To obtain the uniaxial tensile behaviour of UHPFRC, nine dog-bone specimens (Figs. 5 (a) – (c)) were horizontally cast and placed under direct tension. The dog-bone specimens include a shanked portion of 120 mm × 120 mm cross-section and 325 mm length. The ends are tapered to produce square ends of 208.6 mm × 208.6 mm and specimen length of 604.8 mm (Fig. 5 (a)). The dimensions are developed by Singh et al. [15] and are alterations to specimens devised by Redaelli [29] and Moreno et al. [30].
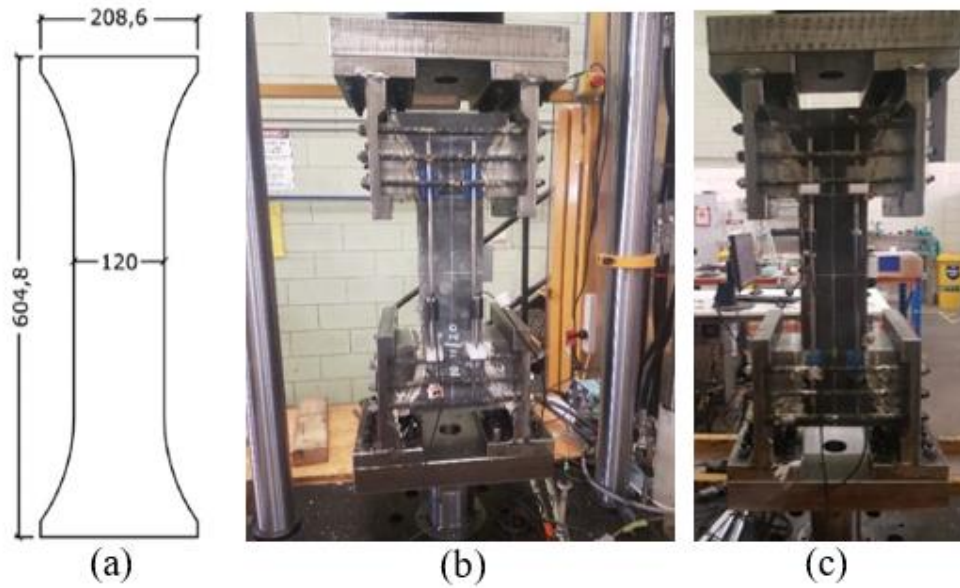
Figure 5 – Direct tension test: a) Dog-bone specimen dimensions [15] (dimensions in mm); b) and c) Direct tension test setup.

The specimens were tested under displacement control at a rate of 0.01 mm/s to a displacement of 2.5 mm before increasing to a rate of 0.05 mm/s to failure. To measure the displacement, four LVDT's were attached to sliding rods bonded to the specimen. The specimens were placed in a specifically designed test rig (Figs. 5 (b) and (c)) to avoid stress concentrations at the bulbed ends. The curved surfaces of the bulbed ends were covered in gypsum paste to ensure even contact between the test jaws and specimen during the loading procedure. The average uniaxial tensile strength (f'_t) was determined to be 3.93 MPa with a standard deviation of 0.32 MPa and a coefficient of variation of 0.123. The average tensile stress-strain relationship in addition to the load-deformation and stress-crack width relationships of the UHPFRC are shown in Figs. 6 (a) – (c).
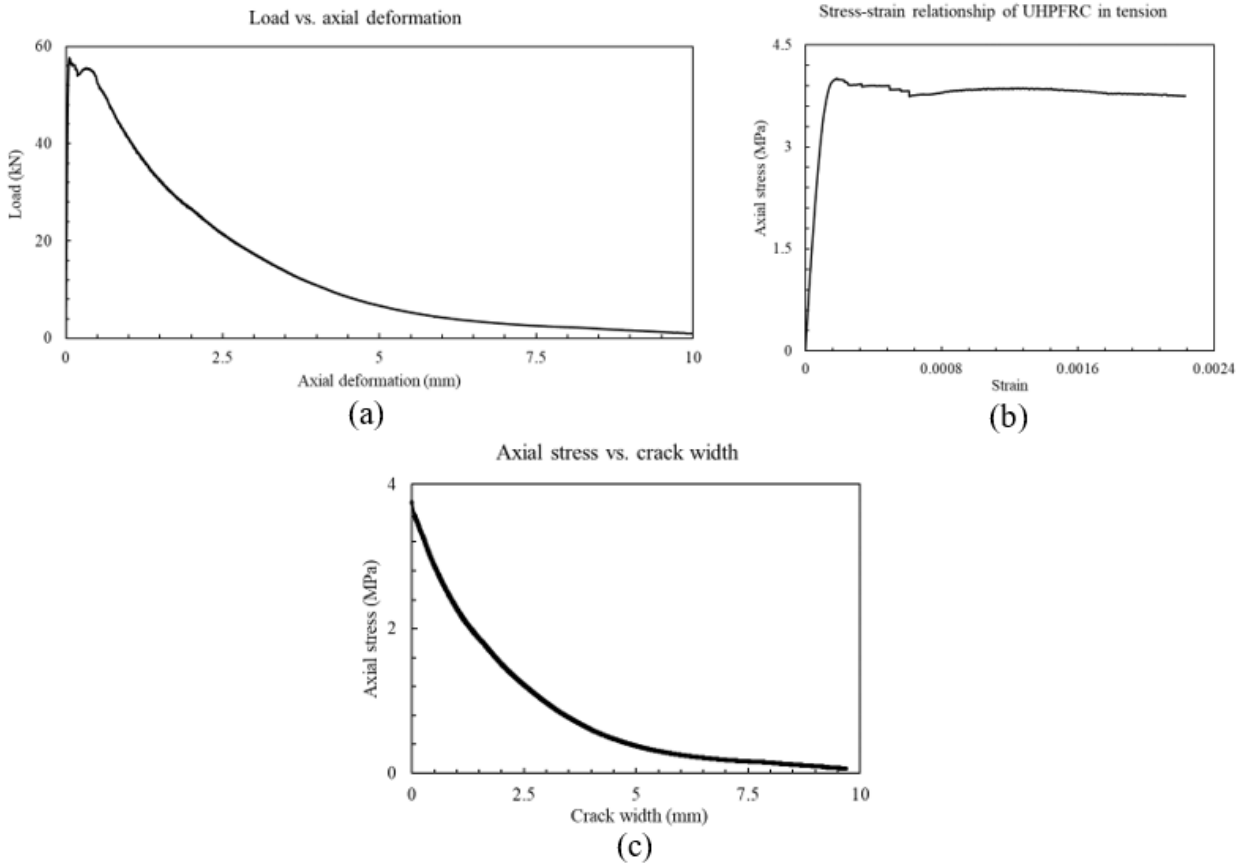
Figure 6 – Tensile properties of UHPFRC: a) load-deformation relationship; b) stress-strain relationship; and c) stress-crack width relationship.

Strains were calculated by taking an average of the LVDT measurements and dividing them over the specimen shank length. Crack widths were estimated by using the LVDT measurements in conjunction with the material properties acquired in the compressive strength test data, using the following equation:

$$s_{cr} = \frac{PL}{E_c A} - \Delta_{total} \tag{1}$$

It was assumed that total deformation of the dog-bone specimen comprised of both elastic and inelastic, and that the inelastic portion was coupled with the cracking width. This assumption

has been previously verified in research on strain and crack width calculations for UHPFRC specimens in tension [31].

2.3.2. *Steel reinforcement and profiled sheet*

Uniaxial tensile tests were conducted on 8 mm diameter, 300 mm length reinforcing steel bar specimens and 0.48 mm thick waterjet-cut coupon specimens. The tensile tests were performed in accordance with AS1391:2007 [32] to establish the stress-strain relationship and quantify the yield and ultimate strengths of the reinforcement bar and profiled sheet, respectively. To prevent warping and torsion, 5 mm thick aluminium tabs were bonded to the grip ends of the steel sheet specimens (Fig. 7). The average yield strength (f_y) of the steel reinforcement was determined to be 412.1 MPa, with an average ultimate strength (f_{ult}) of 508.4 MPa. The average yield strength of the profiled sheet was determined to be 717.8 MPa. Due to the nature of the steel, the profiled sheet did not exhibit a strain hardening phase and was found to be more brittle than the reinforcing bars. The average stress-strain relationship of both the reinforcement and profiled sheet are shown in Fig. 8.
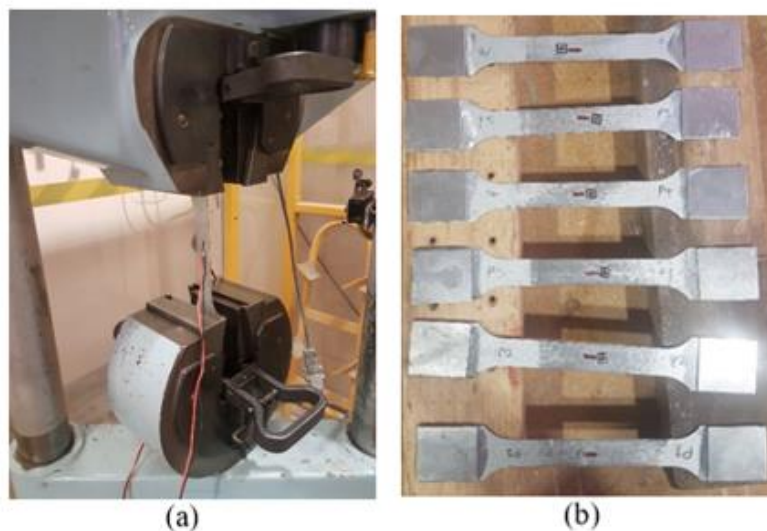

(a)   (b)

Figure 7 – Tensile uniaxial test of profiled steel sheet coupons: a) uniaxial tensile test setup; and b) coupon specimens.
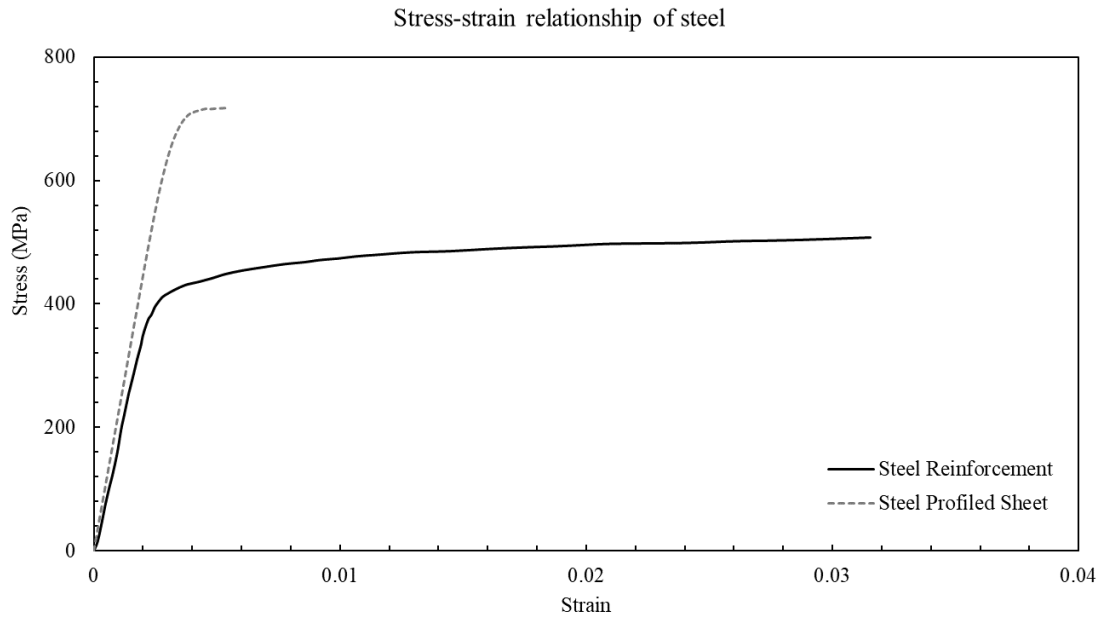
Stress-strain relationship of steel

Figure 8 – Stress-strain relationship of steel reinforcement and profiled sheet.

2.3.3. *GFRP reinforcement*

Uniaxial tensile tests were conducted on 8 mm diameter, 1 m length GFRP bars in accordance with ASTM D7205/D7205M:2006 [33] to establish the stress-strain relationship and quantify the ultimate strength of the reinforcing bars. Steel tubes of 300 mm length, 35 mm outer diameter and 5 mm wall thickness were bonded to the bar ends to act as grip end anchors. The tubes were bonded to the reinforcing bars with two-part epoxy resin and allowed to cure for 24 hours before testing. The average ultimate strength (f_{ult}) of the GFRP was determined to be 931.9 MPa with a standard deviation of 103.6 MPa and coefficient of variation of 0.111. The average stress-strain relationship of the GFRP reinforcement and test specimen setup are shown in Figs. 9 and 10.
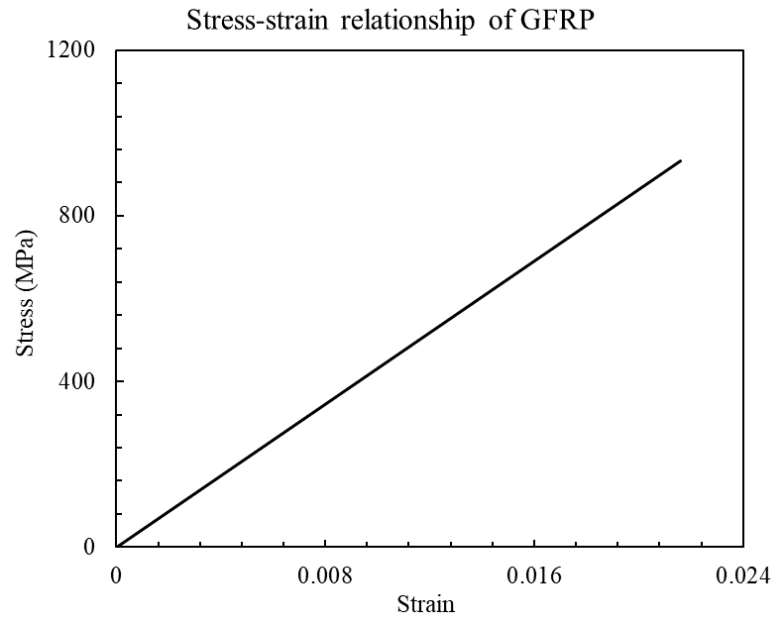
Figure 9 – Stress-strain relationship of GFRP reinforcement.
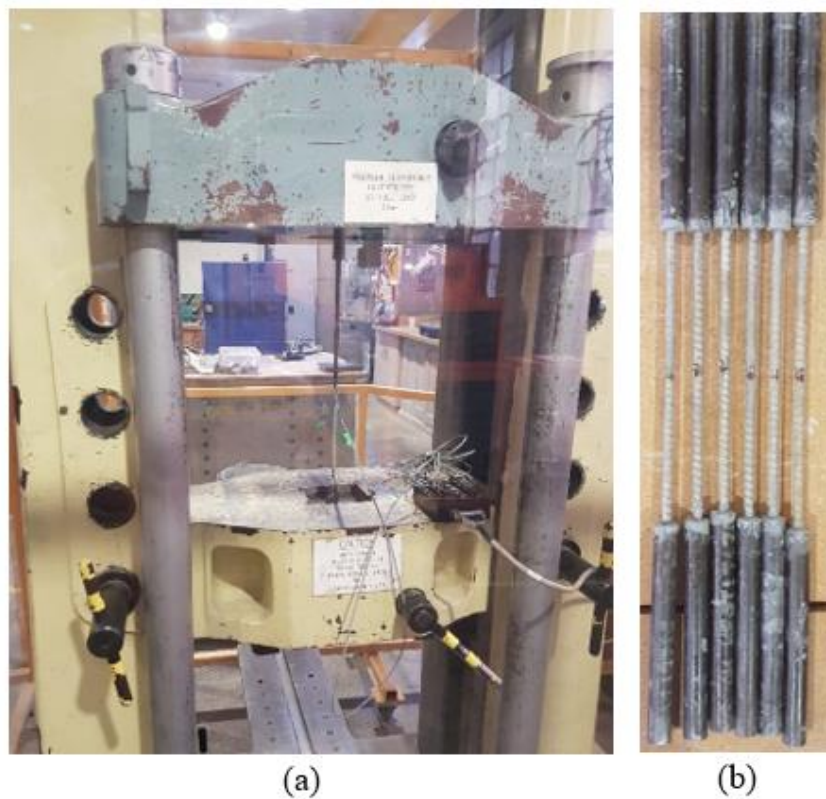

Figure 10 – Tensile uniaxial test on GFRP: a) uniaxial tensile test setup; and b) GFRP specimens.

2.3.4. *EPS foam*

EPS foam used in the box-cell specimens was tested to establish both the compressive and tensile properties. Earlier tests [23] performed on a similar foam provided a tensile and compressive strength of 0.23 MPa and 0.49 MPa, respectively.

2.4. Panel fabrication

The panels were fabricated horizontally using a combination of the profiled steel sheet and plywood as formwork. A shallow plywood box with inner dimensions matching the panel dimensions was built and the prefabricated sheets placed within. To ensure the profile sheet remained level during the casting process, holes were drilled through the formwork base at locations where the screw anchor heads would coincide with the base. Moreover, the base provided support to the steel sheet to prevent buckling failure due to fresh concrete poured on top. The formwork and prefabricated profiled sheet are shown in Fig. 11.

Figure 11 - Formwork and prefabricated profiled steel sheet with connectors.

The profile sheets were prefabricated by drilling 14 mm holes at 94 mm spacings within the profiled sheet channels before installing screw anchors of 12 mm diameter and 50 mm length. The anchors were fitted with rubber grommets at the anchor head and bonded to the profiled sheet with epoxy to ensure the anchors remain vertical during the pouring process. The anchor length was selected to ensure both the foam prisms remained fastened during the pouring process and to provide adequate bond length for shear strength. Moreover, it prevented camber and crushing of the foam prisms due to the fresh concrete exerting uplift.

The first layer was produced by pouring UHPFRC into the channels at a depth of approximately 24 mm. The second layer was a combination of the foam prisms and concrete and required the placement of the foam before the concrete was poured. The foam prisms were aligned centrally within the profile channels before being placed firmly into the screw anchors until the bottom surface was in contact with the first layer of concrete and anchors fully perforated the foam prisms. The second layer was completed by pouring concrete into the voids surrounding the foam prisms. The final layer was produced by pouring the remaining concrete on top of the foam before the top surface was finished by screeding and hand trowelling. The panels were covered by hessian covers 40 minutes after pouring and regularly sprayed with water over 7 days of ambient curing. After 7 days, the panels were demoulded then allowed to cure in ambient conditions for an additional 21 days. The poured and hessian covered specimens are shown in Fig. 12 (a) and (b).
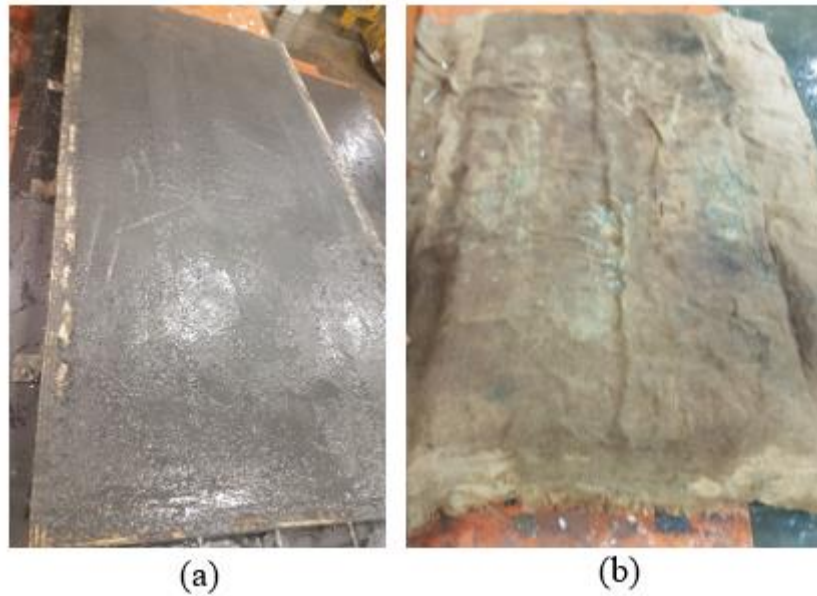
Figure 12 - UHPFRC composite box-cell panels: a) surface-finished panel; and b) hessian mat-covered panel.

2.5. Test setup and instrumentation

The panels were tested under three-point bending with a shear span of 1420 mm and simply supported conditions at the short edges. The loads were applied at the mid-span of each slab through a hydraulic jack to stiffened transfer beams and I-beam (Fig. 13 (a)). The supports were two 40 mm diameter rollers (Fig. 13 (b)) for which 10 mm thick steel plates were placed on. The plates were bonded to the lower surface of the panels and both the plates and loading beam contact areas were coated with gypsum paste to ensure even loading. The hydraulic jack of 1000 kN load capacity applied a monotonically increasing load at a rate of 2 kN/min until the peak load was attained. Thereafter, loading transitioned to displacement control at a displacement rate of 1 mm/min until failure.
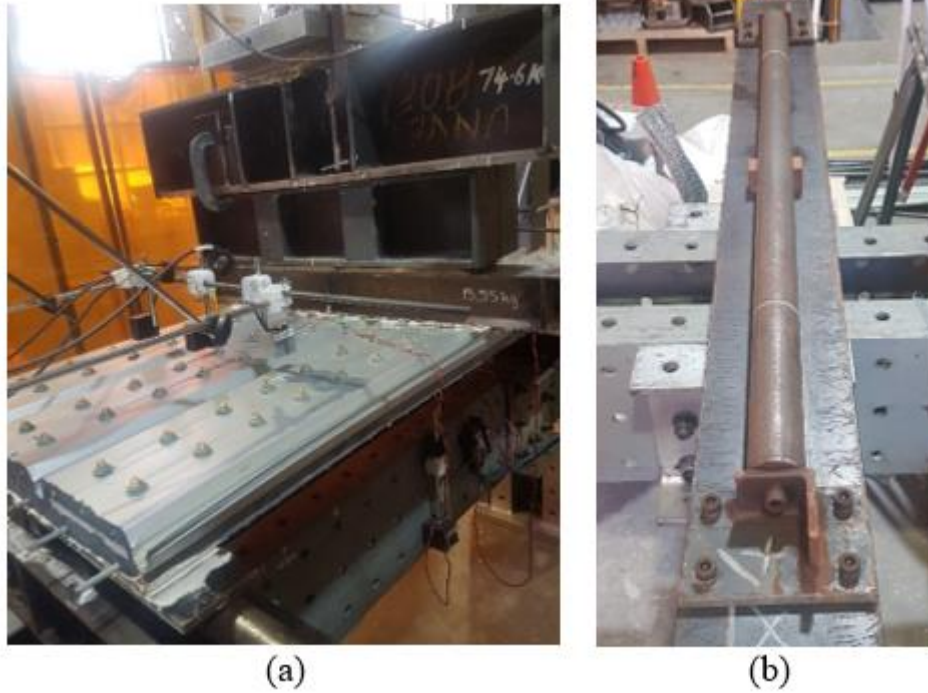
Figure 13 - Test setup of UHPFRC panels: a) Stiffened transfer beams and I-beam for loading; and b) roller supports for panel testing.

To measure slab deflections, a single linear variable differential transducer (LVDT) was mounted on the loading ram and 8 laser sensors were placed along the top surface. Three were mounted at the quarter and three-quarter spans, and two at the midspan (Fig. 14).

Figure 14 - LVDT and laser placement for UHPFRC panel displacement measurement.

Six strain gauges were bonded to the steel sheet and concrete faces to measure strains at the tensile and compressive layers. Four strain gauges were bonded to the top surface, two at the mid-span and one at the quarter and three-quarter spans, respectively. Two strain gauges were bonded to the bottom surface at the mid-span. A strain gauge size of 30 mm was selected for the UHPFRC surfaces, whilst a size of 10 mm was chosen for the steel. Additionally, the surface of the gauges located on the UHPFRC were pre-prepared by spreading a high-strength two-part filler and allowed to cure to ensure a smooth bonding surface.

3. EXPERIMENTAL RESULTS AND DISCUSSION

Table 3 presents a summary of the test results, including peak loads and deflections at the peak loads and at failure for each of the panel specimens.

Specimen	Peak load, P_{max} (kN)	Deflection at peak load, Δ_{peak} (mm)	Deflection at failure, Δ_{max} (mm)
B1-1	47.5	30.4	109.7
B1-2	63.4	55.0	147.2
B2-1	94.4	36.2	100.2
B2-2	61.0	53.3	125.5
B3-1	90.0	52.0	119.8
B3-2	57.1	60.1	135.4

Table 3 - Summary of test results for UHPFRC box-cell panels.

3.1. Load-deflection responses and failure modes

The experimental load-deflection relationships for the UHPFRC panels loaded on the concrete face are shown in Fig. 15. The experimental data illustrates that all three specimens had a similar stiffness in the linear elastic phase, however the stiffness reduced once cracking and delamination begun. Reference specimen B1-1 experienced nonlinear behaviour at a much

75

earlier stage whilst specimen B2-1 exhibited the largest stiffness in the linear elastic phase, owing to the steel reinforcing bars present in the tensile region. Panel specimen B1-1 reached a peak load of 47.5 kN with a deflection of 30.4 mm at the peak load. Early separation of screw anchors from the UHPFRC and foam had begun at an applied load of 25 kN which indicated a reasonable linear-elastic stiffness phase. This was evident from the gap noted between the steel profile and lower layer of UHPFRC when inspected post-testing (Fig. 16 (a)). A tensile crack in the UHPFRC also formed and widened with the increased applied load (Fig. 16 (b)), however owing to the fibres in the concrete matrix, the post-peak ductility was significant and highlighted in Fig. 15. Post-peak behaviour of the panel indicated rupturing of the reinforcement, highlighted by the sudden loss in load-carrying capacity. At failure, the tensile crack propagated to the top face, minor concrete crushing was located at the loading area and a large tensile fracture of the steel profiled sheet at the mid-span (Fig. 16 (c)).

Panel specimen B1-2 reached a peak load of 94.4 kN with a deflection of 36.2 mm at the peak load. The panel exhibited a significant linear-elastic stiffness compared to specimen B1-1, with the first signs of nonlinear behaviour observed at an applied load of 75 kN. At reaching the peak load, a significant loss of load-carrying capacity occurred, owing to rupture of the steel reinforcing bars in the tensile region due to excessive strain before a gradual decrease to failure. Debonding of the UHPFRC from the steel profiled sheet was more evident (Fig. 17 (a)) for this specimen and was a factor in the failure of the panel. Like specimen B1-1, a tensile crack in the UHPFRC formed with the increased applied load, however the propagation of the crack through the panel section was limited to the tensile region and indicates that the neutral axis did not rise significantly through the section profile. Specimen B1-2 failed to a combination of tensile fracture of the steel profiled sheet (Fig. 17 (b)), minor concrete crushing at the top face

(Fig. 17 (b) and (c)), minor crushing of the foam, and major debonding of the UHPFRC from the profiled sheet (Fig. 17 ((a)).

Panel specimen B1-3 reached a peak load of 90 kN with a deflection of 52.2 mm at the peak load. The panel exhibited significant ductility in the pre-peak range with the mid-span deflection at failure 43% greater than panel specimen B1-2. However, two notable features were experienced: an abrupt and substantial loss in load-carrying capacity at the peak load, and the large load-carrying capacity of the section post-failure. The significant loss of load-carrying capacity is due to a rupture of the longitudinal GFRP bars in the tensile region. However, the applied load after rupture was sustained for the duration of the test (15 kN). More significantly, debonding failure was only prevalent in the post-peak phase which indicates the high shear capacity of the panel. However, the severity of the debonding in conjunction with light crushing of the UHPFRC (Figs. 18 (a) and (b)) did not contribute to a reduction of the post-peak capacity of the panel as highlighted in Fig. 18.
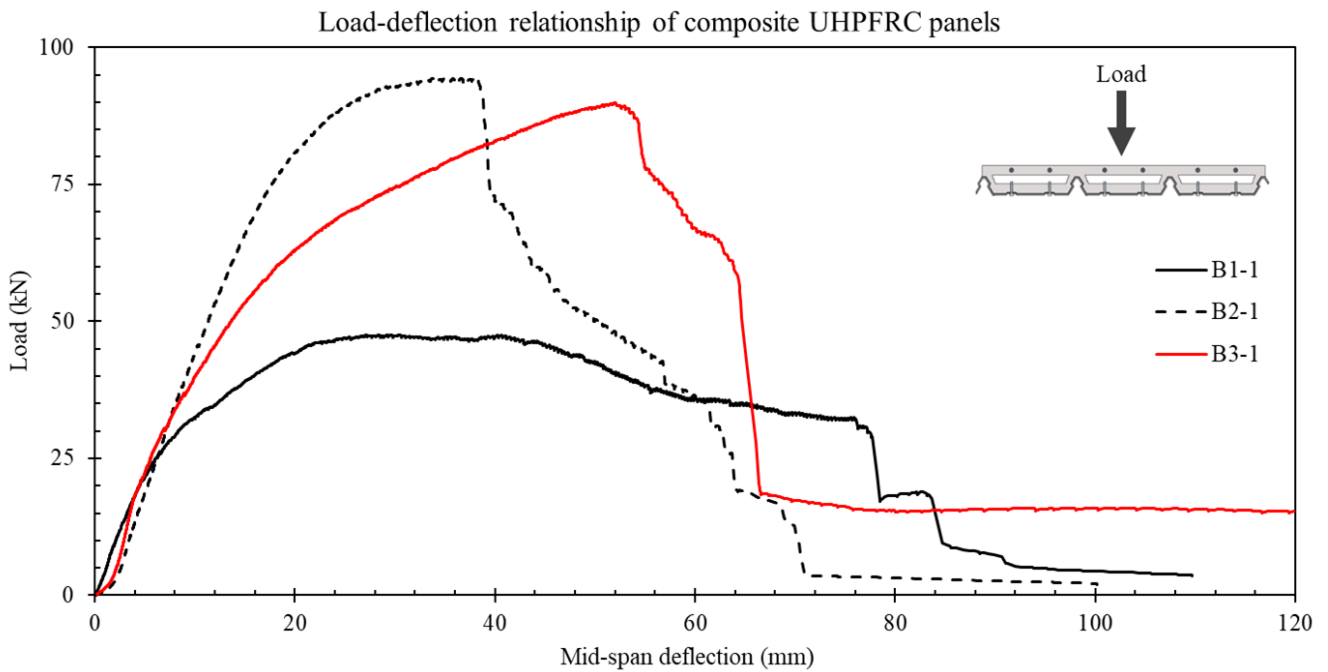
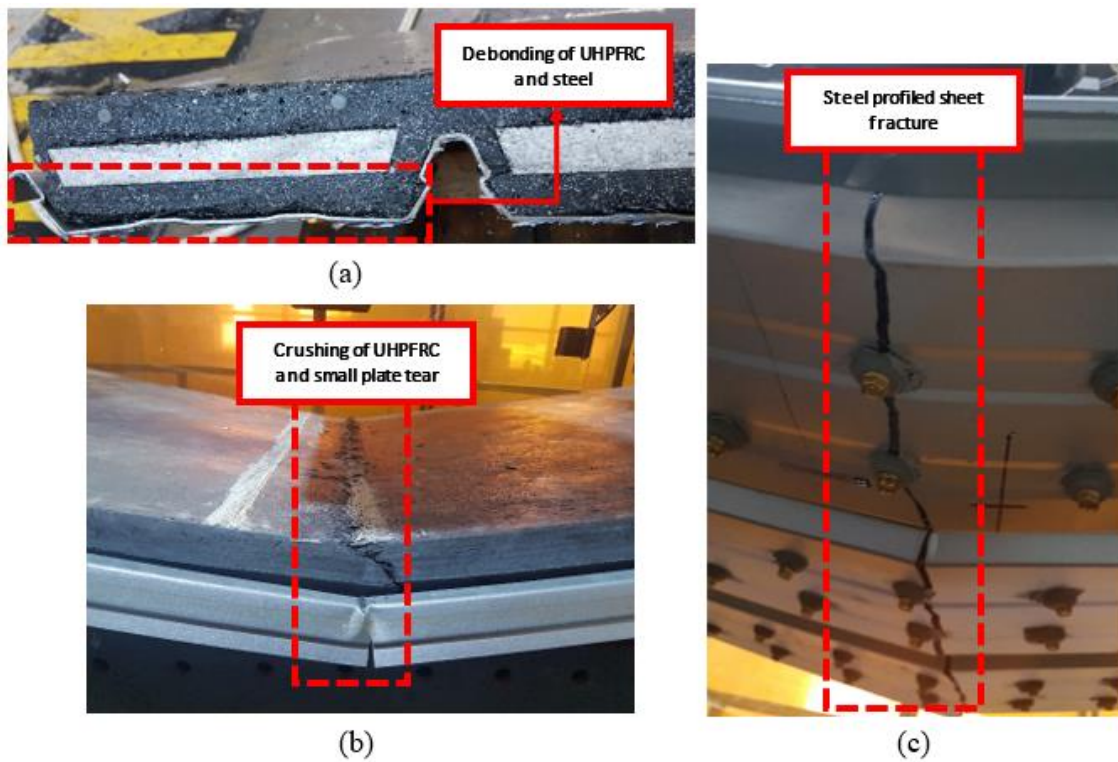**Figure 15 - Load-deflection relationships of UHPFRC panels – loaded on concrete face (positive moment).**

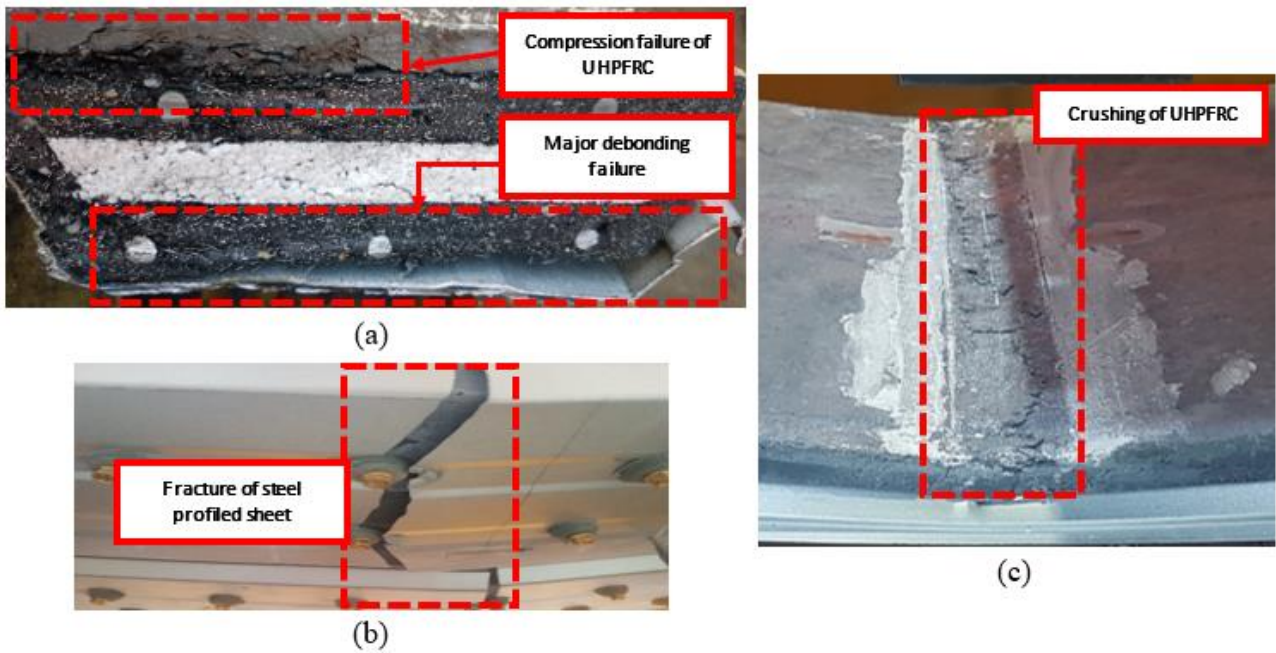**Figure 16 - Failure modes of specimen B1-1.**

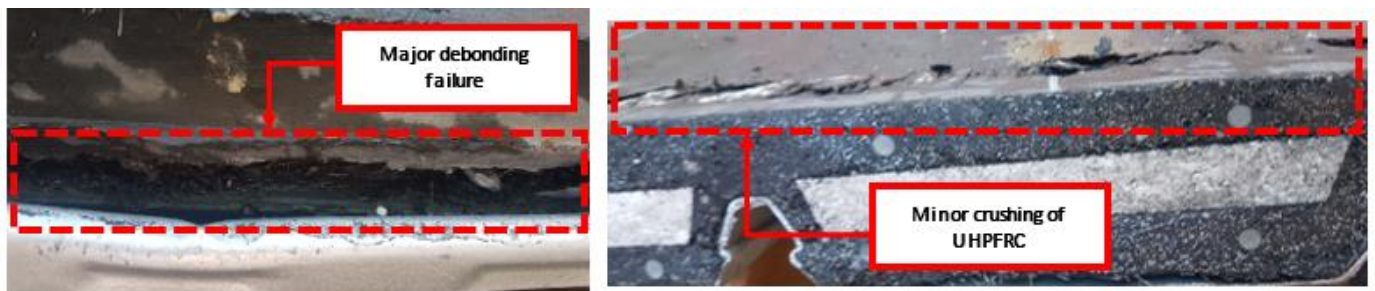**Figure 17 - Failure modes of specimen B2-1.**

Figure 18 - Failure modes of specimen B3-1.

The experimental load-deflection relationships for the UHPFRC panels loaded on the steel face are presented in Fig. 19. The experimental data in demonstrates the near-identical load-deflection behaviour under three-point bending between the three panels. Panel specimen B1-2 reached a peak load of 63.4 kN with a deflection of 55 mm at the peak load. Early signs of cracking in the tensile region were observed at an applied load of 21.5 kN with the initiation of a single crack. Applied load was sustained for a significant duration before consecutive

failure of the tensile longitudinal GFRP reinforcement, indicated by the sharp loss in load-carrying capacity after reaching the peak load and this failure was confirmed when investigating the internal damage of the panel (Fig. 20 (a)). Moreover, the UHPFRC encountered tensile failure and there were signs of crushing of the EPS foam in addition to buckling of the steel profiled sheet (Figs. 20 (b) and (c)).

Panel specimen B2-2 reached a peak load of 61 kN with a deflection of 53.3 mm at the peak load. Like specimen B1-2, signs of cracking in the tensile region were observed at an applied load of 20 kN and indicated the negligible effect of the placement of longitudinal reinforcement in the compressive region within linear-elastic loading. Applied load was sustained for a substantial duration before consecutive failure of the tensile longitudinal GFRP reinforcement, as noted previously in specimen B1-2. However, the load-carrying capacity was rapid and occurred over a much smaller mid-span deflection when compared to the other specimens. The rupture failure of the GFRP reinforcement was seen when investigating the internal damage of the panel (Fig. 21 (a)). However, unlike the previous specimen, there was significant splitting of the concrete cover where the reinforcement was located (Fig. 21 (a)). At failure, there was significant cracking due to the splitting and flexural cracks that had formed (Fig. 21 (b)), along with buckling of the steel plate. A loss in bond between the GFRP and surrounding concrete prism is responsible for cover splitting and subsequent reinforcement rupture which led to the sudden loss in load-carrying capacity after attaining the peak load.

Panel specimen B3-2 reached a peak load of 57.1 kN with a deflection of 60.1 mm at the peak load with signs of cracking in the tensile region observed at an applied load of 21 kN. The load-carrying capacity was significantly reduced as a result of rupturing of the longitudinal GFRP bars. On further examination the tensile failure was severe, with partial pull-out of the concrete

80

at the ruptured end of the GFRP bar (Fig. 22 (a)). Specimen B3-2 exhibited the most severe

flexural cracking, with large cracks surrounded by smaller cracks in the tensile region of the
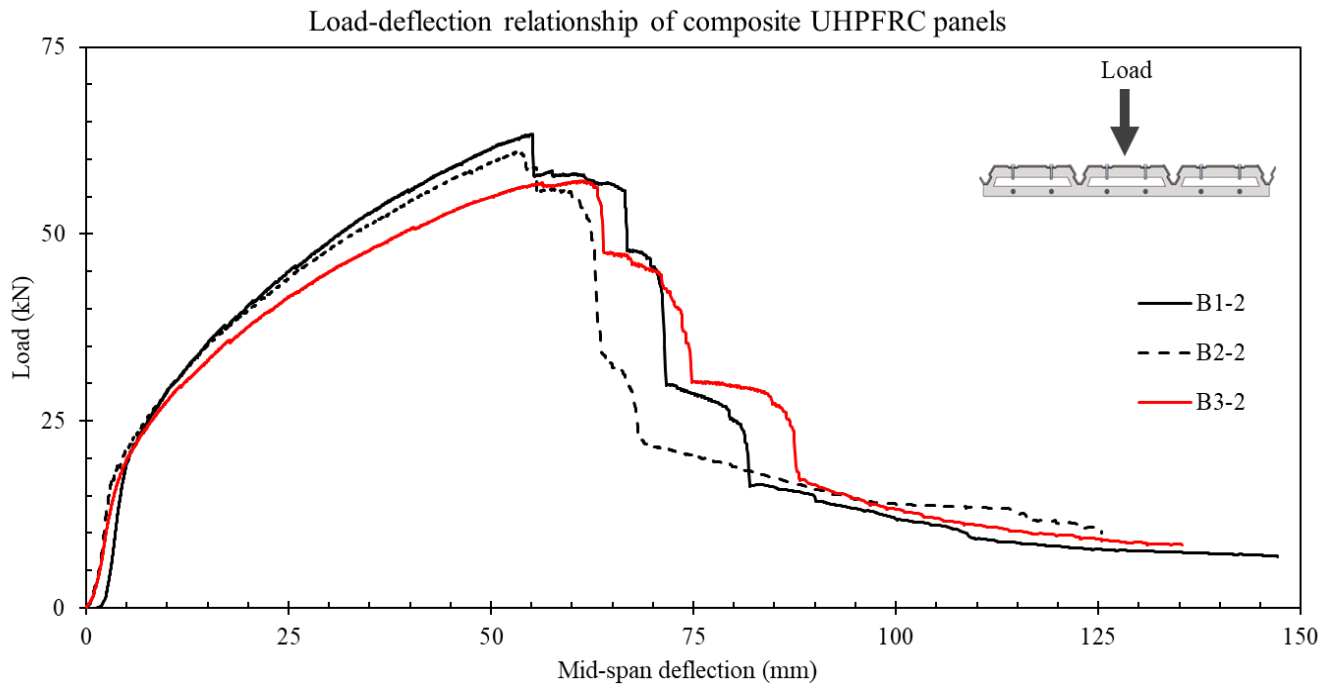
concrete (Figs. 22 (b) and (c)).

Figure 19 - Load-deflection relationships of UHPFRC panels – loaded on steel face (negative moment).
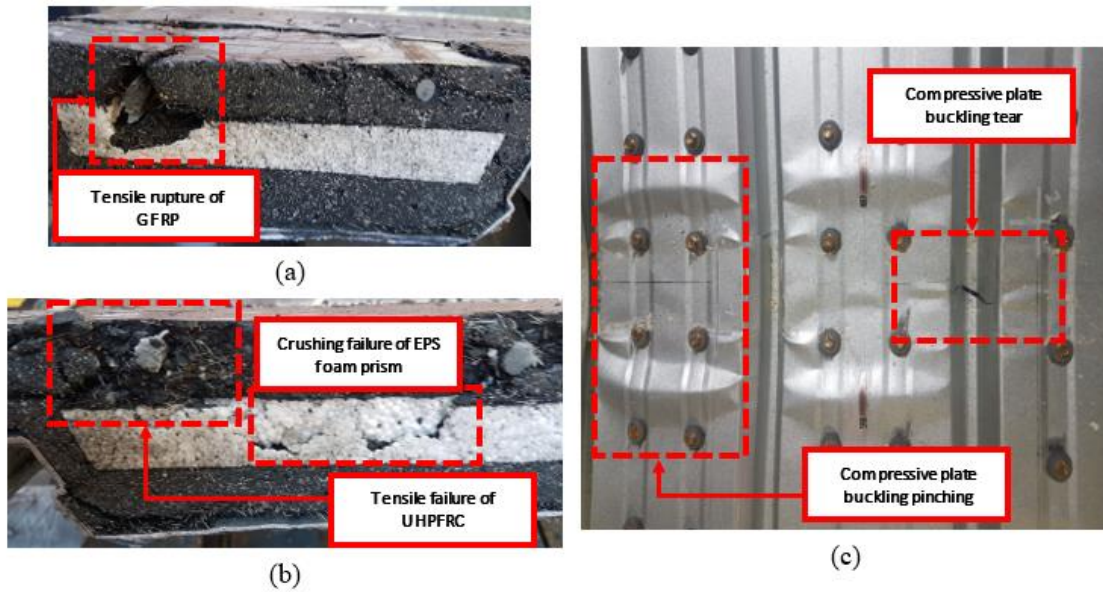
Figure 20 - Failure modes of specimen B1-2: a) Tensile rupture of the longitudinal GFRP reinforcement; b) Tensile cracking of UHPFRC and crushing failure of the EPS foam prism; and c) Compressive plate buckling/pinching and tearing of plate due to buckling within fluted region.
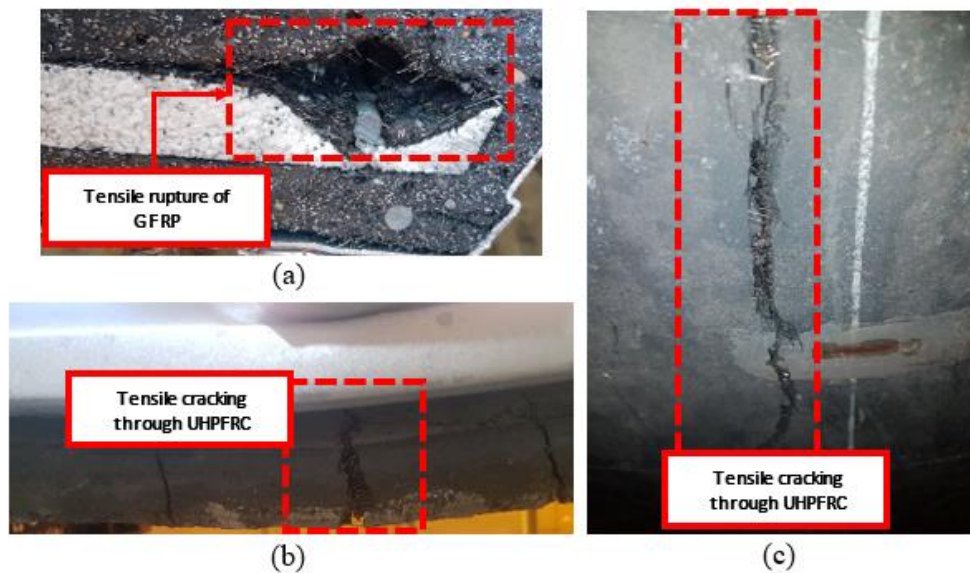

Figure 21 - Failure modes of specimen B2-2: a) Tensile rupture of the longitudinal GFRP reinforcement and splitting of the surrounding concrete cover; and b) Primary crack in UHPFRC layer.
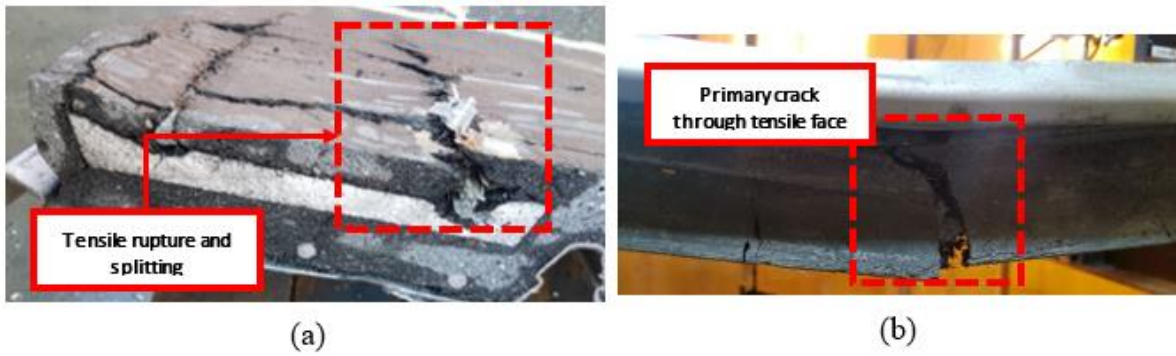
Figure 22 - Failure modes of specimen B3-2: a) Tensile rupture of the longitudinal GFRP reinforcement; b) Primary tensile crack accompanied by secondary cracks in UHPFRC layer; and c) Primary crack in UHPFRC layer.

3.2. Load-strain responses

Figs. 23 (a) – (f) display the load-strain relationship for the top and bottom faces of the composite box-celled panels and locations of the strain gauges with respect to the face geometry. The strains were regularly in compression at the top face and in tension at the bottom face for both loading scenarios, with the exception of the strain gauges placed on the steel face of specimens B1-2, B2-2, and B3-3. The specimens loaded on the concrete face (specimens B1-1, B2-1, and B3-1) experienced an average maximum strain of 2,833 micro-strain (compressive) near the mid-span on the top face (strain gauges SG1 and SG2), and 1,689 and 4,026 micro-strain (tensile) at the quarter-span (strain gauges SG3 and SG4) and mid-span (strain gauges SG3 and SG6) of the bottom face, respectively. The measured maximum strain at the mid-span were slightly less than the failure strains measured in the coupon tests for the steel profiled sheet. It must be noted that strain gauges SG3 and SG4 de-bonded from the steel surface shortly after loading begun and thus no relevant data could be provided. Strains measured for the positively loaded panels were consistent and where strain significantly varied

was an indication of the development of damage in the tension or compression regions. Specimens loaded on the steel face (specimens B1-2, B2-2, and B3-2) experienced an average maximum strain of 3,178 micro-strain near the mid-span on the top face, and 5,790 and 6,484 micro-strain at the quarter-span and mid-span of the bottom face, respectively. The measured yield strains for the concrete matched the values determined from the dog-bone testing, however the strain measured for the panels exceeded the maximum in the stress-strain relationship as it was limited to the point of crack widening. The significant generation of strain for the exceeding load highlights the large ductility of UHPFRC and reinforces the suitability of the material in composite panel design. An observation made for all negatively loaded panels was the reversal of strain state near the loading region. The strain state for all three panels begun in compression, however at approximately 25 kN of applied load, the strain reversed into tension. This highlights the initiation of buckling of steel and the increasing tensile strain and the severity of the buckling previously shown in Fig. 20 (c).
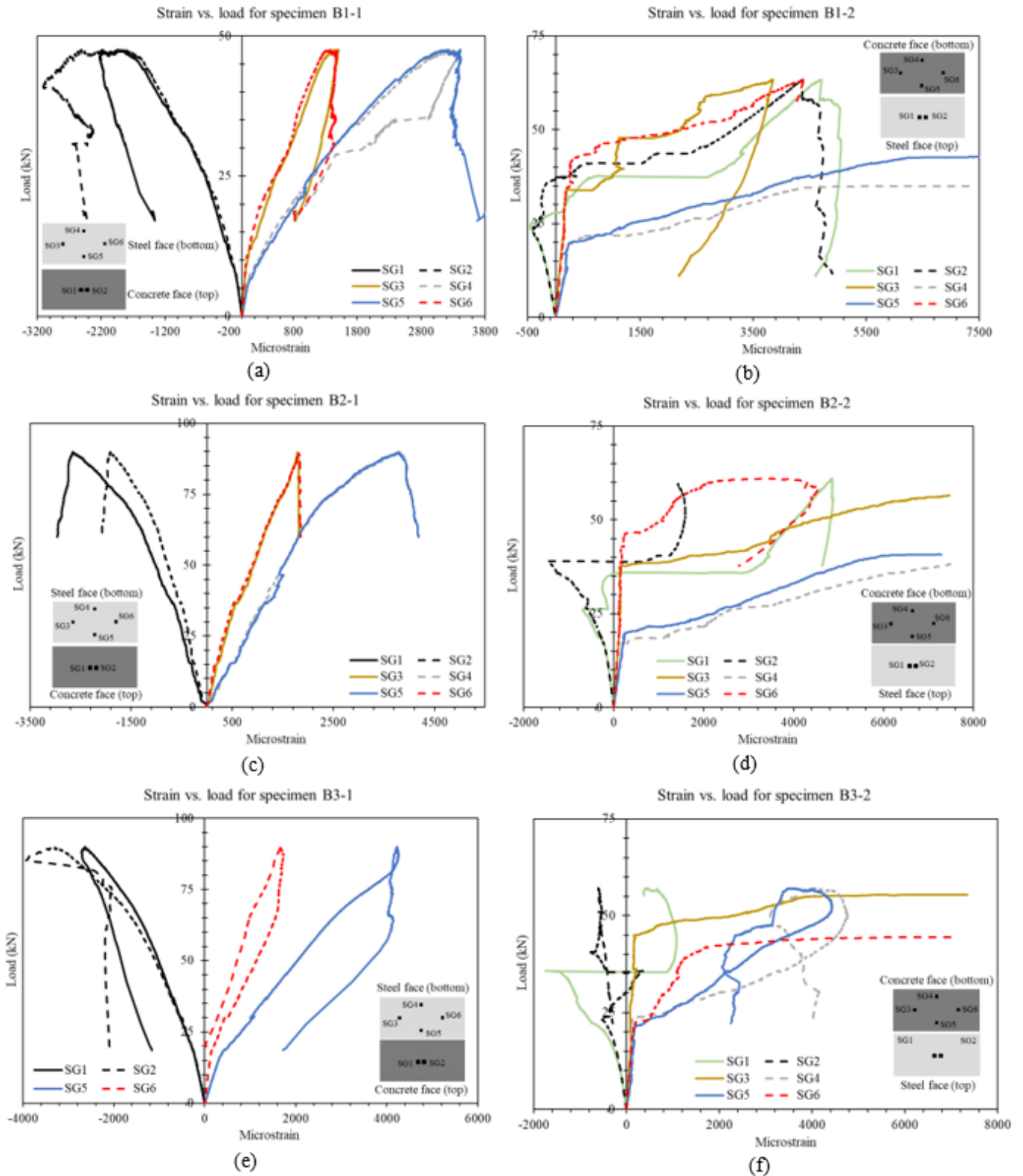
Figure 23 – Load-strain responses for UHPFRC composite panels: a) Specimen B1-1; b) Specimen B1-2; c) Specimen B2-1; d) Specimen B2-2; e) Specimen B3-1; and (f) Specimen B3-2.

3.3. Design considerations

To ascertain the effectiveness of the panel design for residential and commercial structures, a thorough assessment of its strength-to-weight performance, ductility, and both factored loads and deflections for various building codes and standards.

3.3.1. *Strength-to-weight performance and ductility*

Comparisons were made between the panel specimens for strength-to-weight ratios. The panel self-weights were measured and recorded before testing and used in conjunction with the peak loads to obtain the strength-to-weight ratios for each specimen, noted in Table 4.

Specimen	Self-weight, W (kg)	Strength-to-weight ratio	Ductility ratio, $\Delta_{max}/\Delta_{peak}$
B1-1	124.4	39.0	3.61
B1-2	121.6	53.1	2.67
B2-1	125.2	76.8	2.76
B2-2	131.6	47.3	2.36
B3-1	123.0	74.6	2.30
B3-2	120.8	48.2	2.22

Table 4 - Summary of strength-to-weight and ductility ratios for UHPFRC box-cell panels.

Of the specimens loaded on the concrete face, the panel which exhibits the largest strength-to-weight ratio was specimen B2-1 with a ratio of 76.8, however specimen B3-1 closely follows with a ratio of 74.6. The reference specimen B1-1 had a significantly lower ratio owing to a lack of reinforcement in the tensile region. Conversely, of the specimens loaded on the steel face, the panel which exhibited the largest strength-to-weight ratio is specimen B1-2 with a

ratio of 53.1. However, specimens B2-2 and B3-2 had lower strength-to-weight ratios owing to the reinforcement arrangement of the sections. Reference specimen B1-2 had no longitudinal reinforcement in the compression whereas specimens B2-2 and B3-2 contained steel and GFRP reinforcement, respectively. The presence of longitudinal reinforcement in the compression region shifts the neutral axis in the direction of the bottom fibre of the section and less strain is placed on the tensile reinforcement. This was also verified by the load-strain relationships in Fig. 23 when comparing the variation of strain gauge measurements for specimens B1-2, B2-2, and B3-2 on the concrete surface. The results show there is a significant benefit in utilising reinforcement, however the ratio of compressive versus tensile reinforcement must be adjusted to improve the strength of the panel system under negative loading.

Furthermore, comparisons were made between the ductility of the panels, a ratio of the deflection at the peak load was taken with the deflection at failure. Of the specimens loaded on the concrete face, the specimen which displayed the largest ductility was specimen B1-1 with a ratio of 3.61, followed by B2-1 and B3-1 with ratios of 2.76 and 2.36, respectively. However, the ratio in this specific case does not capture the true ductility of specimen B3-1. Due to spatial limitations of the loading frame, load could not be applied beyond the final displacement at the time of testing. The behaviour of the specimen indicates that there would been a prolonged period of resistance before complete loss of load-carrying capacity. Of the specimens loaded on the concrete face, B1-1 displayed the largest ductility with a ratio of 2.36, followed by B2-1 and B3-1 with ratios of 2.30 and 2.22, respectively. The findings indicate the desirability in incorporating a ductile material in steel as tensile reinforcement, however factors such as corrosion and heat resistance need to be considered.

87

3.3.2. *Flexural capacity*

An assessment was performed to check whether the panel system was compliant to live, dead, wind, and combination loading requirements as a structural roofing element. Table 5 summarises design loads and loading combinations for various design standards used in the current study.

Design standards	Load actions (kPa)				Load combinations (kPa)				Maximum equivalent point load, P (kN)
	Live load, Q	Dead load + self-weight, G	Positive wind load, W^+	Negative wind load, W^-	$1.35G$	$0.9G + W_u$	$1.2G + 1.5Q$	$1.2G + 1.6Q + W_u$	
AS 1170.1:2002 [34]	5	2.75*	0.40	1.40	3.71	3.88	10.8	12.7	12.1
ASCE 7-16 [35]	5	2.75*	1.40	2.11	3.71	4.59	10.8	13.4	12.8
Eurocode 2 [36]	5	2.75*	1.48	5.93	3.71	8.41	10.8	16.73	15.9

*Assumed a maximum value of superimposed dead load of 1.5 kPa

Table 5 - Summary of load actions and combinations for various design standards.

Wind loads were calculated by assuming a 50-year occurrence, non-directional wind, densely urban terrain, a building height of 60 m and square plan dimensions of 20 m. Moreover, a zero-angle roof pitch, non-permeable wall conditions, and the panel system acting as a main wind force resisting system (MWFRS) were assumed. The load combinations were upper bound limits to current load assessment standards AS 1170.1 [34], ASCE 7-16 [35], and Eurocode 1 [36] whereas the wind loads were determined using AS 1170.2 [37], ASCE 7-16 [35], and Eurocode 1 [38]. The largest factored pressure was determined to be 16.73 kPa which resulted

in an equivalent point load P of 15.9 kN. Figs. 24 and 25 highlights the position of the equivalent factored load with respect to the load-deflection relationships for both loading scenarios.
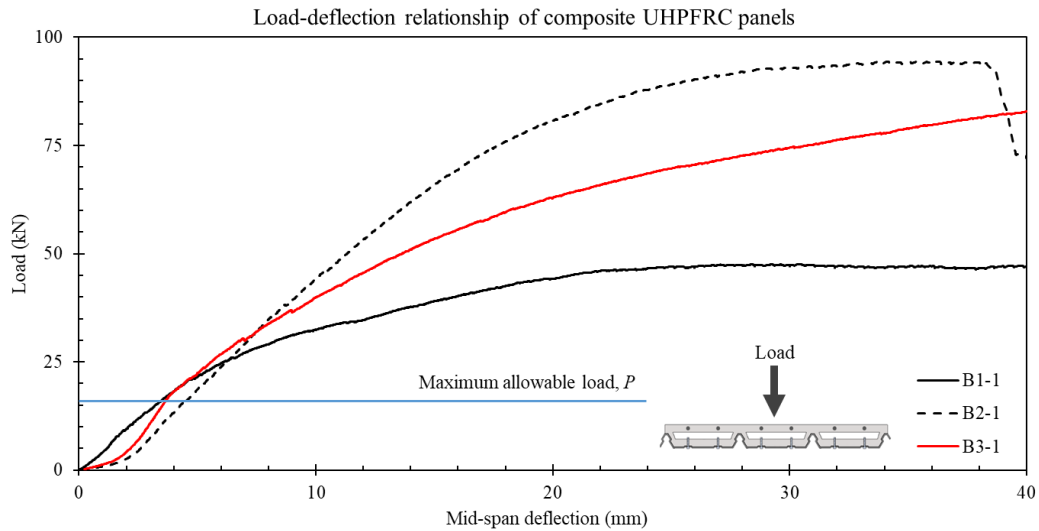

Figure 24 – Comparison of maximum allowable load resulting from factored loading combinations for UHPFRC panel loaded on concrete face.
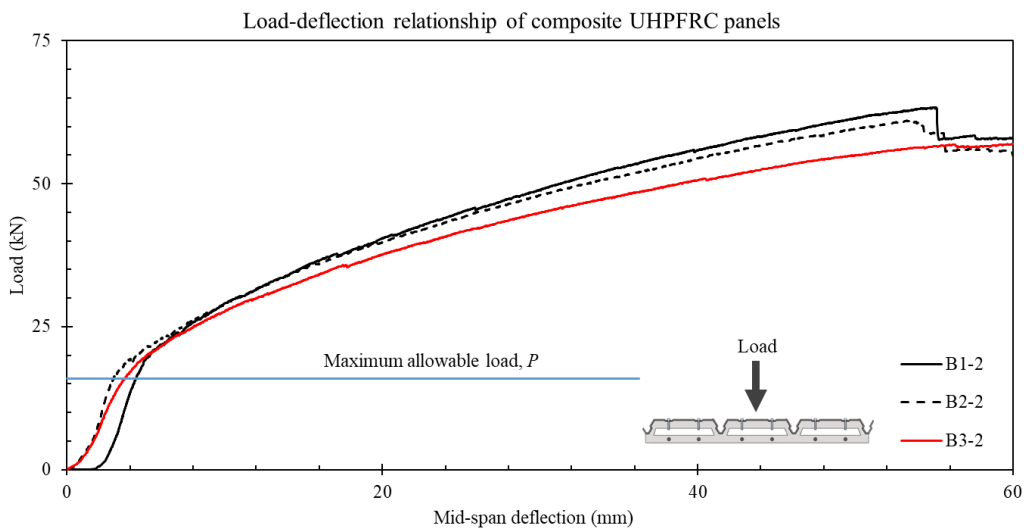

Figure 25 – Comparison of maximum allowable load resulting from factored loading combinations for UHPFRC panel loaded on steel face.

89

The equivalent point load resulting from the load combination remained comfortably within the linear elastic region for both loading configurations, highlighting the compliance of the panel systems with the design standards for varying load actions.

3.3.3. *Deflections*

Design standards were compared for maximum allowable deflections to assess the suitability of the panels under serviceability conditions. Table 6 displays deflection limits and subsequent maximum allowable deflection of the 1420 mm composite shear span for various design standards. Figs. 26 and 27 illustrate the load-deflection relationships shown earlier (Fig. 15) with additional lines to compare the various deflection limits.

Design standards	Maximum allowable deflection limit	Maximum allowable deflection (mm)
AS 3600:2018 [39]	$L^{\wedge}/250$	5.68
ACI 318-19 [40]	$L^{\wedge}/180$	7.89
Eurocode 2 [36]	$L^{\wedge}/250$	5.68
Canadian Building Code 2015 [41]	$L^{\wedge}/360$	3.94

$^{\wedge}$Shear span for slab under simply supported conditions

Table 6 - Summary of maximum allowable deflection limits and associated deflection for various design standards.
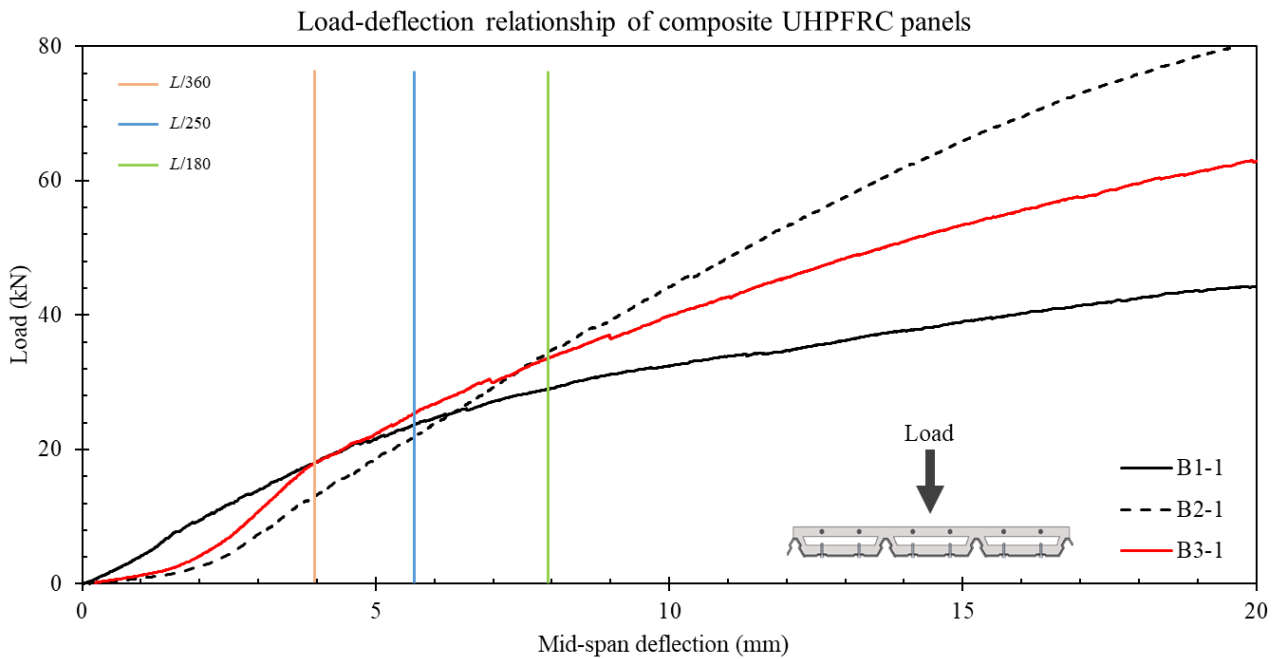
Figure 26 – Comparison of differing limits for maximum allowable deflections for UHPFRC panel loaded on concrete face.
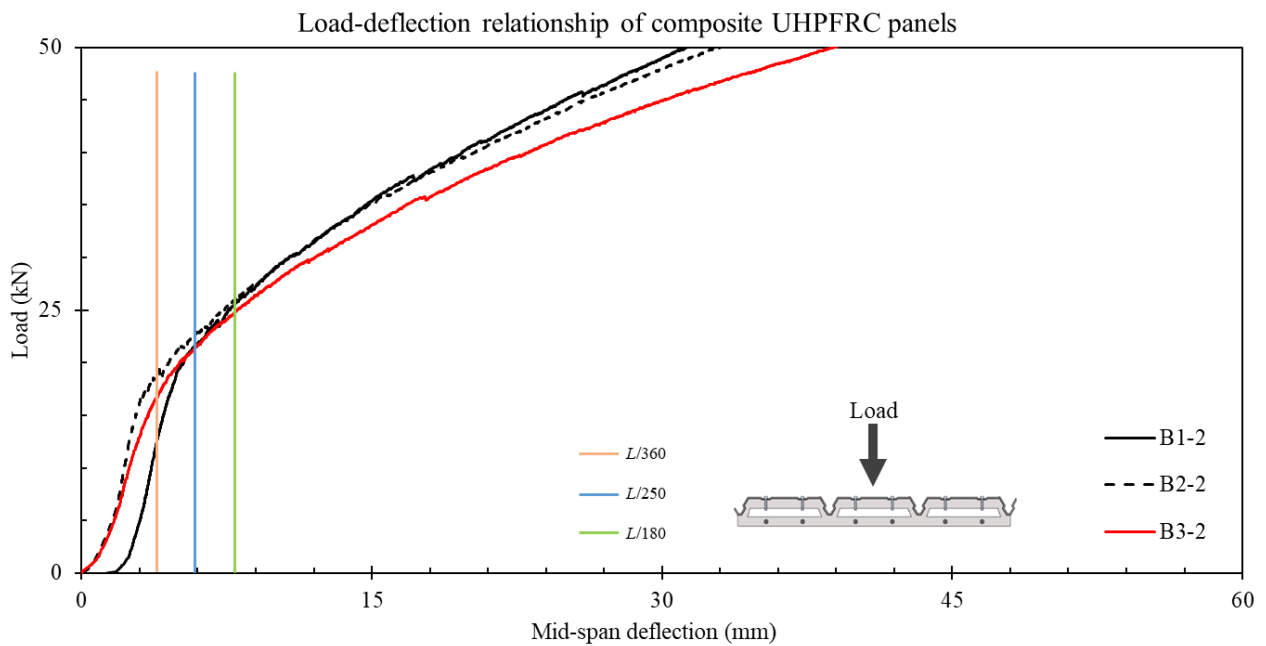

Figure 27 – Comparison of differing limits for maximum allowable deflections for UHPFRC panel loaded on steel face.

For panels loaded on the concrete face, deflections resulting from the limits proposed in the design standards when contrasted to the load-deflection relationship of the panels lie purely within the linear-elastic region for all three specimens. Similarly, permissible maximum deflections for the panels loaded on the steel face lie within the initial elastic phase for the *L*/360 limit for the three specimens, whereas the other two limits were slightly beyond the initial phase of loading. More importantly, neither of these limits were close to the deflection for the peak load. It is clear that the proposed panel system was able to satisfy the deflection limit criterion for control in both the positive and negative bending configurations.

4. CONCLUSIONS

The objective of the present study was to develop innovative box-celled systems based on the box-celled concept. The newly developed panel systems were fabricated by combining the high strength and ductility of UHPFRC with the durability and high performance of GFRP and steel reinforcement. The panels were predominantly tested as one-way slabs and the structural behaviour of the 6 panels were observed through a detailed experimental program. Based on the experimental investigations, it can be concluded that the design philosophy of the panel system can be easily adopted as wind-resistant roofing panels. The following conclusions can be drawn from the study:

(1) The specimens displayed highly ductile behaviour, and more so in the post-failure range,

(2) The screw anchors were able to largely limit de-bonding between the steel profile and concrete slab and prevent shear cracking for a large shear span to depth ratio (> 20:1),

(3) The specimens exhibited large strength-to-weight performance for the specimens reinforced in the section lower layer, and

92

(4) The specimens displayed their compliance to design standards, satisfying requirements for both permissible deflections and load resistance for wind loads and other load combinations.

Recommendations for future research are to develop larger specimens to better understand the structural behaviour of the panel system for long-spanning continuous systems. Moreover, an experimental study should be performed to optimise the reinforcement ratio to balance the tensile and compression zones, and a study should be undertaken to better understand the behaviour of longitudinal GFRP and steel reinforcement with low diameters and clear cover.

ACKNOWLEDGEMENTS

REFERENCES

[1]   D. Dutta, A. Jawdhari, and A. Fam, "A new studded precast concrete sandwich wall with embedded glass-fiber-reinforced polymer channel sections: Part 1, experimental study," PCI Journal, 2020.

[2]   W. A. Thanoon, Y. Yardim, M. Jaafar, and J. Noorzaei, "Structural behaviour of ferrocement–brick composite floor slab panel," Construction and Building materials, vol. 24, no. 11, pp. 2224-2230, 2010.

[3]   M. Al-Kubaisy and M. Z. Jumaat, "Flexural behaviour of reinforced concrete slabs with ferrocement tension zone cover," Construction and Building Materials, vol. 14, no. 5, pp. 245-252, 2000.

[4]   Y. Yardim, A. Waleed, M. S. Jaafar, and S. Laseima, "AAC-concrete light weight precast composite floor slab," Construction and Building materials, vol. 40, pp. 405-410, 2013.

[5]   A. Upadyay and V. Kalyanaraman, "Simplified analysis of FRP box-girders," Composite structures, vol. 59, no. 2, pp. 217-225, 2003.

[6]   I. Balázs, J. Melcher, and A. Belica, "Experimental investigation of torsional restraint provided to thin-walled purlins by sandwich panels under uplift load," Procedia Engineering, vol. 161, pp. 818-824, 2016.

[7]   A. Baskaran, S. Molleti, S. Ko, and L. Shoemaker, "Wind uplift performance of composite metal roof assemblies," Journal of architectural engineering, vol. 18, no. 1, pp. 2-15, 2012.

[8]   E. A. Sayyafi, A. Chowdhury, and A. Mirmiran, "A super lightweight hurrican-resistant thin-walled box-cell roofing system," in International Symposium on Structural Engineering, 2016, pp. 698-704.

[9]   E. A. Sayyafi, A. G. Chowdhury, and A. Mirmiran, "Innovative Hurricane-Resistant UHPC Roof System," Journal of Architectural Engineering, vol. 24, no. 1, p. 04017032, 2017.

[10]   P. Richard and M. Cheyrezy, "Reactive powder concrete with high ductility and 200-800 MPa compressive strength. ACI Spring Convention, San Francisco, SP. 144-24," Richard, P. and Cheyrezy, MH,(1995).. Composition of reactive powder concretes. Cement and Concrete Research, vol. 25, no. 7, pp. 1501-1511, 1994.

[11]   P. Richard and M. Cheyrezy, "Reactive powder concrete," Cement and Concrete Research, vol. 25, no. 7, pp. 1501-1511, 1995.

[12]   Y. L. Voo and S. J. Foster, "Characteristics of ultra-high performance 'ductile'concrete and its impact on sustainable construction," The IES Journal Part A: Civil & Structural Engineering, vol. 3, no. 3, pp. 168-187, 2010.

[13]   R. Yu, P. Spiesz, and H. Brouwers, "Mix design and properties assessment of ultra-high performance fibre reinforced concrete (UHPFRC)," Cement and concrete research, vol. 56, pp. 29-39, 2014.

[14]   H. R. Sobuz, D. J. Oehlers, P. Visintin, N. M. S. Hasan, M. I. Hoque, and A. S. M. Akid, "Flow and Strength Characteristics of Ultra-high Performance Fiber Reinforced Concrete: Influence of Fiber Type and Volume-fraction," Journal of Civil Engineering and Construction, vol. 6, no. 1, pp. 15-21, 2017.

[15]   M. Singh, A. Sheikh, M. M. Ali, P. Visintin, and M. Griffith, "Experimental and numerical study of the flexural behaviour of ultra-high performance fibre reinforced concrete beams," Construction and Building Materials, vol. 138, pp. 12-25, 2017.

[16]   H. Sobuz, P. Visintin, M. M. Ali, M. Singh, M. Griffith, and A. Sheikh, "Manufacturing ultra-high performance concrete utilising conventional materials and production methods," Construction and Building materials, vol. 111, pp. 251-261, 2016.

[17]   P. Visintin, M. M. Ali, T. Xie, and A. Sturm, "Experimental investigation of moment redistribution in ultra-high performance fibre reinforced concrete beams," Construction and Building Materials, vol. 166, pp. 433-444, 2018.

[18]   A. Hassan, S. Jones, and G. Mahmud, "Experimental test methods to determine the uniaxial tensile and compressive behaviour of ultra high performance fibre reinforced concrete (UHPFRC)," Construction and building materials, vol. 37, pp. 874-882, 2012.

[19]   Z. Wu, C. Shi, W. He, and L. Wu, "Effects of steel fiber content and shape on mechanical properties of ultra high performance concrete," Construction and building materials, vol. 103, pp. 8-14, 2016.

[20]   D.-Y. Yoo, H.-O. Shin, J.-M. Yang, and Y.-S. Yoon, "Material and bond properties of ultra high performance fiber reinforced concrete with micro steel fibers," Composites Part B: Engineering, vol. 58, pp. 122-133, 2014.

[21]   R. Lameiras, J. Barros, I. B. Valente, and M. Azenha, "Development of sandwich panels combining fibre reinforced concrete layers and fibre reinforced polymer connectors. Part I: Conception and pull-out tests," Composite Structures, vol. 105, pp. 446-459, 2013.

[22]   H. Wright, H. Evans, and P. Harding, "The use of profiled steel sheeting in floor construction," Journal of Constructional Steel Research, vol. 7, no. 4, pp. 279-295, 1987.

[23]   S. Mahdi, M. M. Ali, A. Sheikh, M. Elchalakani, and T. Xie, "An Investigation Into the Feasibility of Normal and Fibre-Reinforced Ultra-High Performance Concrete Multi-Cell and Composite Sandwich Panels," Journal of Building Engineering, p. 102728, 2021.

[24]   R. O'Hegarty, A. Reilly, R. West, and O. Kinnane, "Thermal investigation of thin precast concrete sandwich panels," Journal of Building Engineering, vol. 27, p. 100937, 2020.

[25]   D. J. Oehlers, N. T. Nguyen, M. Ahmed, and M. A. Bradford, "Partial interaction in composite steel and concrete beams with full shear connection," Journal of Constructional Steel Research, vol. 41, no. 2-3, pp. 235-248, 1997.

[26]   AS, "Methods of testing concrete—Determination of the static chord modulus of elasticity and Poisson's ratio of concrete specimens," 1997.

[27]   C. Korde, M. Cruickshank, R. P. West, and C. Pellegrino, "Activated slag as partial replacement of cement mortars: Effect of temperature and a novel admixture," Construction and Building Materials, vol. 216, pp. 506-524, 2019.

[28]   M. Soutsos, A. Hatzitheodorou, J. Kwasny, and F. Kanavaris, "Effect of in situ temperature on the early age strength development of concretes with supplementary cementitious materials," Construction and Building Materials, vol. 103, pp. 105-116, 2016.

[29]   D. Redaelli, "Testing of reinforced high performance fibre concrete members in tension," in Proceedings of the 6th Int. Ph. D. Symposium in Civil Engineering, Zurich 2006, 2006, no. CONF, p. 8: Proceedings of the 6th Int. Ph. D. Symposium in Civil Engineering, Zurich 2006.

[30]   D. Moreno, W. Trono, G. Jen, C. Ostertag, and S. Billington, "Tension-stiffening in reinforced high performance fiber-reinforced cement-based composites under direct tension," in High Performance Fiber Reinforced Cement Composites 6: Springer, 2012, pp. 263-270.

[31]   P. Visintin, A. Sturm, M. Mohamed Ali, and D. Oehlers, "Blending macro-and micro-fibres to enhance the serviceability behaviour of UHPFRC," Australian Journal of Civil Engineering, vol. 16, no. 2, pp. 106-121, 2018.

[32]   Metallic materials—Tensile testing at ambient temperature, 2007.

[33]   Standard Test Method for Tensile Properties of Fiber Reinforced Polymer Matrix Composite Bars, 2006

[34]   AS 1170.1:2011 - Structural design actions - Permanent, imposed and other actions, 2011.

[35]   Minimum Design Loads and Associated Criteria for Buildings and Other Structures (ASCE/SEI 7-16), 2016.

[36]   Eurocode 2: Design of concrete structures - Part 1-1: General rules and rules for buildings, 2004.

[37]   AS 1170.2:2011 - Structural design actions - Wind actions, 2011.

[38]   Eurocode 1: Actions on structures, 2002.

[39]   AS 3600:2018, 2018.

[40]   Building Code Requirements for Structural Concrete (ACI 318-19): An ACI Standard: Commentary on Building Code Requirements for Structural Concrete (ACI 318R-19), an ACI Report, 2019.

[41]   National Building Code of Canada 2015, 2015.

THIS PAGE HAS BEEN LEFT INTENTIONALLY BLANK

CHAPTER 3

Background

In this chapter, an experimental program is performed to evaluate the bond-slip behaviour of helically ribbed GFRP within UHPFRC. This was performed having observed the helically ribbed reinforcement to be significantly influential on the structural performance of the box-celled composite panel. The behaviour of the helically ribbed GFRP and steel reinforcement embedded in UHPFRC is observed experimentally for various cover conditions and then used in conjunction with existing bond-slip models to develop a multi-variable bond-slip relationship. The results are compared to the steel reinforcement followed by a parametric study to observe the model variation for its key parameters.

List of manuscripts

Mahdi, S., Ali, M. M. & Sheikh, A. H. (2021). "Experimental investigation on the bond-slip behaviour of helically ribbed GFRP embedded in ultra-high performance concrete." Submitted to *Journal of Composites for Construction*.

Statement of Authorship

Title of Paper	Experimental investigation on the bond-slip behaviour of helically ribbed GFRP embedded in ultra-high performance concrete
Publication Status	☐ Published ☐ Accepted for Publication ☑ Submitted for Publication ☐ Unpublished and Unsubmitted work written in manuscript style
Publication Details	Mahdi, S., Ali, M. M. & Sheikh, A. H. (2021). "Experimental investigation on the bond-slip behaviour of helically ribbed GFRP embedded in ultra-high performance concrete." Submitted to *Journal of Composites for Construction*.

Principal Author

Name of Principal Author (Candidate)	Shahin Mahdi		
Contribution to the Paper	Conceptualisation, methodology, data curation, model development, and manuscript writing and revision		
Overall percentage (%)	50		
Certification	This paper reports on original research I conducted during the period of my Higher Degree by Research candidature and is not subject to any obligations or contractual agreements with a third party that would constrain its inclusion in this thesis. I am the primary author of this		
Signature		Date	29/12/2021

Co-Author Contributions

Name of Co-Author	Mohamed Sadakkathulla Mohamed Ali		
Contribution to the Paper	Supervision, conceptualisation, methodology, data curation, model development, and manuscript writing and revision (25%)		
Signature		Date	29/12/2021

Name of Co-Author	Abdul Hamid Sheikh		
Contribution to the Paper	Supervision, conceptualisation, methodology, data curation, model development, and manuscript writing and revision (25%)		
Signature		Date	29/12/2021

Experimental investigation on the bond-slip behaviour of helically ribbed GFRP embedded in ultra-high performance concrete

S. Mahdi[1*], M.S. Mohamed Ali[2,] A.H. Sheikh[3]

[1]Mr. Shahin Mahdi (Corresponding author)

Ph.D. Candidate

School of Civil, Environmental and Mining Engineering

The University of Adelaide

South Australia 5005

AUSTRALIA

Email: shahin.mahdi@adelaide.edu.au

[2]Dr. Mohamed Sadakkathulla Mohamed Ali

Senior Lecturer

School of Civil, Environmental and Mining Engineering

The University of Adelaide

South Australia 5005

AUSTRALIA

Email: mohamed.mohamedsadakkathulla@adelaide.edu.au

[3]Associate Professor Abdul Hamid Sheikh

Associate Professor

School of Civil, Environmental and Mining Engineering

The University of Adelaide

South Australia 5005

AUSTRALIA

Email: abdul.sheikh@adelaide.edu.au

Experimental investigation on the bond-slip behaviour of helically-ribbed GFRP embedded in ultra-high performance concrete

S. Mahdi[1*], M.S. Mohamed Ali[2,] A.H. Sheikh[3]

ABSTRACT

The interaction between ribbed reinforcement and the cementitious material it is embedded in is fundamental for the analysis and design of reinforced concrete structures. Studies on bond-slip behaviour for fibre reinforced polymers (FRP) have concentrated on FRP types and surrounding cementitious material, however studies on the effect reinforcement surface are sparse. An emerging aspect of this field is the development of helically ribbed glass fibre reinforced polymer (GFRP) reinforcement. The present study investigates the experimental behaviour of helically ribbed GFRP reinforcement embedded in ultra-high performance concrete (UHPC) blended with discontinuous high-strength steel fibres. Seven GFRP reinforcement specimens, manufactured by MateenBar™, in addition to seven high-strength steel reinforcement, are cast in differing positions within a UHPC block and tested under pull-out conditions. The local bond-slip relationships of the GFRP and steel specimens were experimentally evaluated, and existing theoretical models were reviewed to develop a new multi-variable bond-slip model for helically ribbed GFRP embedded in UHPC.

Keywords: ultra-high performance concrete (UHPC); glass fibre-reinforced polymer (GFRP); bond-slip; bond stress; steel reinforcement; discontinuous steel fibre.

INTRODUCTION

A critical mechanism of all reinforced concrete members is the bond relationship between the reinforcement and the surrounding concrete. The bond between reinforcement and concrete controls the tension-stiffening, cracking, and deflection behaviour at the serviceability limit

state and is crucial for anchorage development at the ultimate limit state (Cosenza et al. 2002). Moreover, inadequate bond resistance between reinforcement and concrete leads to early onset failure of the member by reduction of both flexural and shear capacities (Yoo et al. 2015). The best representation of this mechanism is the bond strength – slip relationship, where the stress between reinforcement and concrete becomes a function of the relative slip between the two materials. There is extensive literature in both experimental studies and analytical models developed to predict the bond behaviour of reinforcement embedded in concrete. Reinforcement embedded in regular strength concrete has been widely studied, however the advent of high strength concrete, varying reinforcement materials and bar surfaces, and the addition of discontinuous fibres adds to the complexity in modelling bond behaviour.

Ultra-high performance concrete (UHPC) is one such concrete, providing significantly higher durability, tensile and compressive strength to regular concrete (Khaksefidi et al. 2021). However, UHPC exhibits brittle failure post-cracking under tension (Wiemer et al. 2020). The inclusion of discontinuous steel fibres in UHPC minimises such behaviour and further increases tensile and compressive strengths in addition to post-cracking ductility under tensile stress via micro-crack bridging by the fibres (Bae and Pyo 2020, Larsen and Thorstensen 2020). Preliminary research in reinforcement bond behaviour for fibre-blended UHPC was performed by Reineck and Greiner (2004), and Jungwirth and Muttoni (2004) where steel reinforcements of various sizes and embedment lengths were subjected to pull-out tests. The studies identified the relationship between embedment length and reinforcing bar stress and discovered bond lengths greater than two bar diameters result in yield or rupture of the bar (Sturm and Visintin 2019). Subsequent studies by Yoo et al. (2014a, 2014b), Oesterlee (2010), and Marchand et al. (2016) investigated the effect of specimen age, fibre content ratio, and both cyclic and monotonic loading on the bond – slip behaviour. However, studies into the behaviour of glass

fibre-reinforced polymer (GFRP) reinforcement embedded in fibre-blended UHPC is sparse and only focuses on regularly ribbed bars (Hossain et al. 2011, Yoo et al. 2015, Yoo and Yoon 2017) whereas fibre-reinforced polymer reinforcement surfaces significantly differ in geometry, as shown in Fig. 1.
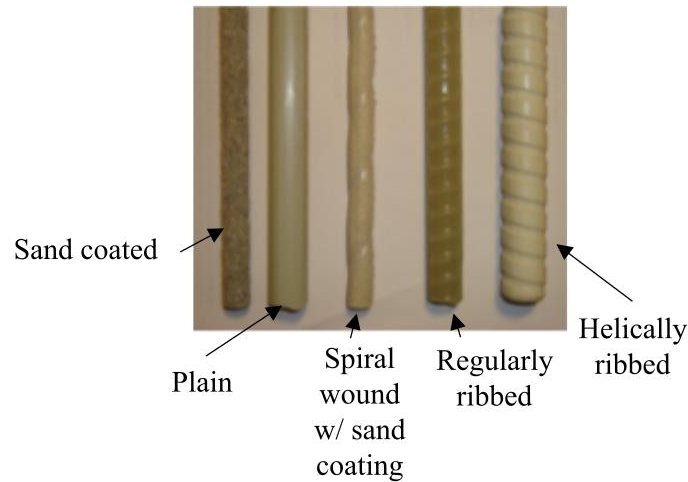

Fig. 1. Differing surface textures of GFRP reinforcing bars (Quayyum 2010).

The most commonly available forms of GFRP reinforcement are plain (smooth), sand coated, spiral wound (typically outer spiral sand coated), regularly ribbed, and helically ribbed. Previous studies performed on bond strengths for fibre-reinforced polymer (FRP) bars (Wambeke and Shield 2006, Mosley et al. 2008) concluded variation in surface treatment had no effect when embedded in regular concrete. However, this was disproved in subsequent studies (Baena et al. 2009) and determined surface texture is significant in the bond behaviour between FRP and concrete. Helically ribbed bars are one such surface type and are advantageous in providing large design life-cycles (100 years), high surface durability, and low environmental impact (MateenBar 2021). Current literature on helically ribbed FRP is very minimal, and critically, recent studies on helically ribbed GFRP bars have only investigated the bond-slip characteristics when embedded in regular concrete (Solyom and Balázs 2020,

Solyom and Balázs 2021) and none on its embedment within fibre-blended UHPC. The above has emphasised the need for an investigation on the bond-slip behaviour of helically ribbed GFRP embedded in fibre-blended UHPC. To address the above, this study aims to:

(1)   Study the variation of cover condition on the bond – slip relationship of helically ribbed GFRP and similarly ribbed steel reinforcing bars embedded in fibre-blended UHPC,

(2)   Utilise analytical models in existing literature to develop a multi-variable model calibrated from the experimental data to predict the bond-slip response of helically ribbed GFRP embedded in fibre-blended UHPC, and

(3)   Perform a parametric study on the multi-variable model to observe the effects of bar diameter and compressive strength of concrete on the bond-slip behaviour.

To realise the above objectives, a total of fourteen GFRP and steel reinforcing bars embedded in a UHPC block with varying cover conditions were cast and subjected to pull-out tests. The local bond-slip relationship for the GFRP and steel were experimentally evaluated and theoretical models for both reinforcement types were suggested and compared to established models. This study was concurrent to unpublished research at the University of Adelaide (Mahdi et al. 2021) where the implementation of low-ribbed GFRP and steel reinforcement at low clear cover was used in the experimental study of composite fibre-blended UHPC panels.

EXPERIMENTAL PROGRAM

Materials

UHPC

Established at the University of Adelaide (Mahdi et al. 2021), a UHPC mix design was used for the current study and mix proportions for a targeted density of 2,550 kg/m^3 are shown in Table 1.

Materials	Sulfate Resistant Cement	Silica Fume	Sand	Water	High-Range Water Reducer	Steel Fibre	Water-to-binder ratio (*w/b*)
Proportions (kg)	953	253	953	172	43	176	0.147

Table 1. Mix proportions of materials used in UHPC mix for current study.

Locally sourced sulphate-resistant cement with a manufacturer reported average compressive strength of 60 MPa and fine silica fume were used as binding agents to create a mix of high packing density and low permeability. Sieved river-washed sand was added to the dry mix acting as a fine aggregate before the ingredients were mixed thoroughly in a planetary cement mixer for five minutes. After the dry mixture was made homogenous, water and a high-range water reducer (HRWR) (Sika ViscoCrete 10) were added to the mixture and allowed to combine for ten minutes before discontinuous high-strength steel micro-fibres were added and combined for an additional 15 minutes. The discontinuous steel fibres were of a nominal length of 13 mm and diameter 0.2 mm with manufacturer reported average Young's modulus and ultimate strength of 210 GPa and 2850 MPa, respectively. Future reference to UHPC in the

current study will refer to the micro-fibre blended UHPC mix. The micro steel fibres constituted 2.5% of the total mix volume and are shown in Fig. 2.

Fig. 2. Micro steel fibres used in the UHPC for the current study.

To establish the compressive strength (f'_c) and Young's modulus (E_c) of the UHPC mix, nine cylinders of 100 mm diameter and 200 mm height were cast, cured and tested in accordance with AS 1012.9:2014 (Standards Australia 2014). The average 28-day compressive strength was found to be 111 MPa with a standard deviation of 6 MPa and coefficient of variation of 0.058. Additionally, eighteen specimens were cast and tested to measure the compressive strength at 7, 14, 21, 28, 32 and 50 days to produce a maturity curve for the UHPC mix shown in Fig. 3. The maturity curve underlines a relatively lower compressive strength within the first 28 days before increasing substantially afterwards. The cement largely (50-70%) consists of ground granulated blast furnace slag (GGBFS) and typically results in delayed onset of strength due to insufficient alkalinity and cement paste hydration (Soutsos et al. 2016, Korde et al. 2019). The regression model for the maturity relationship used a 4-parameter logistic curve, providing a root mean square (RMS) of 103 MPa and underlining a high goodness with a R2 value of 0.992. The average stress-strain relationship of the UHPC in compression is shown in Fig. 4.
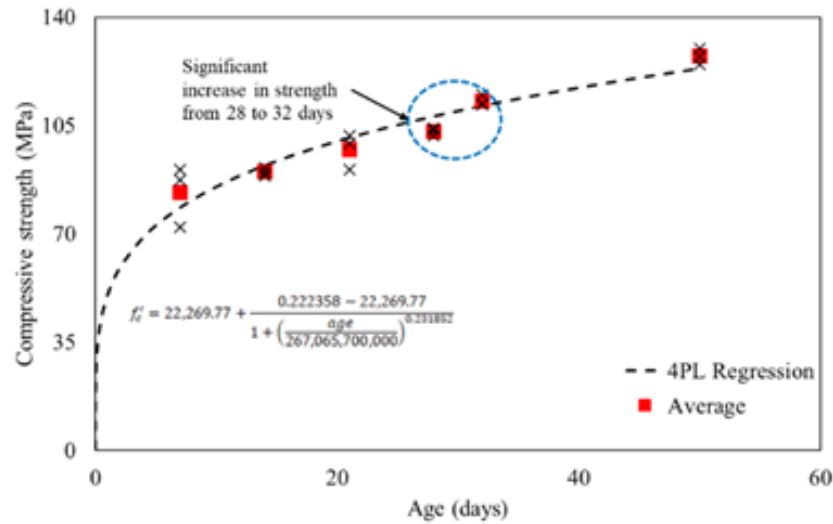
$$f_c' = 22,269.77 + \frac{0.222358 - 22,269.77}{1 + \left(\frac{age}{267,065,700,000}\right)^{0.231882}}$$

Fig. 3. Maturity curve for UHPC mix design (Mahdi et al. 2021).
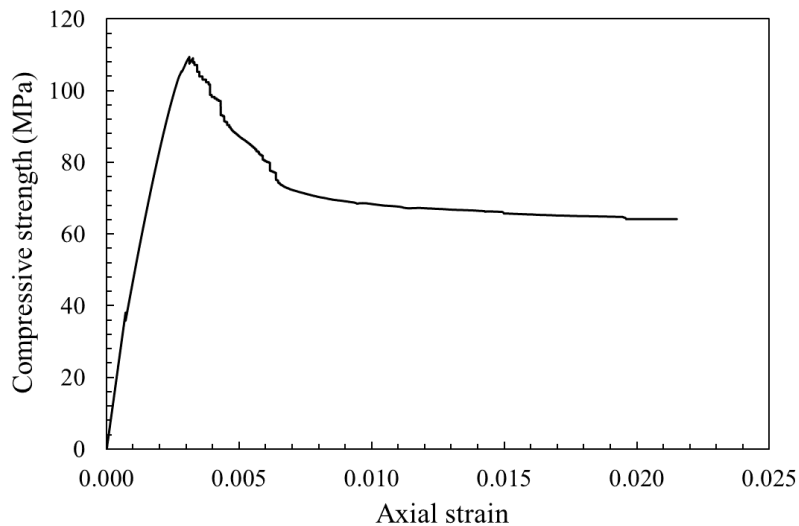

Fig. 4. Stress-strain relationship of UHPC in compression (Mahdi et al. 2021).

The tensile behaviour of UHPC was obtained by the uniaxial testing of nine dog-bone specimens (Figs. 5 (a) – (c)). The specimens include a shanked portion of 120 mm × 120 mm cross-section and 325 mm length. The ends are tapered to produce square ends of 208.6 mm × 208.6 mm and specimen length of 604.8 mm (Fig. 5 (a)). The dimensions are developed by Singh et al. (2017) and are alterations to specimens devised by Redaelli (2006) and Moreno et al. (2012). The specimens were tested under displacement control at a rate of 0.01 mm/s to a displacement of 2.5 mm before ramping to a rate of 0.05 mm/s up to failure (typically below

109

10 mm). Four linear variable displacement transducers (LVDT) were attached to sliding rods bonded to the specimen to measure the displacement and variation across the displacement length. Specimens were positioned in a specifically designed test rig (Figs. 5 (b) and (c)) to avoid stress concentrations at the bulbed ends and ensure failure within the shank. The curved surfaces of the bulbed ends were coated in gypsum paste to satisfy even contact between test jaws and specimen during the loading procedure. The average uniaxial tensile strength (f'_t) was calculated as 4 MPa with a standard deviation of 0.3 MPa and coefficient of variation of 0.123. The average tensile stress-strain relationship in addition to the load-deformation and stress-crack width relationships of the UHPC are shown in Figs. 6 (a) – (c).
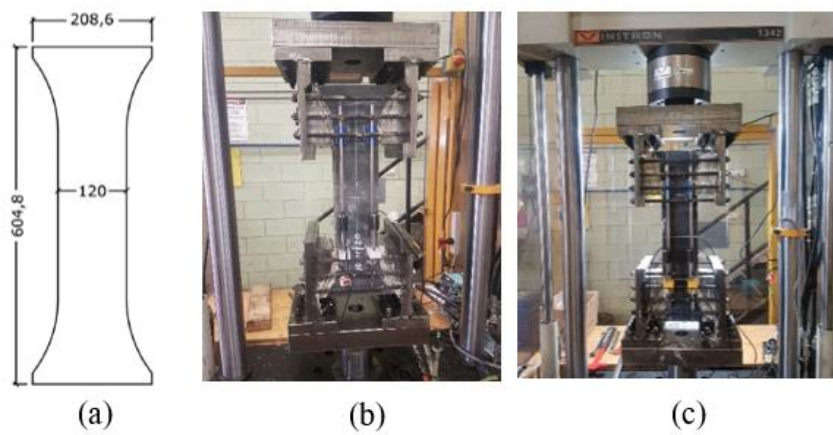

Fig. 5. Direct tension test: a) dog-bone specimen dimensions (Singh et al. 2017) (dimensions in mm); b) and c) direct tension test setup.
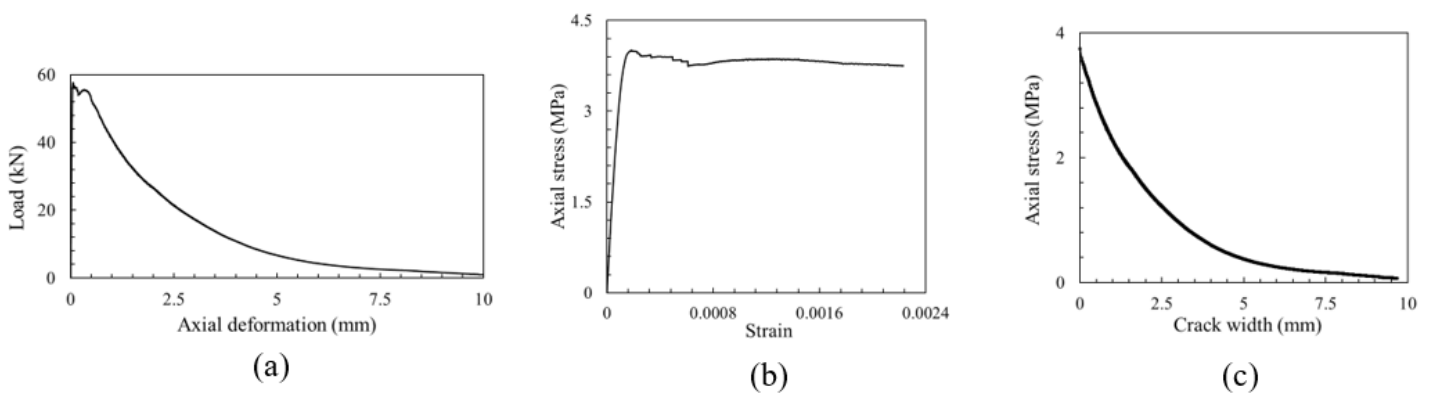

Fig. 6. Tensile properties of UHPC: a) load-deformation relationship; b) stress-strain relationship; and c) stress-crack width relationship (Mahdi et al. 2021).

Strains were estimated by taking an average of the four LVDT measurements and dividing them over the specimen shank length. Crack widths were evaluated by using the following equation:

$$s_{cr} = \frac{PL_{dg}}{E_c A_{dg}} - \Delta_{total} \qquad (1)$$

where s_{cr} is the specimen crack width, L_{dg} and A_{dg} are the specimen shank length and cross-sectional area, and Δ_{total} is the total specimen deformation. The total deformation of the dog-bone specimen was assumed to be a sum of the elastic and inelastic deformations and the inelastic deformations were equivalent to the crack widths. This assumption is supported in recent studies on crack width and tensile strain variation of UHPC in tension (Visintin et al. 2018).

GFRP reinforcement

The GFRP used in this study was a low-ribbed reinforcement developed by MateenBar™, being used as a substitute to traditional reinforcement in several recent large-scale infrastructure projects. Moreover, the low rib height was desirable for low-thickness concrete layers in multi-layered composite panels. The bars were of a nominal diameter 8 mm with a rib height of 0.175 mm, rib inclination of 57° and rib width of 5.1 mm and spacing of 10.76 mm. The cross-section of the GFRP bar and rib dimensions are shown in Figs. 7 (a) and (b) respectively.
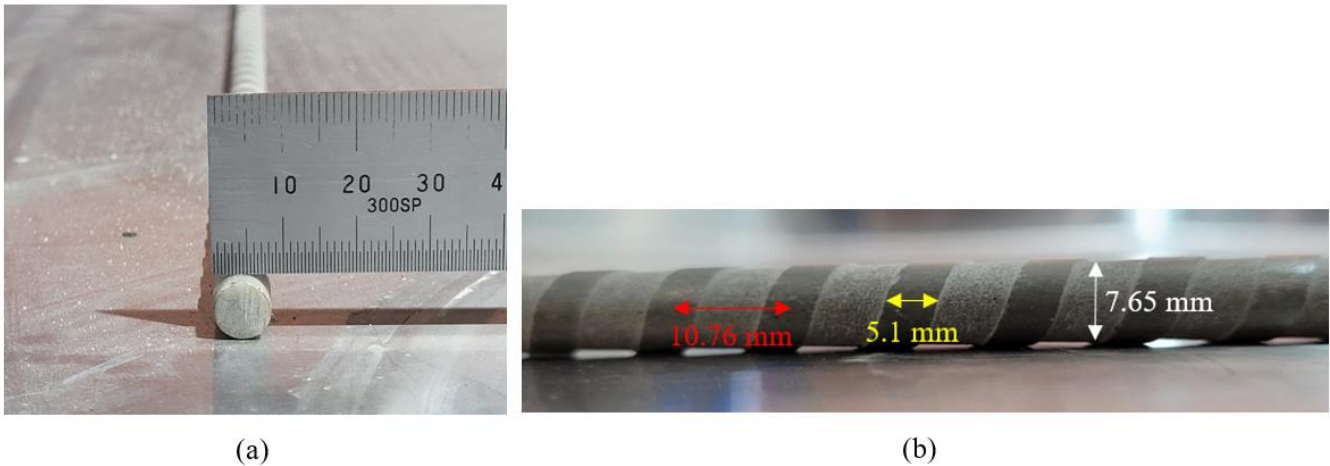
(a)   (b)

Fig. 7. GFRP bars used in the current study: a) cross-section; and b) rib dimensions.

Uniaxial tensile tests in accordance with ASTM D7205/D7205M:2006 (ASTM International 2006) were conducted on seven specimens of 1000 mm length to establish the stress-strain relationship and quantify the ultimate strength of the reinforcing bars. Steel tubes of 300 mm length, 35 mm outer diameter and 5 mm wall thickness were bonded to the bar ends to act as grip end anchors. The tubes were bonded to the reinforcing bars with two-part epoxy resin and allowed to cure for 24 hours before testing. The average ultimate strength (f_{ult}) of the GFRP was determined to be 932 MPa with a standard deviation of 104 MPa and coefficient of variation of 0.111. The nominal diameter of the GFRP specimens (8 mm) was taken to calculate the average tensile stress and plotted against the tensile strain, as shown in shown in Fig. 8.
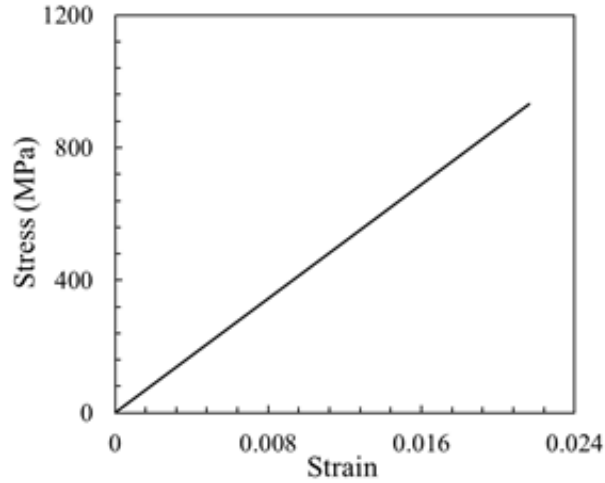
Fig. 8. Stress-strain relationship of GFRP reinforcement (Mahdi et al. 2021).

Steel reinforcement

The deformed steel reinforcing bars were selected as reference specimens for the study and were selected on similar reinforcing rib heights to the GFRP specimens. The bars were of a nominal diameter 8 mm with a rib height of 0.25 mm, rib width of 3.68 mm, rib inclination of 42° and spacing of 2.4 mm as shown in Fig. 9.

Fig. 9. Deformed steel bars used in the current study.

Uniaxial tensile tests in accordance with AS 1391:2007 (Standards Australia 2007) were performed on seven specimens of 300 mm length to establish the stress-strain relationship and quantify the yield and ultimate strengths of the reinforcing bars. The average yield strength (f_y) of the steel reinforcement was determined to be 412 MPa with a standard deviation of 6 MPa

113

and coefficient of variation of 0.014, and an average ultimate strength (f_{ult}) of 508 MPa with a standard deviation of 9 MPa and coefficient of variation of 0.018. The average stress-strain relationship of the steel reinforcement is shown in Fig. 10.
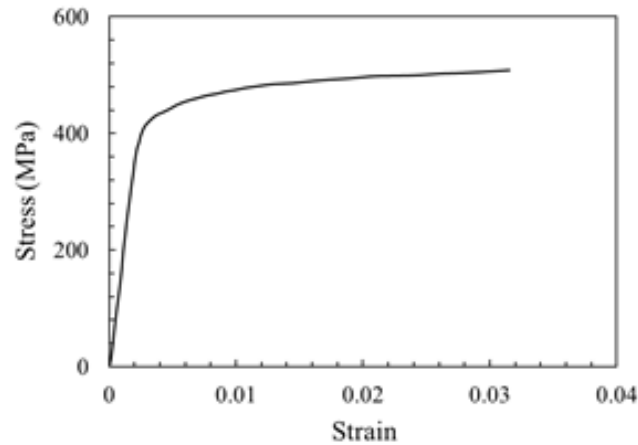

Fig. 10. Stress-strain relationship of steel reinforcement.

Pull-out Block Design and Test Instrumentation

Reinforcing bar specimens were cast into a UHPC block of 792 mm length, 160 mm depth and 100 mm thickness. The block was embedded with fourteen reinforcing bars, seven of which were GFRP and the remaining seven were steel. Dimensions of the UHPC block and test set-up are illustrated in Figs. 11 (a) – (d). A bonded length of twice the nominal diameter ($2d_b =$ 16 mm) was selected based on previous studies on bond lengths for reinforcement in UHPC in preventing bar rupture or yield (Yoo et al. 2014) as opposed to the RILEM (1994) recommendation of $5d_b$ and is illustrated in Fig. 11 (a). To replicate various clear cover conditions, reinforcement was cast in regions of the block corners, edges, centres, and in proximity to other specimens, at diameter-length increments (Fig. 11 (b)). To measure the slip of the reinforcing bars, a single 25 mm LVDT was placed at the loaded end and two 25 mm LVDT's at the free end (Fig. 11 (d)).
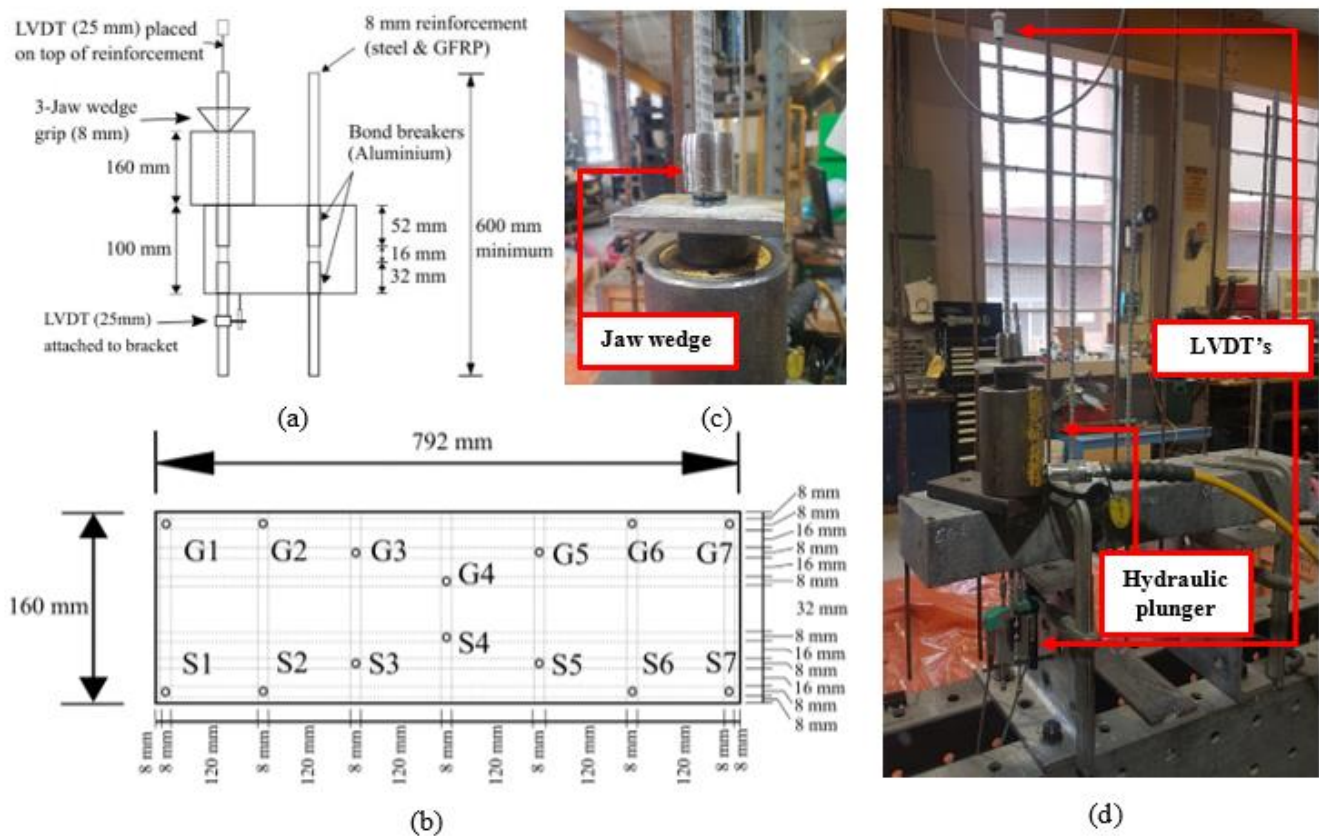
114

Fig. 11. UHPC pull-out block design: a) elevation view; b) plan view; c) cylinder with plate and wedge; and d) pull-out test set-up.

Reinforcement specimens were tested by a hollow hydraulic cylinder plunger loaded by a jack. A perforated steel plate of 10 mm thickness was placed through the reinforcing bar and a 3-jaw wedge was impacted in place above the plate to provide resistance for the loaded plunger. Regular pull-out tests employ the use of couplers to provide this resistance, however the delicate exterior surface of the GFRP required a high-friction mechanism to grip on to and apply load (Fig. 11 (c)). Two plywood boxes were constructed for the formwork of the UHPC pull-out block, with one acting as the mould and another to prevent bar camber during the

concrete pour (Fig. 12 (a)). Copper and aluminium sleeves (Fig. 12 (b)) were used as bond-breakers and were secured in place with plasticine to maintain the bonded length of 16 mm.
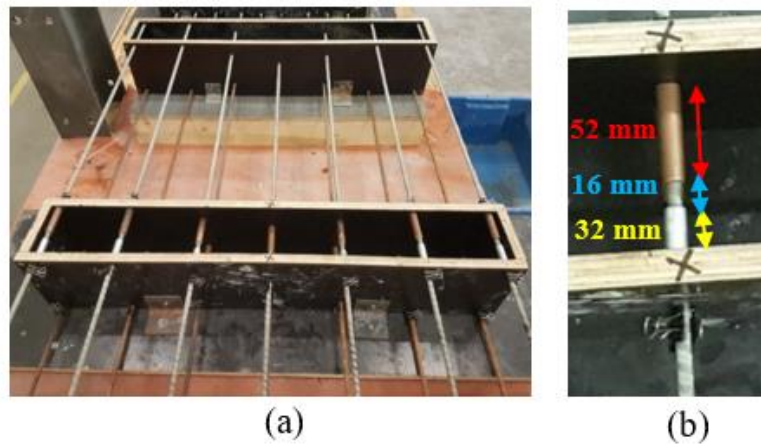

(a)   (b)

Fig. 12. Formwork for the pull-out block; (a) slanted view, and b) copper and aluminium sleeves used as bond-breaker mechanism.

EXPERIMENTAL RESULTS AND DISCUSSION

Bond Stress-Slip Response

The effect of reinforcement type and cover condition is investigated by the bond stress-slip response assessed for each of the reinforcement specimens. For simplification, bond stresses are averaged over the embedment length and defined as:

$$\tau_{ave} = \frac{P_{pull-out}}{L_{embed}\pi d_b} \tag{2}$$

where τ_{ave} is the average bond stress, $P_{pull-out}$ is the pull-out load, l_{embed} is the length of embedment of the reinforcing bar with UHPC, and d_b the nominal diameter of the reinforcing bar (8 mm). Experimental results obtained from the pull-out tests are summarised in Table 2.

Specimen	Position	Material	Peak load, P_{max} (kN)	Peak bond stress, τ_{max} (MPa)	Free end slip at peak load, s_m (mm)	Normalised bond stress, τ^* (MPa)
S1-D8-C1	Corner	Steel	4.73	11.8	1.44	1.12
S2-D8-E1	Edge	Steel	6.46	16.1	1.75 / 1.80	1.53
S3-D8-N1	Central	Steel	1.73	4.3	1.84 / 2.06	0.41
S4-D8-P1	Proximity	Steel	4.81	12.0	2.25	1.14
S5-D8-N2	Central	Steel	3.75	9.3	2.87 / 2.87	0.89
S6-D8-E2	Edge	Steel	6.02	15.0	4.13 / 4.16	1.42
S7-D8-C2	Corner	Steel	5.58	13.9	2.18	1.32
G1-D8-C1	Corner	GFRP	5.09	12.7	0.47	1.20
G2-D8-E1	Edge	GFRP	4.13	10.3	0.55 / 0.42	0.98
G3-D8-N1	Central	GFRP	5.64	14.0	2.60	1.33
G4-D8-P1	Proximity	GFRP	5.69	14.2	1.28	0.54
G5-D8-N2	Central	GFRP	5.73	14.3	2.67	1.35
G6-D8-E2	Edge	GFRP	6.37	15.9	3.51 / 3.39	1.51
G7-D8-C2	Corner	GFRP	3.05	7.6	1.93	0.72

Table 2. Summary of pull-out test results for GFRP and steel reinforcement embedded in UHPC.

In Table 2, P_{max} refers to the peak load of the pull-out test, τ_{max} is the associated bond stress determined using Eq. (2), and s_m is the free end slip at the peak load. Additionally, the normalised bond stress ($\tau^{\char`\^}$) was calculated by:

$$\tau^{\wedge} = \frac{\tau_{max}}{\sqrt{f_c'}} \qquad\qquad (3)$$

Steel reinforcement

Results for the bond stress-slip responses of steel reinforcement embedded in UHPC are shown
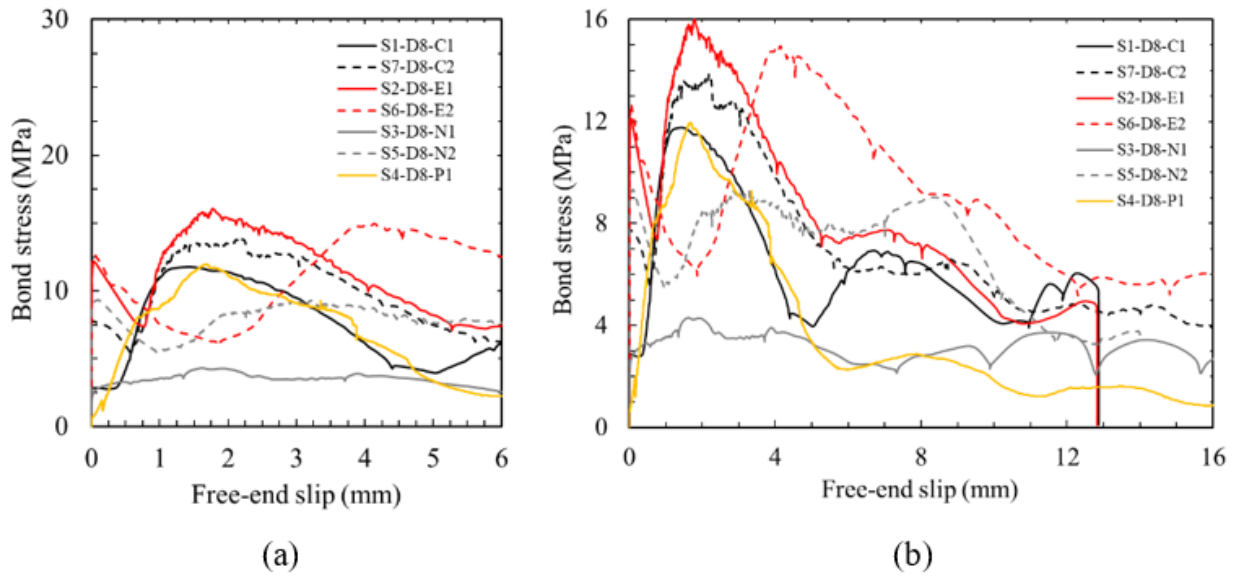
in Figs. 13 (a) and (b).

Fig. 13. Bond stress – slip responses for steel reinforcing bar embedded in UHPC; (a) peak

capture, and b) full response.

The bond stress-slip relationships for steel specimens were described by a rapid increase in

stress at zero slip before a sudden dissipation, owing to an initial break in bond between the

bar and surrounding concrete. Bond stresses then increased for a moderate increase in slip to

its peak stress, before softening and ultimately failing due to complete pull-out. The high bond

stress – zero slip is attributed to the chemical adhesion between the reinforcement and

surrounding concrete (Xiong et al. 2021). All but two specimens (S3-D8-N1 and S4-D8-P1)

experienced regular chemical adhesion, and the lack of high bond stress can be attributed to

their embedment conditions at casting. An observation made was the significant reduction in bond stress once chemical adhesion dissipated for a relatively large slip before reaching the peak stress and being frequently larger than the adhesion stress. This is owing to the contribution of the mechanical interlock between UHPC, amounting to 90% of the peak bond stress (Khaksefidi et al. 2021). As the pull-out load increased, the slip increased and became visible and resulted in the shearing and crushing of the surrounding concrete in the bonded region. Noticeably, widths of the peak stress varied with larger bond stress plateaus observed for larger cover confinement owing to its cover conditions impacted by the presence of a nearby reinforcing bar, and this is supported by observations made by Sturm and Visintin (2019) on cover confinement effects on steel reinforcement embedded in UHPC. The post-peak behaviour of specimens varied however, with specimens S1-D8-C1 and S2-D8-E1 experiencing softening before experiencing full loss in bond stress whereas specimens S3-D8-N1, S5-D8-N2 and S6-D8-E2 sustained a lower bound post-peak bond stress, owing to the fibres in the concrete matrix providing frictional resistance by gripping into the surface ribs as the bars were pulled. However, no yielding or rupture was observed and all specimens experienced failure due to debonding with specimen ribs remaining intact.

GFRP reinforcement

Results for the bond stress-slip responses of helically ribbed GFRP reinforcement embedded in UHPC are shown in Figs. 14 (a) and (b).
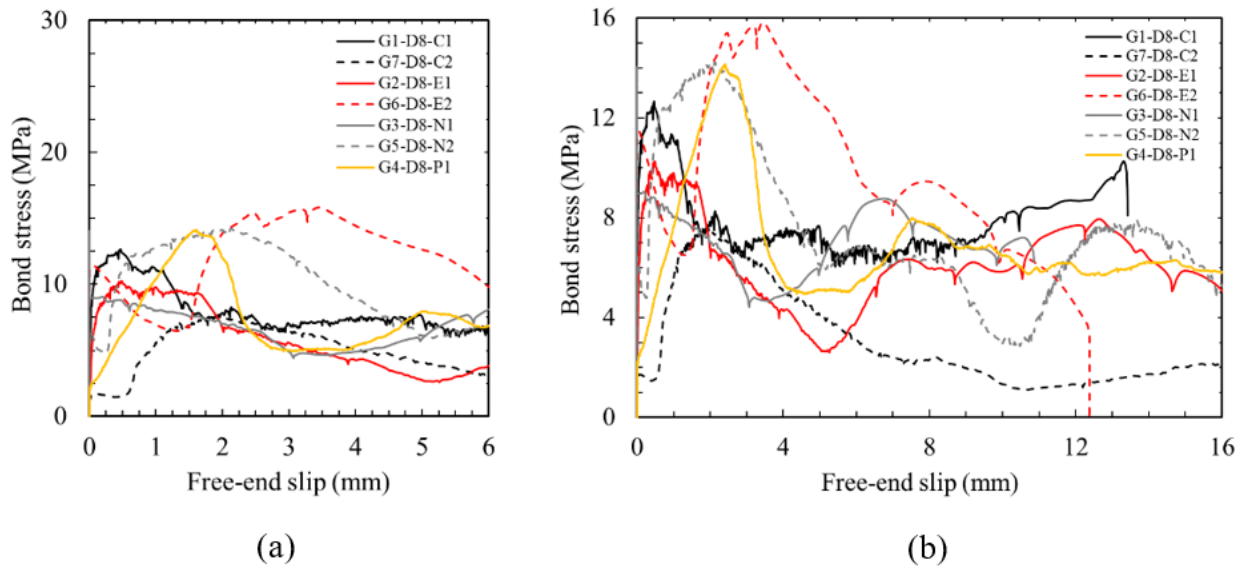
Fig. 14. Bond stress – slip responses for GFRP reinforcing bar embedded in UHPC; (a) peak capture, and b) full response.

The bond stress – slip responses for helically ribbed GFRP specimens significantly differed to that of the steel reinforcement specimens. The response was defined by a chemical adhesion stage where a rapid increase in bond stress was achieved for zero slip. However, the sudden bond stress loss observed for the steel specimens was significantly minimised with only specimen G6-D8-E2 experiencing bond stress loss before reaching its peak. Moreover, remaining specimens experienced a plateau in bond stress for increasing slip, and for specimens G2-D8-E1 and G1-D8-C1, an increase in bond strength beyond the post-peak region. This bond stress increase is the result of a similar resistance mechanism observed in the steel specimen and is referred to as the wedging effect. This effect becomes more prominent for intact ribbing as it passes through the bonded region (Achillides and Pilakoutas 2004) and is supported by studies on GFRP reinforcement embedded in regular fibre-reinforced concrete (FRC) with 1% fibre volume, which found an increase in bond strength well beyond the attainment of peak stress and in the softening region (Kim et al. 2013). As indicated from studies on ribbed GFRP

120

reinforcement embedded in UHPC by Yoo et al. (2015), the initially observed maximum bond stress, the peak stress in this instance, is recognised as the failure point and pull-out as the mode of failure in this study and is reinforced by the findings of Achillides and Pilakoutas (2004). However, it was noted that no rupture was observed and that all specimens experienced failure due to debonding with specimen ribs remaining intact. This is contrary to similar studies on GFRP reinforcement embedded in UHPC where delamination and crushing of the reinforcement ribs are observed. The absence of damage is a result of the comparably low rib depth for the helically ribbed GFRP bars. Similar to observations made for steel reinforcement, widths of the peak stresses varied for varying cover confinement conditions and is supported by the observations made by Sturm and Visintin (2019).

Analytical Modelling of Bond-Slip Behaviour

Current and proposed bond stress – slip models

Pull-out test results from previous studies along with results of the current study to propose a bond stress-slip model for helically ribbed steel bars embedded in UHPC. The proposed model is a combination of concepts derived from the bond stress-slip models proposed by Yoo and Yoon (2017) and Harajli et al. (2002). Both bond-slip models are shown in Figs. 15 (a) and (b).
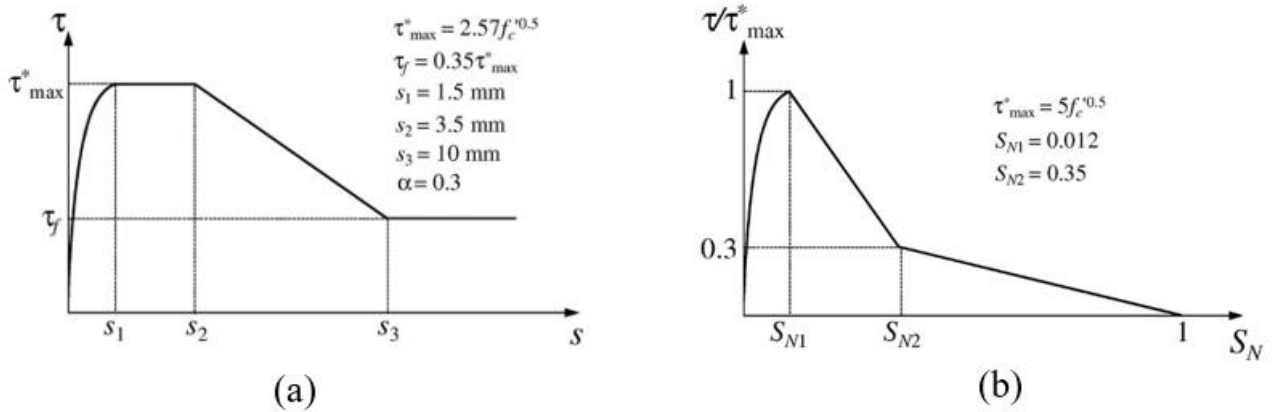
Fig. 15. Bond stress – slip models; (a) Harajli et al. (2002), and b) Yoo and Yoon (2017).

The CEB-FIP (1993) bond-slip model modified by Harajli et al. (2002) is specific to FRC and is defined in the bond stress – slip space as:

$$\tau = \tau_{max}^* \left(\frac{s}{s_1}\right)^\alpha \quad 0 \leq s \leq s_1 \tag{4}$$

$$\tau = \tau_{max}^* \quad s_1 \leq s \leq s_2 \tag{5}$$

$$\tau = \tau_{max}^* - \left(\tau_{max}^* - \tau_f\right)\frac{s-s_2}{s_3-s_2} \quad s_2 \leq s \leq s_3 \tag{6}$$

$$\tau = \tau_f \quad s > s_3 \tag{7}$$

where τ_{max}^* is the maximum bond stress, α is the ascending branch steepness coefficient, τ_f is the frictional bond stress, and slips s_1, s_2 and s_3 define the ascending branch, peak plateau, and descending branch points and are shown in Fig. 15 (a). However, outcomes from Yoo and Yoon (2017) were that the model significantly underestimated peak bond strengths and predicted significantly different bond stress-slip responses as the model was solely based on regression analysis on regular discontinuous fibre-reinforced concrete. Yoo and Yoon (2017) improved upon the previous model by developing a standardised approach using dimensionless parameters S_N and τ/τ^*_{max}, where τ^*_{max} is defined as $5f'^{0.5}_c$ and S_N as a normalisation of the slips (s/l_{embed}). The model is defined as:

122

$$\tau = \tau_{max}^{*}\left(1 - e^{-S_N/s_r}\right)^{\beta} \quad 0 \leq S_N \leq S_{N1} \tag{8}$$

$$\tau = \tau_{max}^{*}\left(1 - 0.7\frac{S_N - S_{N1}}{S_{N2} - S_{N1}}\right) \quad S_{N1} \leq S_N \leq S_{N2} \tag{9}$$

$$\tau = 0.3\tau_{max}^{*}\left(\frac{1 - S_N}{1 - S_{N2}}\right) \quad S_{N2} \leq S_N \leq 1 \tag{10}$$

where s_r and β are test data regression coefficients, s is the free-end slip, and dimensionless slip parameters S_{N1} and S_{N2} define the ascending and softening branch points. The model and the parameters are determined by a least-squares regression using normalised test data and are shown in Fig. 15 (b). The model is successful in modelling the bond-slip behaviour GFRP embedded in UHPC, however it does not account for the peak plateau present when increasing the cover confinement area and was calibrated based on high ridged ribbed reinforcement whereas the current study uses shallow helical ribbing, and thus exhibiting vastly different bond-slip responses. Furthermore, the results of the current study produced dimensionless peak stresses much less than the normalised value in the τ/τ_{max}^{*} - S_N space.

The studies' proposed model aimed to bridge the problem by utilising the descending branch used by Yoo and Yoon (2017) to predict complete pull-out after the softening branch while incorporating a peak stress plateau after the ascending branch implemented by CEB-FIP (1993) and Haragli et al. (2002). The proposed model is shown in Fig. 16.
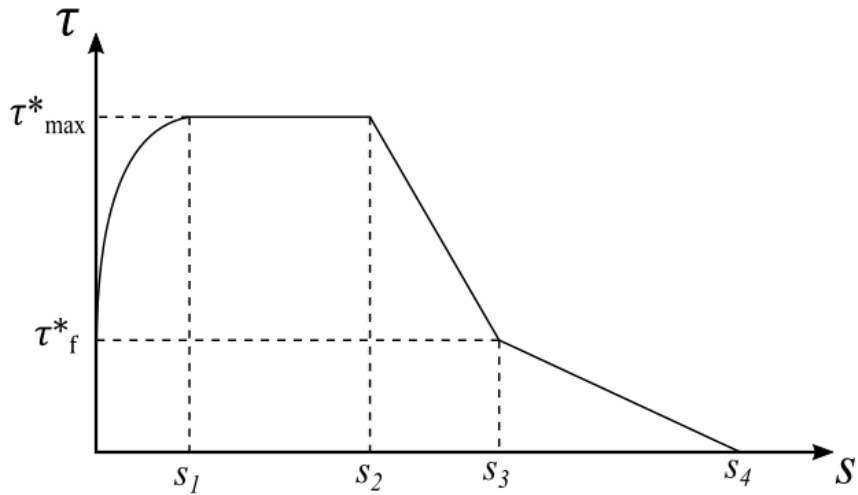
Fig. 16. The bond stress – slip model proposed in the current study.

A major objective of the proposed model was to allow peak bond stress, failure point, and slip parameters be a function of the reinforcement cover conditions. This was achieved by assuming a bond stress dissipation zone with prism dimensions $2d_b$ clear distance from the reinforcement edges and is illustrated in Fig. 17.
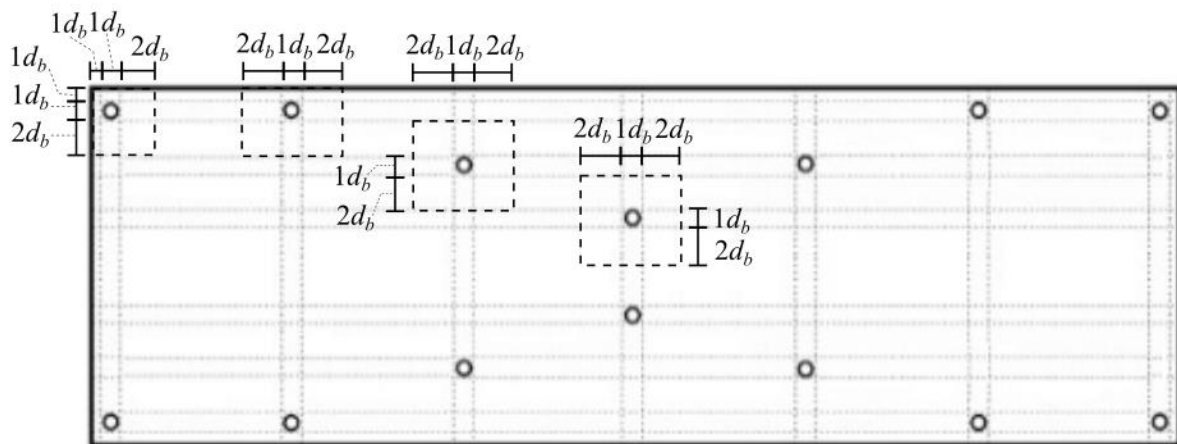

Fig. 17. Reinforcement prism dimensions for corner, edge, and central cover conditions.

The prisms dimensions of the three reinforcement positions are influenced by the cover conditions and affect the prism area, A_{prism}. The prism areas of the corner, edge and central prisms are $16d_b^2$, $20d_b^2$, and $25d_b^2$. Firstly, the normalised peak bond stress $\tau^*_{max}/f'^{0.5}_c$ for the pull-out data was plotted against A_{prism}/d_b^2 and is shown in Fig. 18.
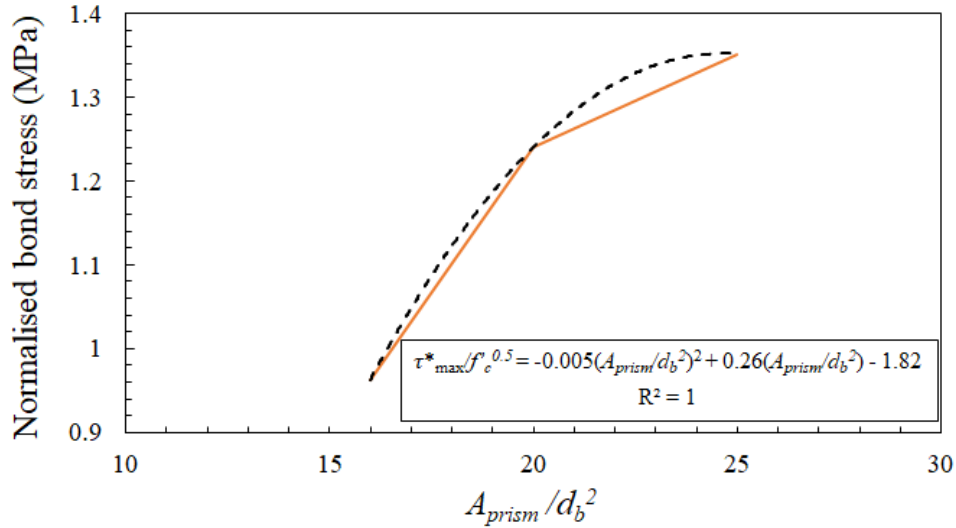

Fig. 18. Peak normalised bond stress vs. A_{prism}/d_b^2.

The peak bond stresses from the pull-out data were fitted to A_{prism}/d_b^2 through a 2-point regression which displayed excellent goodness of fit. The model was limited to an area ratio (A_{prism}/d_b^2) of 25 which resulted in:

$$\tau^*_{max} = f'^{0.5}_c \left[-0.005 \left(\frac{A_{prism}}{d_b^2} \right)^2 + 0.26 \left(\frac{A_{prism}}{d_b^2} \right) - 1.82 \right], \qquad \frac{A_{prism}}{d_b^2} \leq 25 \quad (11)$$

By using a normalised bond stress relationship, the bond stress can be a direct function of the prism to embedment length ratio as opposed to a fixed concrete strength, and thus, can be used for the proposed bond stress. Noticeably, the peak normalised bond stresses are significantly lower for less confined areas such as a corner placement. The failure bond stress, τ^*_f, was similarly modelled using an exponential regression model as shown in Fig. 19.
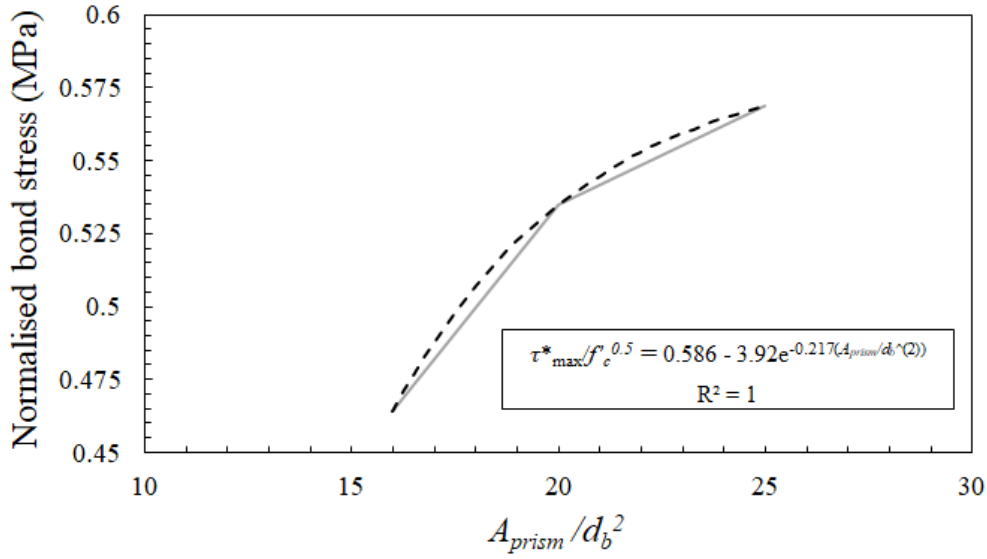
125

Fig. 19. Normalised failure bond stress vs. A_{prism}/d_b^2.

The failure bond stresses for the various cover conditions were fitted with an exponential model and showed excellent goodness of fit. The failure bond stress expectedly increased for increasing confinement and was expressed as:

$$\tau_f^* = f'^{0.5}_c \left[0.586 - 3.92e^{-0.217\left(\frac{A_{prism}}{d_b^2}\right)}\right], \quad \frac{A_{prism}}{d_b^2} \leq 25 \qquad (12)$$

The slip parameters s_1, s_2, and s_3, were also modelled based on the pull-out results of the current study, whereas s_4 was set to the embedment length, l_{embed} to emulate complete pull-out behaviour of the reinforcement from the embedment zone and permitted the slip parameters to be normalised to the embedment length. This relationship is shown in Fig. 20.
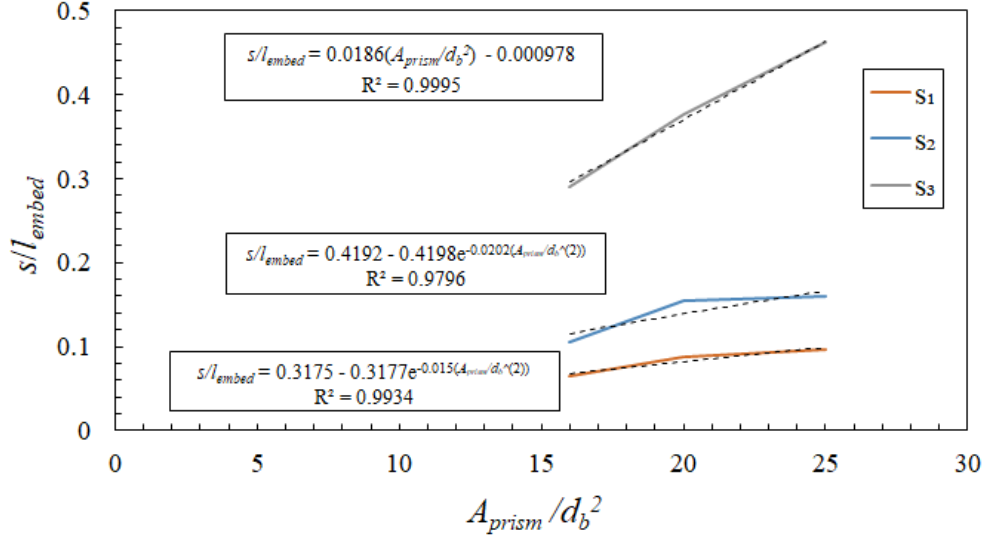
126

Fig. 20. Normalised slip vs. A_{prism}/d_b^2.

The slip parameters were fitted with linear and exponential models and showed excellent goodness of fit. Intuitively, the slip values increase for an increasing confining cover. The slip parameters are defined as:

$$s_1 = l_{embed}\left[0.3175 - 0.3177e^{-0.015\left(\frac{A_{prism}}{d_b^2}\right)}\right], \quad \frac{A_{prism}}{d_b^2} \leq 25 \tag{13}$$

$$s_2 = l_{embed}\left[0.4192 - 0.4198e^{-0.0202\left(\frac{A_{prism}}{d_b^2}\right)}\right], \quad \frac{A_{prism}}{d_b^2} \leq 25 \tag{14}$$

$$s_3 = l_{embed}\left[0.0186\left(\frac{A_{prism}}{d_b^2}\right) - 0.000978\right], \quad \frac{A_{prism}}{d_b^2} \leq 25 \tag{15}$$

$$s_4 = l_{embed}, \quad \frac{A_{prism}}{d_b^2} \leq 25 \tag{16}$$

The equations proposed in this study (Eqs. (11) – (16)) define the limits of the proposed model illustrated in Fig. (16), however the shape of the ascending branch was determined using a least-squares difference approach for the calibration of the pull-out data to the branch proposal

in Eq. (4). Based on the least-squares difference method, α was found to be 0.274. The plateau
and two softening branches are represented as:

$$\tau = \tau_{max}^* \quad s_1 \leq s \leq s_2 \tag{18}$$

$$\tau = \tau_{max}^* - \left(\tau_{max}^* - \tau_f^*\right)\frac{s-s_2}{s_3-s_2} \quad s_2 \leq s \leq s_3 \tag{19}$$

$$\tau = \tau_f^* \left(1 + \frac{s-s_3}{s_4-s_3}\right) \quad s_3 \leq s \leq s_4 \tag{20}$$

The stress parameters and functions in Eqs. (11) – (12) and (18) – (20) in conjunction with the

slip parameters in Eqs. (13) – (16) provide a complete representation of the bond slip – stress

relationship for GFRP embedded in UHPC as a function of compressive strength and cover

condition. No previous studies had studied the experimental behaviour of GFRP reinforcement

embedded in UHPC for an embedment length of $2d_b$, thus, the proposed model was compared

to the steel specimen pull-out data in the current study, as both were cast in the same prism,

encountered no yielding or splitting failure, cast with the same embedment length, and more

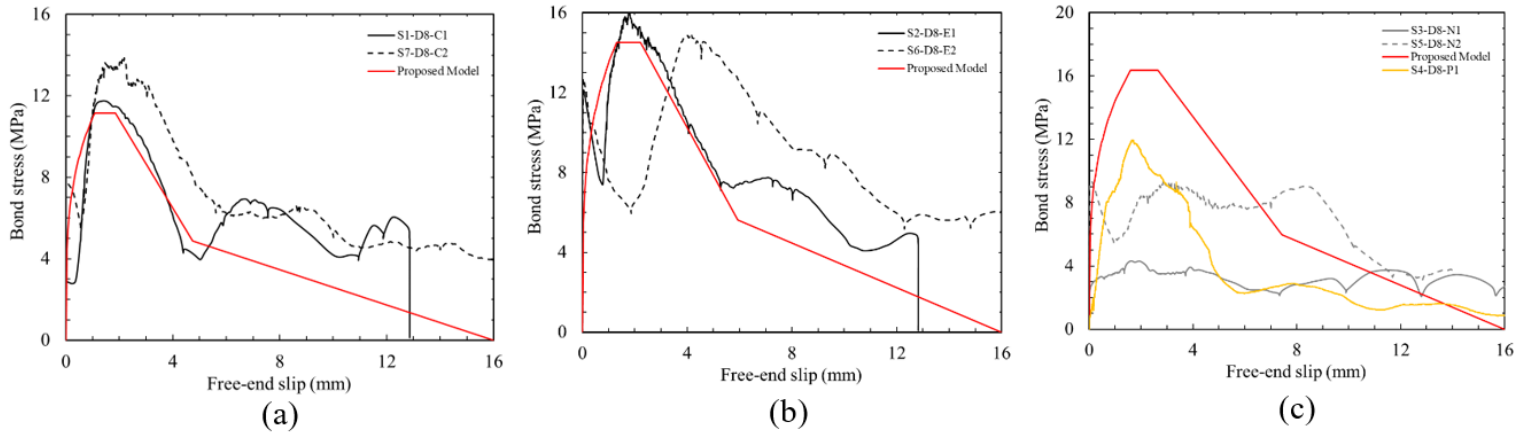significantly had a low rib depth. This correlation is illustrated in Figs. 21 (a) – (c).

Fig. 21. Bond stress – slip comparisons between steel reinforcement and proposed model for:
a) corner placement; b) edge placement; and c) central placement.

The proposed model generally correlates well to the experimental results of the steel reinforcement embedded in UHPC for the same embedment length, and this is more noticeable in Figs. 21 (a) and (b) where the maximum peak bond stresses are both close in magnitude and the slips in those locations are also in proximity to each other. Moreover, the slope of the softening and pull-out branches closely matches. However, the results do not correlate with the proposed model applied for the centrally placed reinforcement. This is due to casting and testing issues with the specimens, namely specimens S5-D8-N2 and S3-D8-N1, where an ascending branch was never attained. This suggests premature debonding before testing occurred. Ultimately, the proposed model agreed with the experimental results for a similarly ribbed reinforcement type, although further experimental study is recommended to further improve the model parameters and investigate cover conditions lower than $1d_b$.

Parametric study

A parametric study was performed on the proposed model to observe the effects of concrete compressive strength and bar diameter on the bond-stress relationship and the related parameters. The concrete compressive strength was varied for differing reinforcement confinement conditions to observe the effect on both peak and failure bond stresses and is illustrated in Figs. 22 (a) and (b).
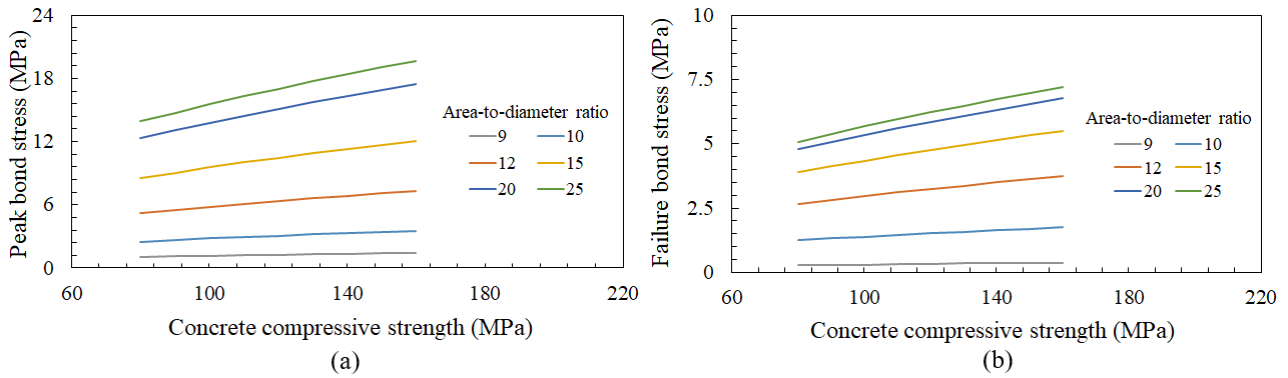
Fig. 22. Predictions for bond stress vs. concrete compressive strength for varying cover conditions by the proposed model: a) peak bond stress; and b) failure bond stress.

Predictions shown by the proposed model highlight an expected increase in both peak and failure bond stresses for an increasing compressive bond stress, and that this behaviour is magnified for larger cover confinement. This is better illustrated when observing the bond strengths for an area ratio (A_{prism}/d_b^2) of 9, the plateau suggesting that a stronger compressive strength for UHPC will have no effect on the bond strengths. Moreover, the increase in area ratio has a significant effect at the lower cover region however its efficacy is reduced as the area ratio increases. Another measure on the effect of concrete strength on the proposed model was observing the complete bond – slip behaviour for a fixed bar diameter (8 mm) and embedment length of $2d_b$ for an increasing compressive strength, shown in Fig. 23. The relationships illustrated in Fig. 23 predictively show the increase in bond strength across the relationships for an increasing compressive concrete strength. By assuming a fixed embedment length and bar diameter, the slips do not vary and results in an increase and decrease of the slope magnitudes for the failure branch and softening branch, respectively. An important parameter to examine was the bar diameter, and predictions for the bond – slip relationship for varying bar diameter was performed and is illustrated in Fig. 24.
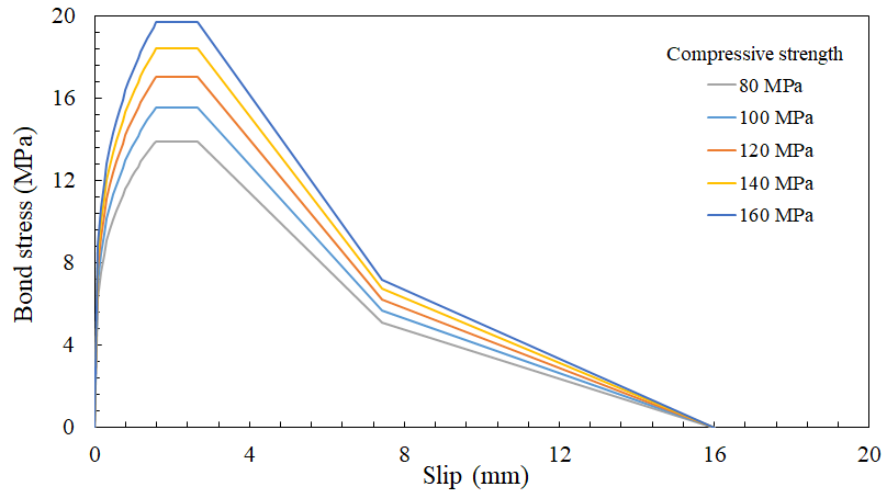
130

Fig. 23. Predictions for bond stress vs. slip for varying concrete compressive strength by the proposed model.

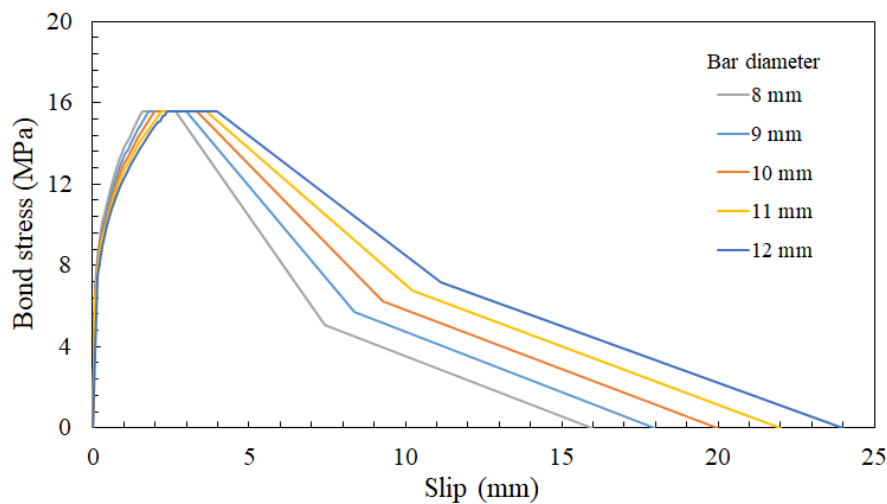**Fig. 24.** Predictions for bond stress vs. slip for varying reinforcement bar diameter by the proposed model.

The predictions made in Fig. 24 highlight both the change in slip magnitudes and peak widths for the varying bar diameters. The increasing bar diameter results in an increase in slip at both the peak, onset of softening, and onset of failure, and consequently a larger peak plateau width.

131

Moreover, the steepness of the softening phase remains the same for the varying diameter and highlights an increase in bond strength for both the softening and failure phases.

CONCLUSIONS

The objective of the present study was investigation on the bond-slip behaviour of helically ribbed GFRP embedded in UHPC. A total of fourteen GFRP and steel reinforcing bars embedded in a UHPC block with varying cover conditions were cast and subjected to uniaxial pull-out testing. The local bond-slip relationships of the GFRP and steel specimens were experimentally evaluated, and existing theoretical models were reviewed to develop a new multi-variable bond-slip model for helically ribbed GFRP embedded in UHPC. The following conclusions can be drawn from the study:

(1) The pull-out specimens displayed high variability in the bond-slip behaviour owing to the varying cover conditions. Both steel and GFRP exhibited larger peak bond stresses and peak plateau widths for centrally placed reinforcement, and both decreased for specimens placed at the corners and edges.

(2) Established bond-slip models were reviewed and used to develop a new model to predict the bond-slip behaviour of helically ribbed GFRP reinforcement embedded in UHPC for the current model. The pull-out data of the current study was used to establish expressions to the parameters presented in the proposed model, primarily to account for the effects of cover condition.

(3) The newly established model was compared to the steel reinforcement tested in the current study and was largely agreeable in the bond-slip behaviour, with peak stresses, plateau widths and both softening and failure slopes closely matching.

(4) The parametric study was performed on the proposed model to observe the effects of bar diameter and compressive strength of concrete on the bond-slip behaviour. The

major findings were the increase in bond strengths at peak and failure for an increasing concrete compressive strength, the increase in strength for the entire bond-slip relationship for an increasing concrete compressive strength, and the increase in slip magnitudes for the slip parameters for an increasing bar diameter. Moreover, there is minimal variation in peak and failure stresses for low concrete cover conditions and an increase in plateau widths for increasing bar diameters, suggesting a nil effect for increasing the compressive strength of concrete for reinforcement in low cover conditions.

Recommendations for future research are to perform a larger number of experimental tests on helically ribbed GFRP reinforcement specimens embedded in UHPC. The variation of bond – slip behaviour is largely affected by the bar diameter and concrete cover conditions, however differing rib depths, widths, and spacing have a large effect on the bond – slip behaviour and requires adjustments to the proposed model to account for. Moreover, tests for varying embedment lengths and bar diameters should be performed to better verify the outcomes of the parametric study.

DATA AVAILABILITY STATEMENT

Some or all data, models, or code that support the findings of this study are available from the corresponding author upon reasonable request; pull-out data, bond-slip fitting data.

NOTATION

The following symbols are used in this paper:

A_{dg} = cross-sectional area of tensile dog-bone specimen (mm^2);

d_b = bar diameter of GFRP and steel reinforcing bars (mm);

E_c = Young's modulus of concrete (GPa);

f_{ult} = ultimate strength of GFRP and steel (MPa);

f_y = yield strength of steel (MPa);

f'_c = compressive strength of concrete (MPa);

f'_t = tensile strength of concrete (MPa);

L_{dg} = shank length of tensile dog-bone specimen (mm);

l_{embed} = bar embedment length (mm);

P_{max} = peak applied pull-out load (kN);

$P_{pull-out}$ = applied pull-out load (kN);

R^2 = coefficient of determination;

S_N = normalised slip parameter (mm/mm);

S_{N1} = normalised slip at peak stress (mm/mm);

S_{N2} = normalised slip at softening (mm/mm);

s_{cr} = tensile crack width of tensile dog-bone specimen (mm);

s_m = slip at peak bond stress (mm);

s_r = slip regression coefficient (dimensionless);

s = reinforcement slip (mm);

s_1 = ascending branch peak slip (mm);

s_2 = peak plateau slip (mm);

s_3 = softening branch frictional slip (mm);

s_4 = failure slip (mm);

w/b = water-to-binder ratio (kg/kg);

α = ascending branch steepness parameter (dimensionless);

β = exponential regression coefficient (dimensionless);

Δ_{total} = total uniaxial deformation of tensile dog-bone specimen (mm);

τ = bond stress (MPa);

τ_{ave} = average bond stress (MPa);

τ_f = frictional bond stress in model proposed by Yoo and Yoon (2017) (MPa);

τ_{max} = peak bond stress (MPa);

$\hat{\tau}$ = normalised bond stress (MPa);

τ^*_f = frictional bond stress in model proposed by current study (MPa); and

τ^*_{max} = peak bond stress in all models (MPa).

REFERENCES

Achillides, Z., and K. Pilakoutas. 2004. "Bond behavior of fiber reinforced polymer bars under direct pullout conditions." *J. Comp. Constr.*, 8 (2): 173-181. https://doi.org/10.1061/(ASCE)1090-0268(2004)8:2(173)

ASTM International. 2006. *Standard Test Method for Tensile Properties of Fiber Reinforced Polymer Matrix Composite Bars*. West Conshohocken, PA: ASTM International.

Bae, Y., and S. Pyo. 2020. "Ultra high performance concrete (UHPC) sleeper: Structural design and performance." *Eng. Struct.*, 210, 110374. https://doi.org/10.1016/j.engstruct.2020.110374

Baena, M., L. Torres, A. Turon, and C. Barris. 2009. "Experimental study of bond behaviour between concrete and FRP bars using a pull-out test." *Comp. Pt. B: Eng.*, 40(8), 784-797. https://doi.org/10.1016/j.compositesb.2009.07.003.

CEB (Comité euro-international du béton). 1993. *CEB-FIP Model Code 90*. Lausanne, Switzerland: CEB.

Cosenza, E., G. Manfredi, and R. Realfonzo 2002. "Development length of FRP straight rebars." *Comp. Pt. B: Eng.*, 33 (7), 493-504. https://doi.org/10.1016/S1359-8368(02)00051-3.

Harajli, M., B. Hamad, and K. Karam. 2002. "Bond-slip response of reinforcing bars embedded in plain and fiber concrete." *J. Mat. Civ. Eng.*, 14 (6): 503-511. https://doi.org/10.1061/(ASCE)0899-1561(2002)14:6(503).

Hossain, K., D. Ametrano, C. Mak, and M. Lachemi. 2011. "Bond strength and development length of GFRP bars in ultra-high performance concrete." *J. Build. Eng.*, 10, 69-79. https://doi.org/10.1016/j.jobe.2017.02.005.

Jungwirth, J., and A. Muttoni. 2004. "Structural behavior of tension members in Ultra High Performance Concrete." In *International symposium on ultra high performance concrete*, 1-12. Kassel, Germany.

Khaksefidi, S., M. Ghalehnovi, and J. De Brito. 2021. "Bond behaviour of high-strength steel rebars in normal (NSC) and ultra-high performance concrete (UHPC)." *J. Build. Eng.*, 33, 101592. https://doi.org/10.1016/j.jobe.2020.101592.

Kim, B., J.-H. Doh, C.-K. Yi, and J.-Y. Lee. 2013. "Effects of structural fibers on bonding mechanism changes in interface between GFRP bar and concrete." *Comp. Pt. B: Eng.*, 45 (1), 768-779. https://doi.org/10.1016/j.compositesb.2012.09.039.

Korde, C., M. Cruickshank, R. P. West, and C. Pellegrino. 2019. "Activated slag as partial replacement of cement mortars: Effect of temperature and a novel admixture." *Constr. Build. Mat.*, 216, 506-524. https://doi.org/10.1016/j.conbuildmat.2019.04.172.

Larsen, I. L., and R. T. Thorstensen. 2020. "The influence of steel fibres on compressive and tensile strength of ultra high performance concrete: A review." *Constr. Build. Mat.*, 256, 119459. https://doi.org/10.1016/j.conbuildmat.2020.119459.

Mahdi, S., A. H. Sheikh, M. S. Mohamed Ali, and M. Elchalakani. 2021. "Experimental investigation into the structural behaviour of ultra-high performance fibre-reinforced concrete box-celled composite panels." submitted, *Comp. Struct.*, Elsevier, Amsterdam, Netherlands.

Marchand, P., F. Baby, A. Khadour, T. Battesti, P. Rivillon, M. Quiertant, H.-H. Nguyen, G. Généreux, J.-P. Deveaud, and A. Simon. 2016. "Bond behaviour of reinforcing bars in UHPFRC." *Mater. struct.*, 49 (5), 1979-1995. https://doi.org/10.1617/s11527-015-0628-0.

MateenBar. 2021. " Corrosion-free, durable, sustainable | Mateenbar." Accessed November 18, 2021. https://www.mateenbar.com/advantages.

Moreno, D., W. Trono, G. Jen, C. Ostertag, and S. Billington. 2012. "Tension-stiffening in reinforced high performance fiber-reinforced cement-based composites under direct tension.", *High Perf. Fiber Reinf. Cem. Comp. 6*, 263-270. https://doi.org/10.1007/978-94-007-2436-5_32

Mosley, C. P., A. K. Tureyen, and R. J. Frosch. 2008. "Bond strength of nonmetallic reinforcing bars." *ACI Struct. J.*, 105 (5), 634-642.

Oesterlee, C. 2010. *Structural response of reinforced UHPFRC and RC composite members*. Bern, Switzerland: Bern University of Applied Sciences.

Quayyum, S. 2010. *Bond behaviour of fibre reinforced polymer (FRP) rebars in concrete*. Vancouver, Canada: University of British Columbia.

Redaelli, D. 2006. "Testing of reinforced high performance fibre concrete members in tension." In Proc., *6th Int. Ph.D. Symp. in Civil Eng., Zurich 2006.*, 1-8. Zurich, Switzerland.

Reineck, K.H., and S. Greiner. 2004. "Tests on ultra-high performance fibre reinforced concrete designing hot-water tanks and UHPFRC-shells." In Proc., *Int. Symp.Ultra-High Perf. Conc., Kassel, Germany.*, 361-374. Kassel, Germany.

RILEM TC. 1994. *RILEM recommendations for the testing and use of Constructions Materials - RC 6 Bond test for reinforcement steel. 2. Pull-out test, 1983.*, 218-220. E & FN SPON.

Singh, M., A. Sheikh, M. M. Ali, P. Visintin, and M. Griffith. 2017. "Experimental and numerical study of the flexural behaviour of ultra-high performance fibre reinforced concrete beams." *Con. Build. Mat.*, 138, 12-25. https://doi.org/10.1016/j.conbuildmat.2017.02.002.

Solyom, S., and G. L. Balázs. 2020. "Bond of FRP bars with different surface characteristics." *Con. Build. Mat.*, 264, 119839. https://doi.org/10.1016/j.conbuildmat.2020.119839

Solyom, S., and G. L. Balázs. 2021. "Analytical and statistical study of the bond of FRP bars with different surface characteristics." *Comp. Struct.*, 270, 113953. https://doi.org/10.1016/j.conbuildmat.2020.119839

Soutsos, M., A. Hatzitheodorou, J. Kwasny, and F. Kanavaris. 2016. "Effect of in situ temperature on the early age strength development of concretes with supplementary cementitious materials." *Con. Build. Mat.*, 103, 105-116. https://doi.org/10.1016/j.conbuildmat.2015.11.034

Standards Australia. 2014. *Methods for testing concrete - Method 9: Compressive strength tests - Concrete, mortar and grout specimens*. AS 1012.9:2014. Sydney, Australia: Standards Australia.

Standards Australia. 2007. *Metallic materials—Tensile testing at ambient temperature*. AS 1391:2007. Sydney, Australia: Standards Australia.

Sturm, A. B., and P. Visintin. 2019. "Local bond slip behavior of steel reinforcing bars embedded in ultra high performance fibre reinforced concrete." *Struct. Conc.*, 20 (1), 108-122. https://doi.org/10.1002/suco.201700149.

Visintin, P., A. Sturm, M. Mohamed Ali, and D. Oehlers. 2018. "Blending macro-and micro-fibres to enhance the serviceability behaviour of UHPFRC." *Aus. J. Civ. Eng.*, 16(2), 106-121. https://doi.org/10.1080/14488353.2018.1463608.

Wambeke, B. W., and C. K. Shield. 2006. "Development length of glass fiber-reinforced polymer bars in concrete." *ACI Mat. J.*, 103 (1), 11-17.

Wiemer, N., A. Wetzel, M. Schleiting, P. Krooß, M. Vollmer, T. Niendorf, S. Böhm, and B. Middendorf. 2020. "Effect of fibre material and fibre roughness on the pullout behaviour of metallic micro fibres embedded in UHPC." *Materials*, 13 (14), 3128. https://doi.org/10.3390/ma13143128

Xiong, Z., W. Wei, F. Liu, C. Cui, L. Li, R. Zou, and Y. Zeng. 2021. "Bond behaviour of recycled aggregate concrete with basalt fibre-reinforced polymer bars." *Comp. Struct.*, 256, 113078. https://doi.org/10.1016/j.compstruct.2020.113078.

Yoo, D.-Y., K.-Y. Kwon, J.-J. Park, and Y.-S. Yoon. 2015. "Local bond-slip response of GFRP rebar in ultra-high-performance fiber-reinforced concrete." *Comp. Struct.*, 120, 53-64. https://doi.org/10.1016/j.compstruct.2014.09.055.

Yoo, D.-Y., J.-J. Park, S.-W. Kim, and Y.-S. Yoon. 2014. "Influence of reinforcing bar type on autogenous shrinkage stress and bond behavior of ultra high performance fiber reinforced concrete." *Cem. Conc. Comp.*, 48, 150-161. https://doi.org/10.1016/j.cemconcomp.2013.11.014.

Yoo, D.-Y., H.-O. Shin, J.-M. Yang, and Y.-S. Yoon. 2014. "Material and bond properties of ultra high performance fiber reinforced concrete with micro steel fibers." *Comp. Pt. B: Eng*, 58, 122-133. https://doi.org/10.1016/j.compositesb.2013.10.081.

Yoo, D.-Y., and Y.-S. Yoon. 2017. "Bond behavior of GFRP and steel bars in ultra-high-performance fiber-reinforced concrete." *Adv. Comp. Mat.* 26 (6), 493-510. https://doi.org/10.1080/09243046.2016.1197493.

THIS PAGE HAS BEEN LEFT INTENTIONALLY BLANK

CHAPTER 4

Background

In this chapter, the experimental study is performed to observe the structural behaviour of curved and asymmetrically skewed UHPFRC slabs and is accompanied by several analytical and numerical modelling procedures. Asymmetric and curved slab specimens are cast at various skew and curvature angles and tested under statically indeterminate conditions. Closed-form solutions are developed to predict deflections at the ultimate state, and a thorough finite-element analysis is performed to observe the full-range structural performance. A parametric study is performed to examine the variation of deflection, shear, bending and torsion along the slab length for varying skew and curvature angles.

List of manuscripts

Ali, M. M., Mahdi, S., Sheikh, A. H., Elchalakani, M., & Xie, T. (2021). "Structural performance and analysis of asymmetrically skewed and curved ultra-high performance fibre reinforced concrete slabs." *Engineering Structures*, 113574.

Statement of Authorship

Title of Paper	Structural Performance and Analysis of Asymmetrically Skewed and Curved Ultra-High Performance Fibre Reinforced Concrete Slabs
Publication Status	☑ Published ☐ Accepted for Publication ☐ Submitted for Publication ☐ Unpublished and Unsubmitted work written in manuscript style
Publication Details	Ali, M. M., Mahdi, S., Sheikh, A. H., Elchalakani, M., & Xie, T. (2021). "Structural performance and analysis of asymmetrically skewed and curved ultra-high performance fibre reinforced concrete slabs." *Engineering Structures*, 113574.

Principal Author

Name of Principal Author (Candidate)	Mohamed Sadakkathulla Mohamed Ali
Contribution to the Paper	Supervision, research conceptualisation, methodology formulation, and manuscript revision
Overall percentage (%)	30
Signature	Date 29/12/2021

Co-Author Contributions

Name of Co-Author	Shahin Mahdi
Contribution to the Paper	Manuscript preparation and revision, software analysis, model development and theory validation (30%)
Certification	This paper reports on original research I conducted during the period of my Higher Degree by Research candidature and is not subject to any obligations or contractual agreements with a third in its inclusion in this thesis.
Signature	Date 29/12/2021

Name of Co-Author	Abdul Hamid Sheikh
Contribution to the Paper	Supervision, research conceptualisation, and model development (30%)
Signature	Date 29/12/2021

Name of Co-Author	Mohamed Elchalakani		
Contribution to the Paper	Manuscript revision (5%)		
Signature		Date	29/12/2021

Name of Co-Author	Tianyu Xie		
Contribution to the Paper	Data curation (5%)		
Signature		Date	29/12/2021

Structural Performance and Analysis of Asymmetrically Skewed and Curved Ultra-High Performance Fibre Reinforced Concrete Slabs

M.S. Mohamed Ali[1], S. Mahdi[2*], A.H. Sheikh[3], M. Elchalakani[4], T. Xie[5]

[1]Dr. Mohamed Sadakkathulla Mohamed Ali
Senior Lecturer
School of Civil, Environmental and Mining Engineering
The University of Adelaide
South Australia, Adelaide 5005
AUSTRALIA
Email: mohamed.mohamedsadakkathulla@adelaide.edu.au

[2]Mr. Shahin Mahdi (Corresponding author) *
Ph.D. Candidate
School of Civil, Environmental and Mining Engineering
The University of Adelaide
South Australia, Adelaide 5005
AUSTRALIA
Email: shahin.mahdi@adelaide.edu.au

[3]Associate Professor Abdul Hamid Sheikh
Associate Professor
School of Civil, Environmental and Mining Engineering
The University of Adelaide
South Australia, Adelaide 5005
AUSTRALIA
Email: abdul.sheikh@adelaide.edu.au

[4]Dr. Mohamed Elchalakani
Senior Lecturer
School of Civil, Environmental and Mining Engineering
The University of Western Australia
Western Australia, Perth 6009
AUSTRALIA
Email: mohamed.elchalakani@uwa.edu.au

[5]Dr. Tianyu Xie
Research Assistant
School of Civil and Infrastructure Engineering
RMIT University
Victoria, Melbourne 3000
AUSTRALIA
Email: anson.xie@rmit.edu.au

Structural Performance and Analysis of Asymmetrically Skewed and Curved Ultra-High Performance Fibre Reinforced Concrete Slabs

M.S. Mohamed Ali[1], S. Mahdi[2*], A.H. Sheikh[3], M. Elchalakani[4], T. Xie[5]

ABSTRACT

The present study investigates the structural performance of asymmetrically skewed and curved ultra high-performance fibre-reinforced concrete (UHPFRC) slabs/bridge decks through both experimental and theoretical investigations. Four slabs were constructed with varying skew and curvature angles and tested under increasing concentrated loading. In addition to the experimental program, closed-form models based on the method of virtual work and Castigliano's second theorem were developed to predict the reaction forces and deflections at the mid-span of the skewed and curved slabs within the linear elastic state. Closed-form solutions were developed based on yield-line theory in conjunction with a mechanics-based moment-rotation model to predict deflections at the ultimate state, and a thorough finite-element analysis implementing non-linear material models in conjunction with damage modelling was performed to observe the full-range structural performance of the slabs. A parametric study was performed to examine the effect of skew and curvature angle on deflection, shear, bending and torsion. The generic analytical procedures and finite-element model were compared against experimental results obtained from the study and results show that the models can be applied to UHPFRC asymmetrically skewed and curved slabs.

Keywords: ultra-high performance fibre-reinforced concrete; skewed slab; curved slab; bridge deck; virtual work, finite-element modelling.

1. INTRODUCTION

The rapid increase of population growth and urbanisation has led to increased traffic and consequently the need for curved and skewed bridges in both urban and mountainous areas [1]. Moreover, skewed and curved slabs are used in floor systems and cantilevered slabs for balconies of multi-storey buildings where architectural designs lead to space limitations and the need for slabs of varying geometry [2]. Due to their geometry, skewed and curved slabs are susceptible to multiple modes of failure. The collapse of skewed bridges such as the Rio Bananito in Costa Rica [3], the Gavin Canyon undercrossing in Northridge [4] and the Americo Vespucio/Miraflores in Chile [5] are examples of failure due to in-plane rotations about the pier and support, with skew angles the primary factor in seismic failure of those structures [6, 7]. Skewed slab design and support arrangements are critical due to the longitudinal and transverse bending, torsion and warping of the structure. with the combination of torsional and bending moments the most detrimental to the superstructure [8, 9]. Structural slabs with a skew angle of 20° or more are subject to large variation in shear and moment distribution and require more rigorous assessment whereas slabs with skew angles of less than 20° can be analysed using standard slab theory [10-12]. Moreover, horizontally curved bridge slabs encounter significant flexural and torsional moments due to the load eccentricity from the supports, and the behaviour becomes more complex as the curvature angle increases. Canadian and American codes and guidelines [13, 14] outline that bridge decks of curvature angles of less than 12° are subject to regular slab analysis whereas a more thorough approach is required for larger curved slabs. Additionally, distortion is a significant factor in the failure of curved bridges and is exacerbated with an increasing curvature for bridge deck slabs [15].

The most used material in the design and construction of bridge decks and slabs are steel-reinforced concrete (RC). However, precast RC slabs and bridge decks incur large annual

maintenance costs with reinforcement corrosion leading to approximately $13.6 billion dollars in the repair of highway bridges [16]. The economic impact and safety concerns have directed research towards developing bridge decks and slabs with prolonged lifespans [17]. One such improvement is the adoption of advanced cementitious materials such as ultra-high performance concrete (UHPC). Ultra-high performance concrete is a newly-developed cementitious material which provides superior strength, durability, and life-span in comparison to conventional concrete [18]. Research has grown progressively in UHPC slab assessment and design [19, 20], however UHPC under tension exhibits cracking followed by brittle failure [21]. This is minimised with the addition of steel fibres, resulting in the emergence of ultra-high performance fibre-reinforced concrete (UHPFRC). UHPFRC provides superior tensile strength and strain hardening properties, and the inclusion of steel fibres provides additional ductility in the post-cracking region as microcracks in the concrete are bridged by steel fibres, and this minimises crack widths in the tensile region [22]. The cost of UHPC and UHPFRC are greater than regular concrete for precast structures, however their mechanical advantages eliminate or greatly reduces the amount of conventional steel reinforcement required which leads to reduced labour and quality control costs in addition to reduced member sizes and batch volume [23]. For slabs more specifically, this results in the avoidance of complicated reinforcement carcasses and, thus, reducing slab thicknesses. Moreover, research on UHPC and UHPFRC has progressively refined mix designs by using conventional materials [24, 25] and the use of locally sourced materials in conjunction with optimised mix designs further reduces these costs. More significantly, studies into the lifespan assessment of UHPC/UHPFRC and RC bridges have shown that whilst UHPC/UHPFRC have higher initial construction costs, they are annually more economical to maintain, with lifespans at least twice that of RC structures [26]. These characteristics make UHPFRC an ideal cementitious material for slab and bridge deck construction. UHPFRC has been adopted in the construction of bridges

as early as 1997 with the construction of the Sherbrooke footbridge, Canada, in 2002 the Seonyu Footbridge in Seoul, South Korea [27], and the resurfacing of existing RC bridge decks with UHPFRC in Central Switzerland [28]. Research at the University of Adelaide [29] has studied the structural behaviour of regularly skewed UHPFRC slabs, however research on UHPFRC has received little attention with regards to asymmetrically skewed and curved slabs which are common in continuous-spanning bridge deck systems and buildings. To address these shortcomings, this study aims to:

(1)   Study the structural behaviour of one-way UHPFRC slabs/bridge deck elements with varying skew and curvature angles through a small-scale experimental program,

(2)   Develop closed-form mechanics-based models based on the method of virtual work and Castigliano's second theorem to predict the deflections and reaction forces at the ultimate limit state for skewed and curved slabs,

(3)   Develop a modified approach to the yield-line theory [29] to determine the failure load at the ultimate limit state for skewed slabs in conjunction with a mechanistic approach in determining the moment capacity [30], and

(4)   Conduct a detailed finite-element analysis incorporating a concrete damage plasticity model to adequately simulate both the elastic and post-elastic behaviour of the slabs, using a refined code (ABAQUS).

To realise the above objectives, two asymmetrically skewed slabs with skew angles of 25° and 45° and two horizontally curved slabs with curvature angles of 60° and 90° were fabricated and subjected to monotonically increasing concentrated loads at various locations along the slab length. The deflections at various locations along the slabs are measured for the increasing load and are recorded to validate the aforementioned closed-form models and finite-element

149

analysis. This research is an extension to previous research by Xie et al. [29] at the University of Adelaide, where the structural performance of regularly skewed UHPFRC slabs/bridge deck elements were studied.

The expected outcomes of the research are further understanding the influence of skew and curvature angles for UHPFRC slabs at both the elastic and ultimate state limits, the development and validation of approaches designed to predict the behaviour of skewed and curved slabs in both the elastic and ultimate state limits, and therefore work towards the development of guidelines and approaches to the design and construction of UHPFRC skewed and curved slabs.

2. EXPERIMENTAL PROGRAM

2.1. Skewed and curved slab test specimens

2.1.1. *UHPFRC mix design*

In the current study, a UHPFRC mix design developed previously at the University of Adelaide [24, 31] was modified to facilitate for a differing sulphate resistant cement, shown in Table 1.

	Sulphate Resistant Cement (kg)	Silica Fume (kg)	Sand (kg)	Water (kg)	Superplasticiser (kg)	Steel Fibres (kg)	w/b ratio
UHPFRC	0.79	0.21	1	0.12	0.06	0.233	0.12

Table 1 – Mix proportion of UHPFRC mix for the current study.

The sulphate resistant cement (nominal compressive strength of 60 MPa) and silica fume were used as the binding agents to produce a concrete with high packing density and low

permeability. The sand was a natural river washed sand which was sieved before being added to the dry mix as a fine aggregate. The dry ingredients (sand, cement and silica fume) was mixed thoroughly in a planetary cement mixer for 5 minutes, then water and superplasticiser (*Sika ViscoCrete 10*) were added to the dry mix and mixed for an additional 10 minutes. The steel fibres with a nominal length of 13 mm and diameter 0.2 mm, and Young's elastic modulus and ultimate strength of 210 GPa and 2850 MPa respectively, were added to the cementitious mix at peak flowability. This was mixed for an additional 5 minutes to ensure homogeneity throughout the mix before casting into the specimen moulds. The target strength of the mix was 135 MPa for a pour volume of 0.48 m^3.

2.1.2. *Slab configurations*

Four UHPFRC one-way slabs (two asymmetrically skewed and two curved) were tested with varying skew (25° and 45°) and curvature angles (60° and 90°). These angles were deemed as critical in understanding skew and curvature behaviour as bridge deck members. The skew slab dimensions at centre are 1500 mm × 720 mm × 60 mm with a clear span of 1420 mm. Fig. 1 illustrates the configuration of the skewed slabs investigated in this study.
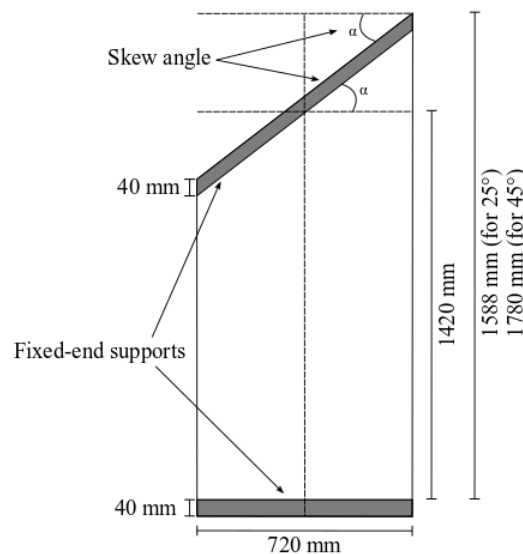

Figure 1 – Description of UHPFRC skewed slab.

The asymmetrically skewed slab angle is defined as the angle between support lines relative to the line normal to the longitudinal axis of the slab as denoted in Fig. 1. The elongated edge length of the slabs are 1588 mm and 1780 mm for the 25° and 45° skewed slabs, respectively.

The curved slab dimensions are 1420 mm × 720 mm × 60 mm, however in the case of a curved structural element, the specified length is a circumferential measurement and is taken from the centre of the supports. The angle of curvature is defined as the angle measured support to support and this provides variance for the lengths of the slab specimens. The configuration of the curved slabs is shown in Fig. 2.
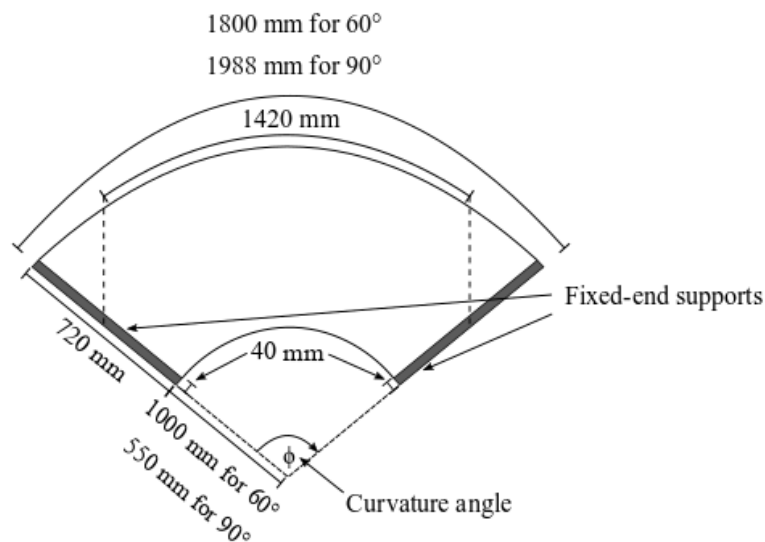

Figure 2 – Description of UHPFRC curved slab.

The specimen circumferential lengths for the 60° and 90° slabs are 1800 mm and 1988 mm, respectively. The slabs were reinforced with square steel reinforcing mesh of 4 mm diameter and 100 mm spacing, placed at the section centroid to provide additional flexural stiffness. The slabs were clamped at the ends to replicate end conditions observed for continuous bridge decks and one-way slabs [32] which incur a combination of torsional and flexural moments at their span ends. To ensure zero rotation at the ends, two 40 mm thick steel plates were clamped by

four 22 mm diameter bolts (two at each end of the plates). A closer inspection of the bolted
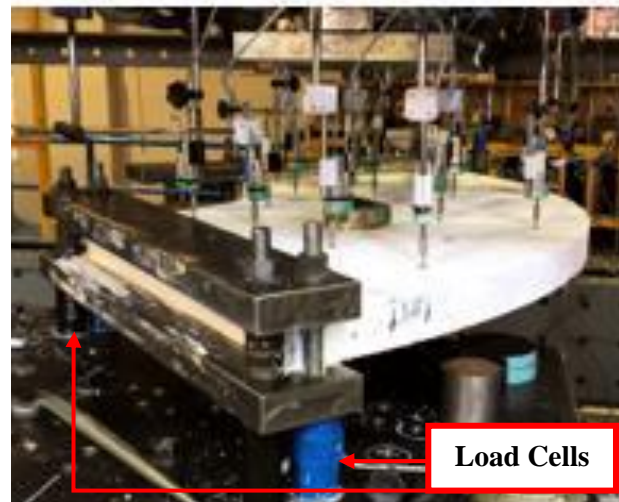
clamp support is shown in Fig. 3.

Figure 3 – Bolted plate support for UHPFRC slabs.

2.1.3. *Testing and instrumentation*

For loading of the UHPFRC skewed and curved slabs, two loading phases were explored. In

the first phase, loads were applied up to a maximum load at four designated points to observe

reaction forces at the fixed-end supports and subsequent deflection profiles within the elastic

loading range with the use of linear variable differential transformers (LVDT) and load cells.

The position of the load points as well as the LVDT's for the loading of UHPFRC skewed and
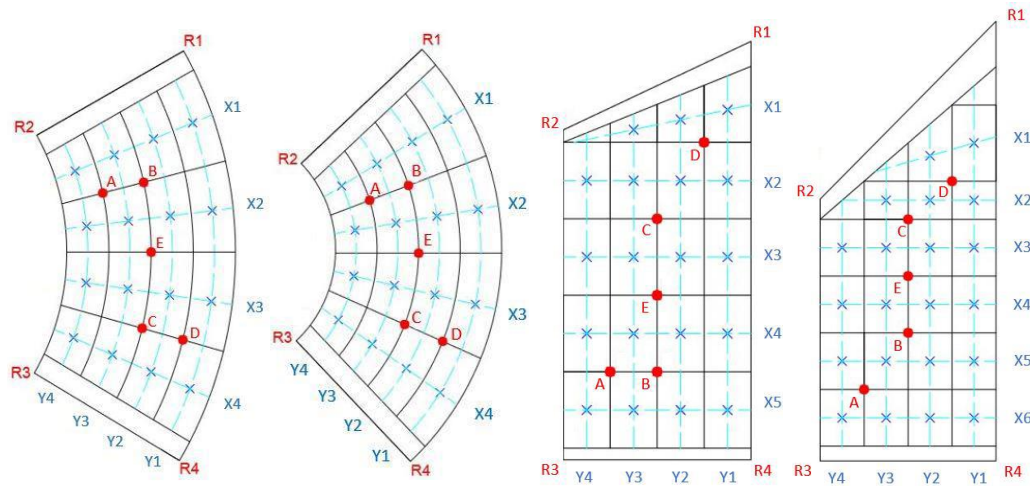
curved slabs are seen in Fig. 4.

Figure 4 – Loading and LVDT positioning for test of UHPFRC skewed and curved slabs.

The maximum load magnitude used to assess reaction forces (20 kN) was selected based on findings from previous studies on skewed UHPFRC slabs [29] to establish a large spread of data whilst ensuring the section remained in the linear elastic state. The slabs were divided into 4x4 grids from the termination of the supports (R1, R2, R3, R4) and were used for the placement of LVDT's and loading points (A, B, C, D, E). The loading points were positioned adjacent to the slab centres along the centre-line (B and C) and near the corners (A and D). The load positions were selected as they were critical cases for both skewed (at the acute corners) and curved (at both inner and outer curvature corners) slab loading scenarios. For the second phase of loading, slabs were loaded at the slab centres (E) and loaded up to failure. The loads were applied via a hand-driven hydraulic jack and through a steel circular loading plate of 115 mm diameter and 40 mm thickness. Load control was used for the application of the load, with a rate of 5 kN/min for both elastic and failure loading phases. The position of the LVDT's are indicated by crosses which are at intersections of blue gridlines drawn through the centre of the grids (X1 – X6, Y1 – Y4), for which a total of 22 LVDT's were used to measure the vertical

deflection along the slab length. To measure the reaction forces, load cells were placed at the corners of the supports as shown by the blue load cells below the supports in Fig. 3.

2.2.   Testing of material properties

2.2.1. *UHPFRC compression tests*

To obtain the compressive strength (f'_c), Young's modulus (E_c) and Poisson's ratio (v) of the UHPFRC, uniaxial compression tests were conducted on three cylindrical specimens with 100 mm diameter and 200 mm height as per AS 1012.9:2014 [33]. The specimens were tested under a loading rate of 0.3 MPa/s and 2 linear variable differential transformers (LVDT) were placed to measure the displacement of the cylinder under loading. Additionally, four 30 mm strain gauges were placed orthogonally at mid-height of the surface of two of the three specimens and loaded beyond the peak load to establish a compressive stress-strain relationship.

2.2.2. *UHPFRC direct tension tests*

To experimentally obtain the stress-strain behaviour of UHPFRC under direct tension, two dog-bone shaped specimens were horizontally cast and tested under uniaxial direct tension which are shown in Figs. 5 (a) – (c). The dimensions of the dog-bone specimens consist of a central shank with a square cross-section of 120 mm × 120 mm with a length of 325 mm. In order to avoid stress concentrations under tension, the specimen is tapered at its ends with square dimensions of 208.6 mm and a total specimen length of 604.8 mm (Fig. 5 (a)). The specimen dimensions are devised by Singh et al. [31] and are a modification to dimensions proposed by Redaelli [34] and Moreno et al. [35]. The specimens were tested under displacement control at a constant rate of 0.01 mm/s and the displacement was measured using 2 LVDT's. The specimens were placed in a specifically designed test rig (Figs. 5 (b) and (c))

and curved surfaces coated in gypsum paste to ensure contact between the test rig and specimens during the loading procedure.
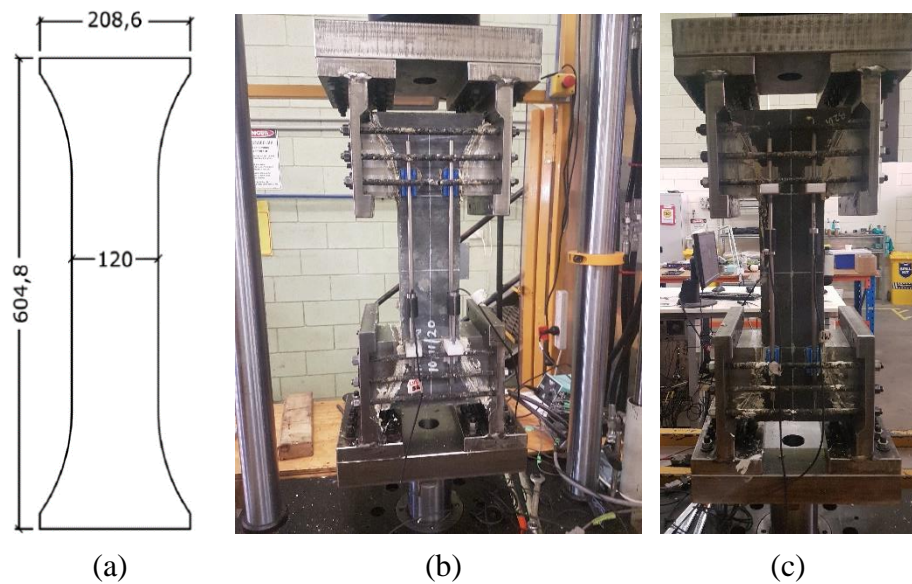

(a)   (b)   (c)

Figure 5 – Direct tension test: a) Dog-bone specimen dimensions [31] (dimensions in mm); b) and c) Direct tension test setup.

2.2.3. *Steel reinforcement tension tests*

To obtain the stress-strain relationship and relevant properties of the steel reinforcement mesh, specimens were cut and placed under uniaxial tension. Six 4 mm diameter specimens of a length of 300 mm were cut and placed in grips. Two 5 mm strain gauges were placed on opposing sides of the specimen centre which were ground for the gauges to be seated properly during testing. A constant loading rate of 2 kN/min was used until rupture was achieved.

3. EXPERIMENTAL RESULTS AND DISCUSSION

3.1. Determination of material properties

3.1.1. *UHPFRC compressions tests*

Three cylindrical specimens were tested under pure compression, from which two were strain gauged to observe the stress-strain behaviour. The average of the three tests was taken and established a mean 28-day compressive strength (f'_c) of 130.4 MPa with a standard deviation of 3.44 MPa and coefficient of variation of 0.026, a Young's modulus (E) of 58.5 GPa, and Poisson's ratio (v) of 0.235. An average compressive stress-strain relationship of the strain gauged specimens is shown in Fig. 6.
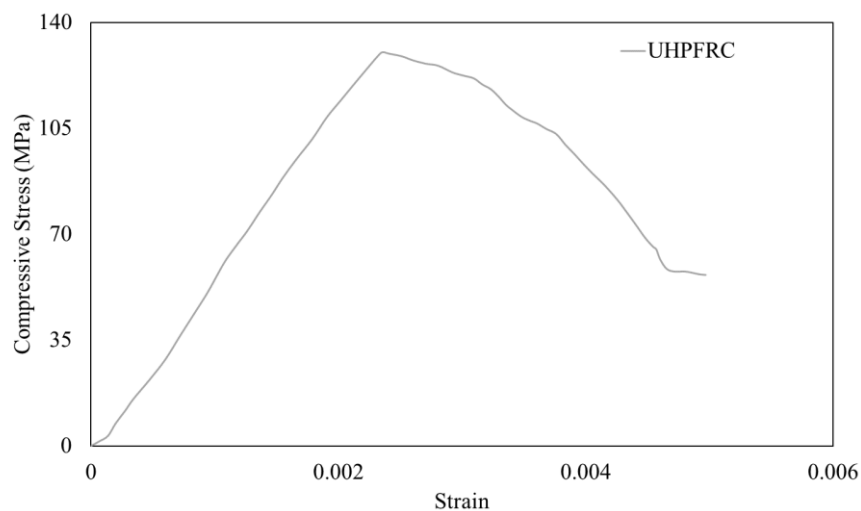

Figure 6 – Compressive stress-strain relationship of UHPFRC.

The behaviour is as expected in the pre-peak region, remaining linear up to the peak stress before a rapid loss in strength, stabilising at approximately 50% of the peak strength before compressive failure with no visible deformation observed in the pre-peak phase. The large post-peak residual strength and softening range is owed to the fibres within the concrete matrix. The deformation in the post-peak region is highlighted by the formation of a wedge however the damage is alleviated by the presence of the fibres. To evaluate the strain, both strain gauge

readings and LVDT data are used. The strain gauge data are accurate during the pre-peak phase of loading, however post-peak strains are immeasurable due to strain and damage localisation at the mid-height where the gauges are located. To overcome this, the displacement during the loading procedure measured by the LVDT's was divided by the original specimen length to obtain global strain over the specimen and this was used post-peak, whereas the strain gauge measurements were used pre-peak to develop the stress-strain relationship.

3.1.2. *UHPFRC direct tension tests*

Two dog-bone specimens were tested under direct tension to observe both the stress-strain and stress-crack width relationships which are shown in Figs. 7 (a) and (b).
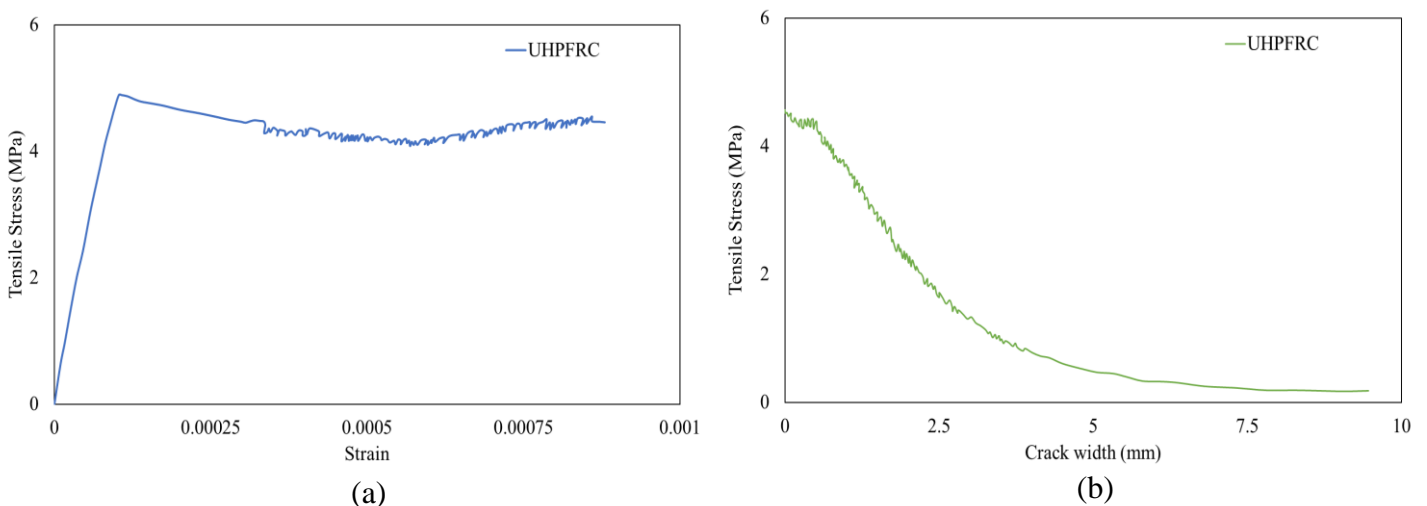

(a)   (b)

Figure 7 – Tensile properties of UHPFRC: (a) stress-strain relationship of UHPFRC; and (b) Tensile stress vs. crack width relationship.

The first crack initiated at a stress of 4.4 MPa, indicated by Fig. 7 (b) however an additional stress of 0.5 MPa was applied before the peak tensile strength was attained (Fig. 7 (a)). This is owed to the fibres within the specimen matrix which bridged the crack and resist the stresses

at the crack face before attaining peak strength. A peak stress of 4.9 MPa was followed by a reduction in capacity in the specimen as the applied load decreased and cracks widened until tensile failure of the specimen occurred. Crack widths were estimated by using LVDT measurements in conjunction with material properties attained from the cylinder test data, using the following equation:

$$w_{cr} = \frac{PL}{E_c A} - \Delta_{total} \tag{1}$$

It was assumed that total deformation of the dog-bone specimen contained both elastic and inelastic deformations and that the inelastic portion was coupled with the cracking width. This assumption has been previously verified in research on strain and crack width calculations for UHPFRC specimens in tension [36].

3.1.3. *Steel reinforcement tension tests*

Six steel reinforcement specimens were placed under uniaxial tension to obtain the stress-strain relationship. The specimens were 300 mm in length and 4 mm diameter, and resulted in an average yield strength, ultimate strength, and elastic modulus of 500 MPa, 625 MPa, and 195.5 MPa, respectively.

3.2. Testing of skewed and curved UHPFRC slabs

3.2.1. *Loading - elastic range*

Loads were applied at the designated locations (*A*, *B*, *C*, and *D*) within the elastic range and the results for reaction load proportions are shown in Figs. 8 and 9.
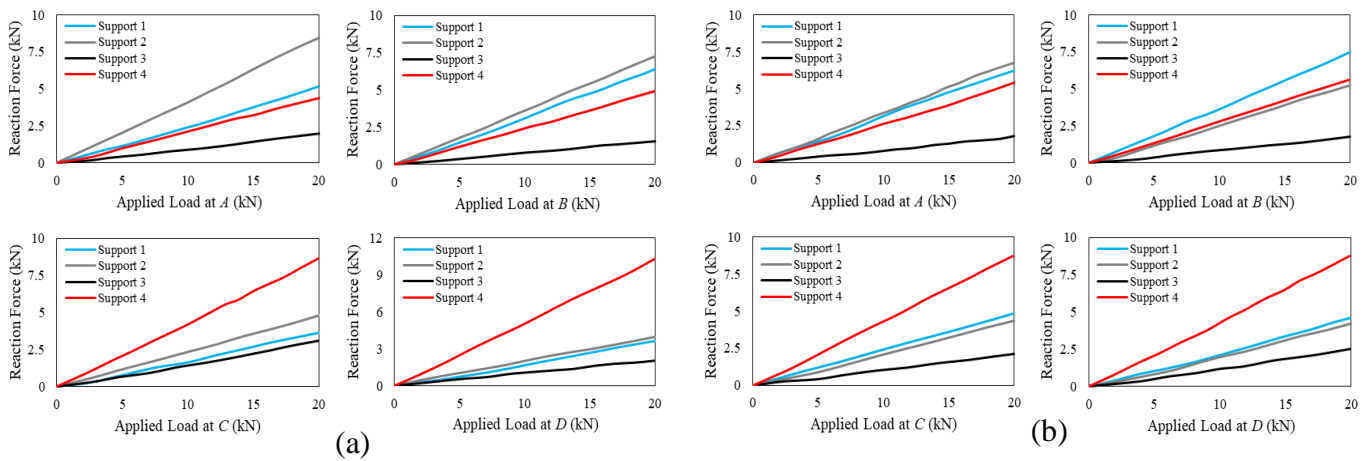
Figure 8 – Reaction forces at supports within elastic loading region for: (a) 60°; and (b) 90° curved UHPFRC slab vs. applied load.
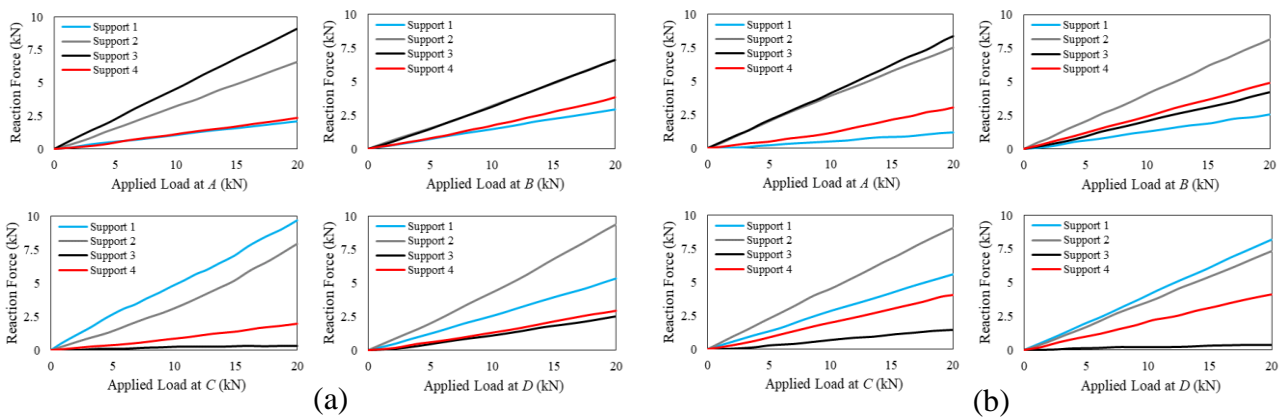

Figure 9 – Reaction forces at supports within elastic loading region for: (a) 25°; and (b) 45° skewed UHPFRC slabs vs. applied load.

Figs. 8 (a) – (d) illustrate the relationship between the load applied at locations *A*, *B*, *C* and *D* and their corresponding reaction forces at the supports for curved slabs with curvature angles of 60° and 90° respectively. It is shown that when loading was applied to the curved slabs at points *A* and *D*, the reaction force measured at the support that has shorter distance to the loading points exhibited larger reaction forces than those further away to the loading point. In

160

addition, it was observed that when loading was applied at points *A* and *D*, the reaction forces measured at support 1 increased with increasing curvature of the slab under same loading condition. For cases where loads were applied at the centreline of the slabs as indicated in Fig. 4, the increase in curvature of the slabs would result in the increase of reaction forces at supports 2 and 4, whereas the reaction force at support 1 would decrease. Furthermore, it indicates that the curvature angle of curved slabs only had a slight effect on the variance of reaction forces across the four supports.

Figs. 9 (a) – (d) illustrate the relationship between the load applied at locations *A*, *B*, *C* and *D* and their corresponding reaction forces at the supports for skewed slabs with skew angles of 25° and 45° respectively. It is demonstrated that when load was applied to the skewed slabs at points *A* and *D*, the reaction forces measured at the nearer supports are larger than the supports further away. It was observed that when loading was applied at points *A* and *D*, the reaction force measured at support 4 increased with the increasing of the skew angle of the slab whereas the reaction force at support 1 decreased. For the cases of loads applied at the centreline of the slabs, the increase in skewness of the slabs resulted in the increase of reaction force at support 4 whereas the reaction forces at support 3 decreased. It can be concluded that with increasing skewness of the slabs, support 4 experiences an increase in reaction force. A key difference noted between the two slab systems is that when load was applied to point *C* for the 25° slab and *D* for the 45° slab, support 3 experienced little to no reaction force.

3.2.2. *Loading – to failure*

In addition to the observations made in the elastic range, the specimens were loaded at the mid-span up to failure to observe the failure modes and cracking patterns of the skewed and curved slabs. The crack patterns and locations of failure are shown in Figs. 10 (a) – (f).
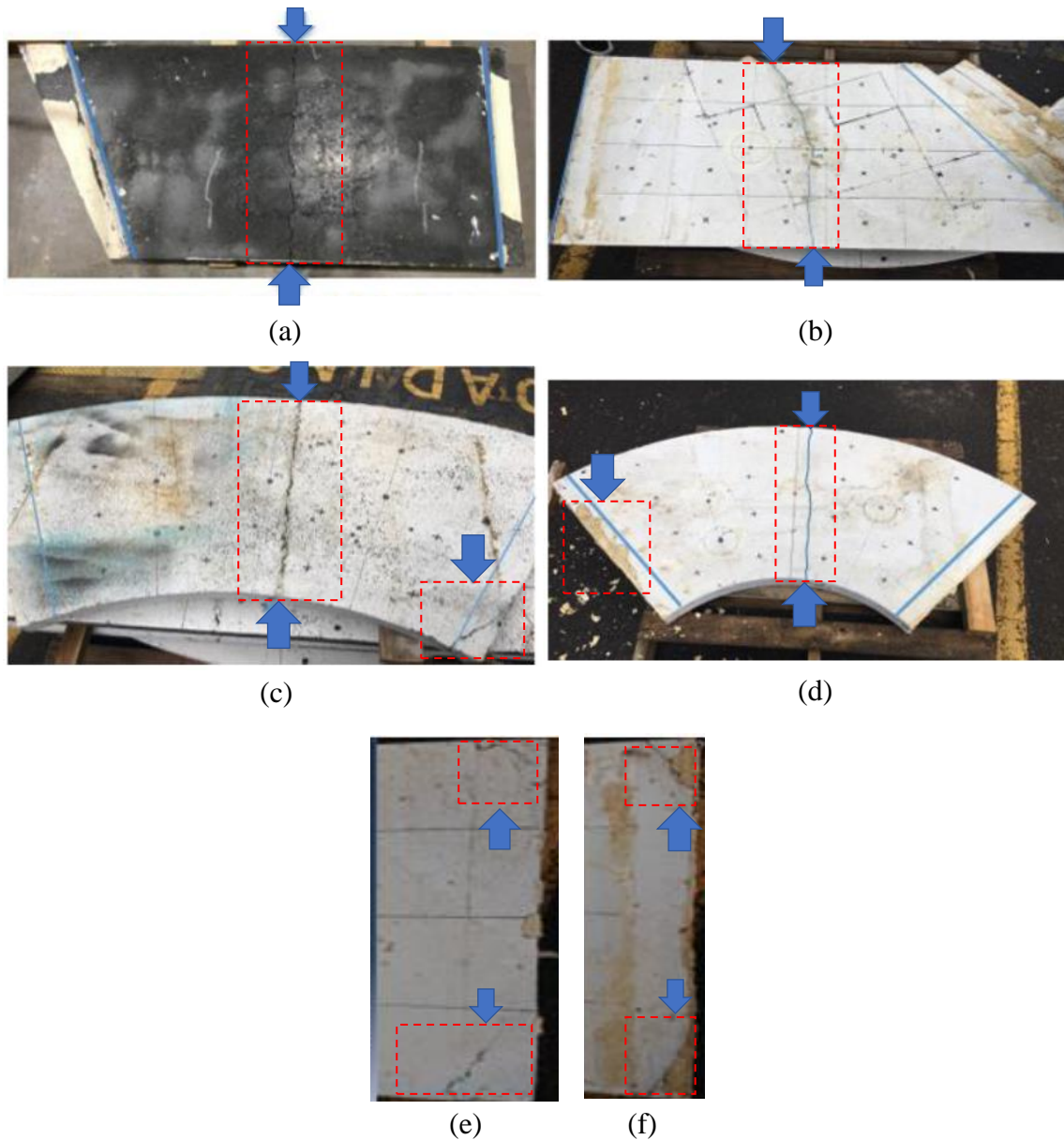
Figure 10 – Failure modes and locations of UHPFRC slabs: (a) skewed 25°; (b) skewed 45°; (c) curved 60°; (d) curved 90°; (e) skewed 25° at straight support [bottom face]; and (f) skewed 45° at straight support [bottom face].

It was observed that the primary tensile crack had formed at the mid-span for each of the slabs, with minor cracking observed adjacent to the primary cracks. However, cracks which developed in the skewed slab specimens were slanted and more prominently seen in the 45° skewed slab (Fig. 10 (b)). There were also signs of damage at the supports of the curved slabs

as indicated in Figs. 10 (c) – (f). Diagonal cracking can be seen at the corner of the 60° curved slab (Fig. 10 (c)) and spalling of the concrete cover at the left support of the 90° curved slab (Fig. 10 (d)). Moreover, inspection of the bottom surface of the skewed slabs revealed diagonal cracks at the support corners. The load-deflection relationship at the mid-span for the skewed and curved UHPFRC slabs is shown in Fig. 11. Failure of all four slabs is attributed to the collapse of the slabs as the primary tensile crack propagated through the slab sections for each case.
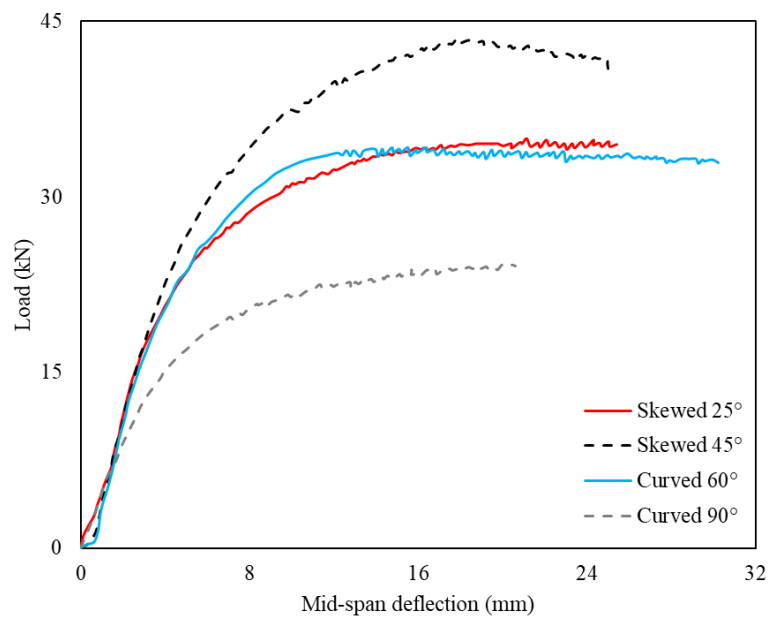

Figure 11 – Experimental load vs. mid-span deflection relationship for curved and skewed UHPFRC slabs.

There is a significant difference in load capacities between the varying skew and curvature UHPFRC slabs as seen in Fig. 11. A 25% increase in capacity was observed for 45° skewed slab when compared to the 25° skewed slab, however the peak was reached at a larger deflection. There was a 40% increase in capacity observed for the 60° curved slabs when compared to the 90° curved slabs. This significantly large difference in load capacities is owed to the 90° curved slab having a larger eccentricity between the load points and its supports. The

larger curvature induces larger torsional moments which would significantly reduce the load carrying capacity of the slab. Moreover, it was noted there was an increase in capacity for a larger skew between the two skewed slabs. This is due to shortening of the load path between the angled and straight supports as the skew angle increases, which results in a smaller lever arm and reduction in both bending moments and deflections [37].

4. ANALYTICAL MODELS

For this study, both analytical and numerical models are utilised to predict the response of the structure. However, this section presents development of three analytical models: one for modelling the curve slabs while the other two for the asymmetrically skew slabs. Castigliano's second theorem (CST) has been used for developing the model for curve slabs whereas the two models for skew slabs are developed using the method of virtual work and yield line analysis. All three modes provide closed-form solutions and can accurately predict the load capacity, deflection, torsion, and bending moment for different slab geometries.

4.1. Asymmetrically skewed UHPFRC slab models

4.1.1. *Method of virtual work for predicting mid-span deflection*

Fig. 12 (a) shows the geometry of the skew slab, which is supported along the inclined side *CF* and the opposite side *DE*. Both supports are treated as fully fixed in accordance with the supporting system used for laboratory testing of the slabs. As the two opposite edges parallel to *x* (*CD* and *EF*) are unsupported, the deformation of the slab is assumed to have predominantly one way bending. This assists to idealise the deformation of the slab with a 1D member along *AB* having bending and torsional modes of deformations (Figs. 12 (b) and (c)). Though this idealisation simplifies the analysis of the structure, it still possesses some challenges as it is statically indeterminate. The method of virtual work is applied to the present

164

problem to overcome the static indeterminacy in order to derive closed-form solutions for mid-span deflection and reaction forces.
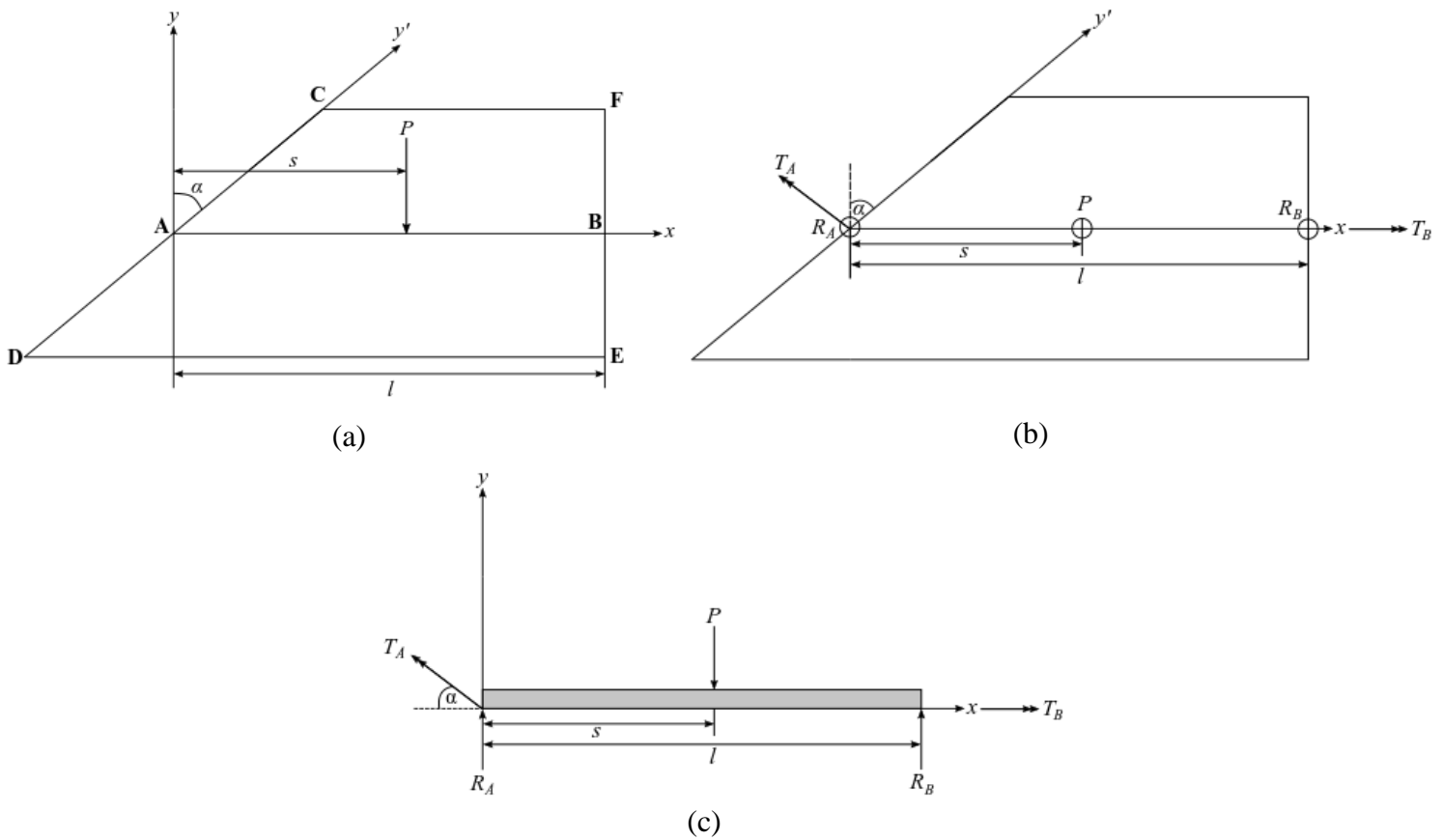

(a)

(b)

(c)

Figure 12 – Skewed slab schematics: a) top view with axis system; (b) reaction at supports (top view); and (c) reactions at supports (side view) for the method of virtual work.

The 1D idealisation results in support edges *CD* and *EF* to be lumped at *A* and *B* as fixed supports. Point load *P* is applied to the asymmetrical slab of length *l* and skew angle α at a distance *s* from support *A*. Torsional moments are resolved at the supports (T_A, T_B) along with reaction forces (R_A, R_B) which are highlighted in Figs. 12 (b) and (c). The torsional moment at *A* (T_A) is perpendicular to the angular edge which results in moment components for both directions. These are separated before equilibrium is applied to generate expressions for reaction forces R_A and R_B:

$$R_A = \frac{Ps}{l} + \frac{T_B \tan \alpha}{l} \tag{2}$$

$$R_B = \frac{P(l-s)}{l} - \frac{T_B \tan \alpha}{l} \tag{3}$$

The generic equations for the bending and torsional moments across the idealised structure are:

$$M(x) = \frac{T_B \tan \alpha}{l}(l - x) + \frac{P(l-s)}{l}x - P\langle x - s \rangle \tag{4}$$

$$T(x) = T_A \cos \alpha = T_B \tag{5}$$

The method of virtual work is applied to the problem for which a virtual slab is developed where unit loads and moments are applied to solve the indeterminate structure. A unit torsional moment is applied at B for the virtual system which results in the following bending and torsional moment distributions:

$$m_\phi(x) = \frac{\tan \alpha(l-x)}{l} \tag{6}$$

$$t_{phi}(x) = t_A \cos \alpha = 1.0 \tag{7}$$

The method of virtual work is applied for the fixed support at B which gives the condition:

$$\phi_B = \int_0^l \left(\frac{Mm_\phi}{EI} + \frac{Tt_\phi}{GJ} \right) dx = 0 \tag{8}$$

The condition in Eq. (8) is solved to give:

$$T_B = -\frac{P \tan \alpha(l-s)(2l-s)s}{2l^2(\tan^2 \alpha + 3k)} \tag{9}$$

where k is the bend-to-twist ratio (EI/GJ). Eq. (9) is substituted into Eqs. (4) – (5) for the bending and torsional moment distributions which become:

$$M(x) = -\frac{P \tan^2 \alpha(l-s)(2l-s)s}{2l^3(\tan^2 \alpha + 3k)}(l - x) + \frac{P(l-s)}{l}x - P\langle x - s \rangle - M_{FEM} \tag{10}$$

$$T(x) = -\frac{P \tan \alpha(l-s)(2l-s)s}{2l^2(\tan^2 \alpha + 3k)} \tag{11}$$

where M_FEM is the fixed end moments of the idealised structure based on the position of the point load P. The same process is applied to generate the following distribution for the slab deflection:

$$\Delta = \frac{Px}{6EIl}(l-s)(2lx-s^2-x^2) + \frac{Ps^2 \tan^2 \alpha}{12EIl^3(\tan^2 \alpha+3k)}(l-s)^2(2l-s)^2 \text{ for } 0 \le x \le s \quad (12)$$

$$\Delta = \frac{Ps}{6EIl}(l-x)(2lx-s^2-x^2) + \frac{Ps^2 \tan^2 \alpha}{12EIl^3(\tan^2 \alpha+3k)}(l-s)^2(2l-s)^2 \text{ for } s \le x \le l \quad (13)$$

The equations derived for the deflections (Eqs. (12) and (13)) and reaction forces (Eqs. (2) and (3)) are used to generate predictions and are compared to the experimental findings which are shown in Table 2.

Specimen	Support Edge	Reaction Forces (kN)		Error (%)	Mid-span deflection (mm)		Error (%)
		Experimental	Theoretical		Experimental	Theoretical	
Skewed 25°	CD	17.62	18.22	3.41	0.95	0.80	15.8
	EF	2.34	1.78	23.9			
Skewed 45°	CD	14.47	13.74	5.05	1.46	1.75	19.9
	EF	5.45	6.26	14.9			

Table 2 – Comparison of experimental and theoretical results for the reaction forces at the supports and mid-span deflection of 25° and 45° skewed UHPFRC slabs.

The closed-form solutions provide sufficient predictions to the mid-span deflection for the 25° and 45° skewed slabs with percentage errors lying below 20%. Predictions made for the reaction forces at the skewed edge support *CD* are more accurate with percentage errors below 6% whereas predicted errors for the straight edge support *EF* lie below 24%. However, the larger prediction error percentage is owed to the lesser load magnitude whereas the load differences are less than 1 kN. The source of prediction error between theoretical and experimental results can be primarily attributed to the random orientation and dispersal of steel fibres in the specimen body. This assumption can lead to non-homogeneity whereas the model assumed homogenous material properties.

A parametric study was performed to observe the variation of bending moment, shear force, torsional moment, and deflection for varying bend-to-twist ratios, load positions, and slab skew angles using the developed expressions (Eqs. (2) – (3) & (10) – (13)) for a slab subjected to a unit load, with the results of the study shown in Figs. 13 – 19.
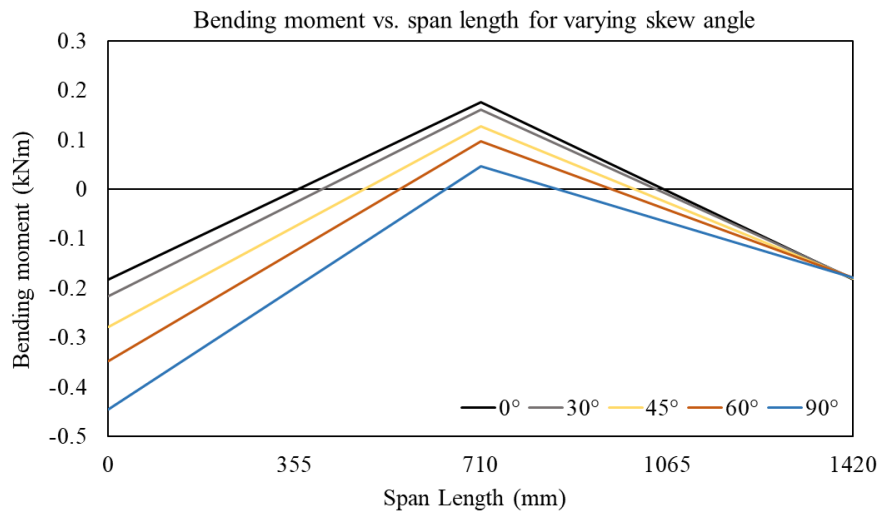

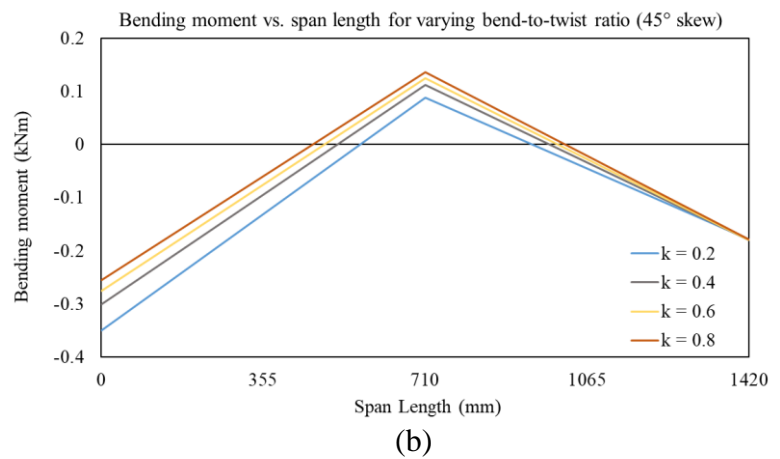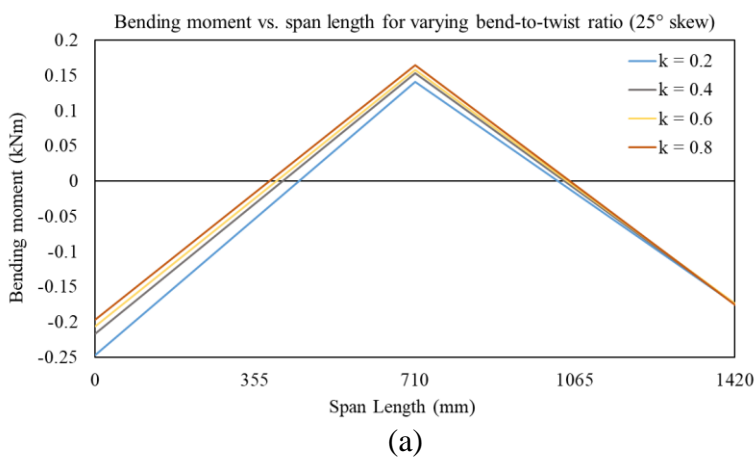**Figure 13 – Bending moment vs. span length for varying skew angle for asymmetrically skewed slab.**

(a)   (b)

Figure 14 – Bending moment vs. span length for varying bend-to-twist ratios: (a) 25° skewed slab; and (b) 45° skew slab.
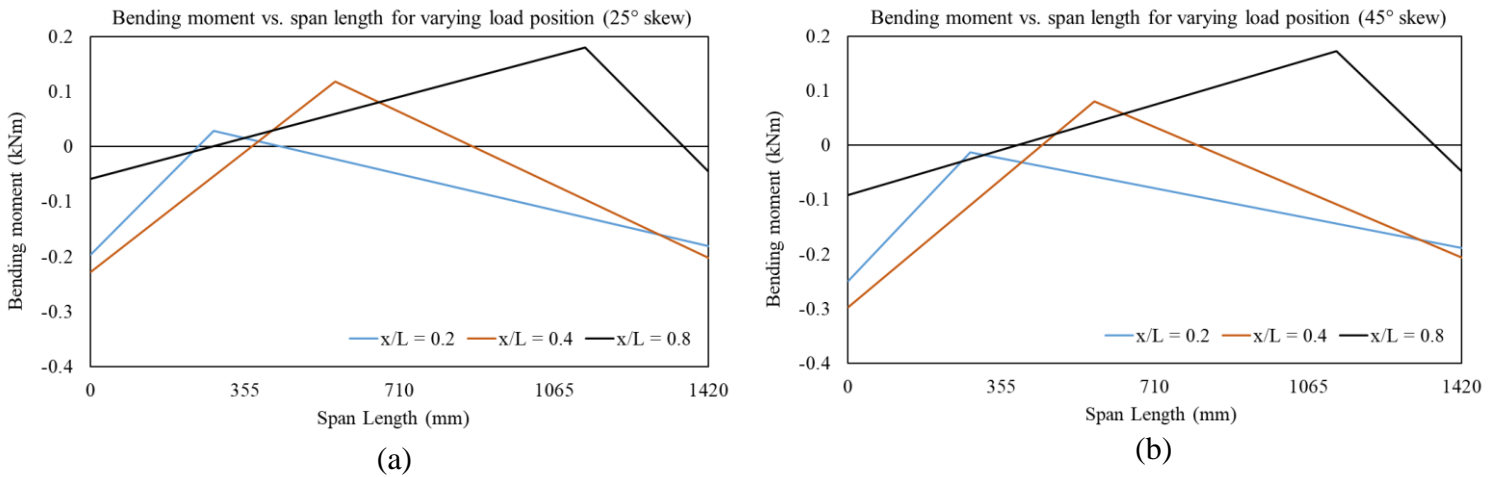
168

Figure 15 – Bending moment distribution along span length for varying load positions: (a) 25° skewed slab; and (b) 45° skew slab.

The variation of bending moment distributions of the asymmetrically skewed slab was plotted against the span length and are shown in Figs. 13 – 15. The bending moment distribution for a slab loaded at the mid-span was observed for varying skew angles (from 0° to 90°) for a fixed bend-to-twist ratio of 0.6175 (Fig. 13) illustrated the increase in negative bending moment at the support for an increasing skew angle. The influence of the bend-to-twist ratio k on the bending moment along the slab span was shown (Figs. 14 (a) and (b)) when the load was applied at the centre of slab on the central line and highlighted an increase in bending moment for an increase in bend-to-twist ratio. Lastly, the maximum bending moment of the slab for varying skew angle occurred when the applied load was near the non-skewed, or straight support, and the bending moment magnitude increased at the edge for an increasing skew angle (Figs 15 (a) and (b)). It should be noted that a skew angle of 90° is not a physically realistic value however is suitable to use as an upper limit for an envelope.
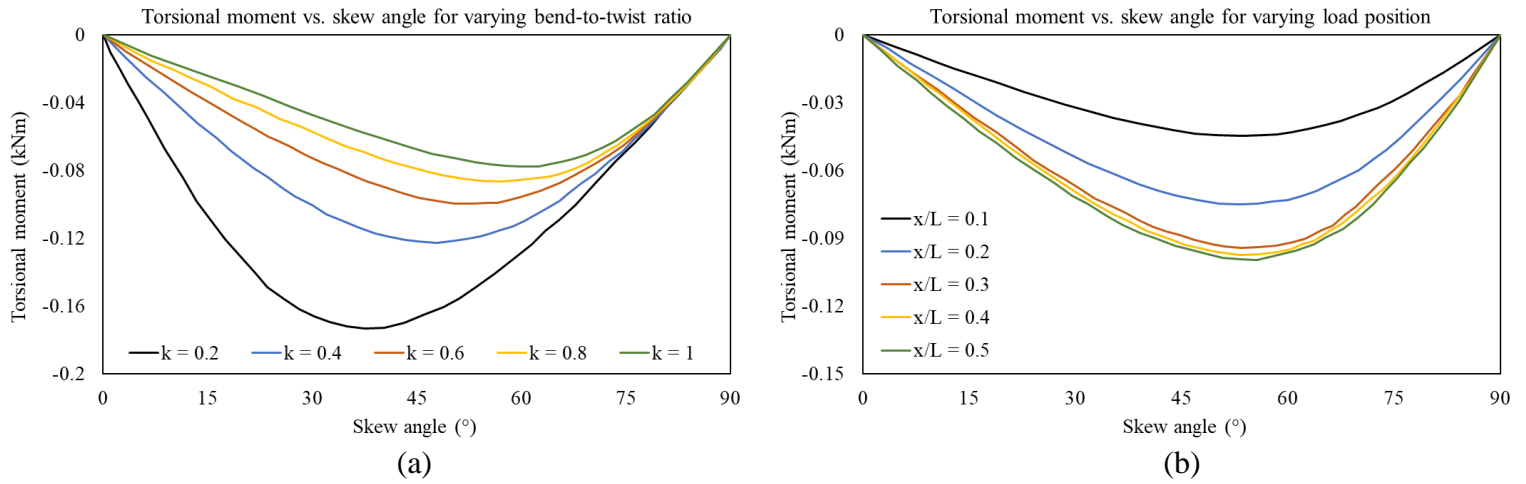
Figure 16 – Torsional moment vs. slab skew angle at the mid-span for: (a) varying bend-to-twist ratio; and (b) varying load position.

The variation of idealised torsional moment distributions of the asymmetrically skewed slab was plotted against skew angle and are shown in Figs. 16 (a) and (b). The study showed a decrease in torsional moment at the mid-span for an increase in bend-to-twist ratio (Fig. 16 (a)). Moreover, a decrease in torsional moment was observed for an increasing skew angle. Secondly, the influence of load position on the mid-span torsional moment was studied and indicated a decrease in torsion at the mid-span as the load position is further away from the mid-span. Additionally, it is shown that the maximum torsional moment at the mid-span occurred for a slab skew of 55° (Fig. 16 (b)). It should be noted that a bend-to-twist value of 0.2 is not a physically realistic value however is suitable to use as a lower limit for an envelope, as some materials are known to cross below the unit value threshold.
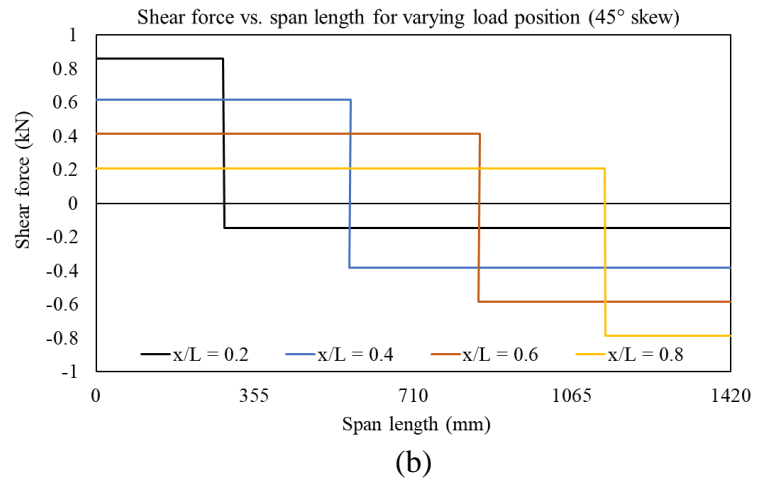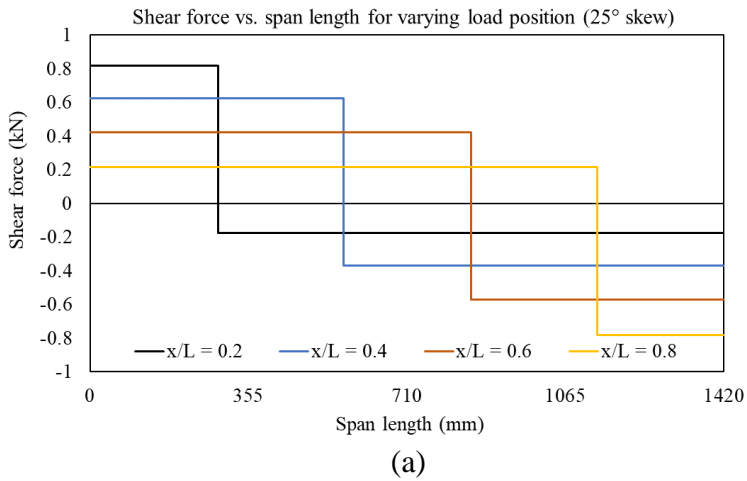
Figure 17 – Shear force distribution along span length for varying load position: (a) 25° skewed slab; and (b) 45° skew slab.

The variation of shear force for the asymmetrically skewed slab was plotted for varying load positions for both the 25° and 45° skew slab and are shown in Figs. 17 (a) and (b). The shear force profiles suggest that shear of the slabs is independent of skew angle but largely reliant on the position of the applied loads.

Figure 18 – Deflection vs. slab skew angle at the mid-span for varying bend-to-twist ratio.

The deflection at the mid-span for skewed slabs was plotted against the slab skew angle for varying bend-to-twist ratios and is shown in Fig. 18. The result of the study illustrates that mid-span deflections increase for an increasing bend-to-twist ratio and this is pronounced for higher bend-to-twist ratios at higher 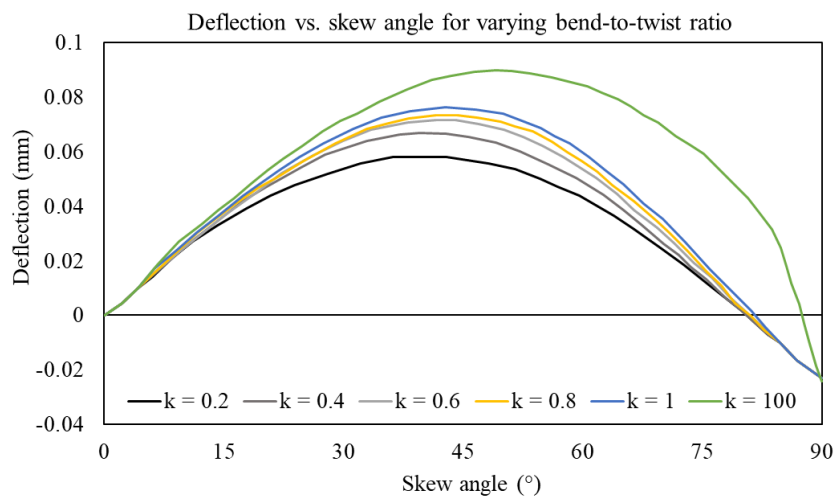skew angles. For a ratio of $k = 0.2$, the peak mid-span deflection is at a skew angle of 45°, whereas at a ratio of $k = 100$, the peak deflection is at approximately 55°. Moreover, the model highlights that mid-span deflections beyond a slab skew of 75° are not accurate and this is evident in Fig. 18. This is due to the negative deflections for the varying bend-to-twist ratios.

4.1.2. *Yield line theory for estimating mid-span collapse load*

To predict the failure load to the skewed slab problem, a yield line analysis is applied for which the geometry of the problem is shown in Figs. 19 (a) and (b). The solution to the yield line method has been used in previous research in predicting the collapse load at the ultimate state limit for skewed slabs [29].
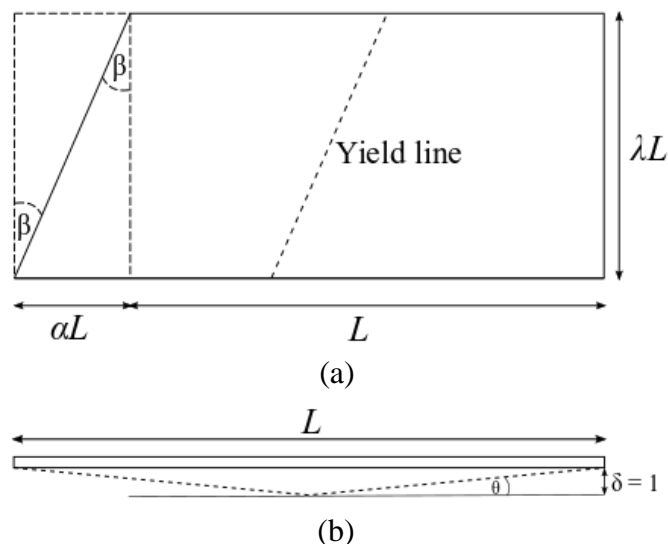

Figure 19 – Schematic for the yield line analysis on skewed slabs: a) top view; and b) side view.

The length of the shorter slab edge L is used in conjunction with coefficients λ and α as scalar parameters to calculate the magnitude of the width and segmented skewed length of the slab, respectively, and is illustrated in Fig. 19 (a). The expression for the external work done to the slab by a virtual unit load is:

$$\sum W\theta = w\delta dxdy = \frac{1}{2}w\delta\left(\lambda L^2 + \frac{1}{2}\lambda L^2\right) \tag{14}$$

The internal work done about the yield line in Fig. 19 (a) is defined as:

$$\sum M\theta = ML\theta = M_x^+ \lambda L\left(\frac{8}{2L+\alpha L}\right) + 2M_x^- \lambda L\left(\frac{2}{L}\right) \tag{15}$$

where M_x^+ and M_x^- are the positive and negative bending moments along the yield line about the x-axis. Equating the external and internal work done, the following expression is found:

$$\sum W\theta = \sum M\theta \tag{16}$$

$$\frac{1}{2}w\delta\left(\lambda L^2 + \frac{1}{2}\lambda L^2\right) = M_x^+ \lambda L\left(\frac{8}{2L+\alpha L}\right) + 2M_x^- \lambda L\left(\frac{2}{L}\right) \tag{17}$$

which when simplified, results in:

$$w = \frac{4}{l^2}\left[\frac{8M_x^+ + 8M_x^- + 4\alpha M_x^-}{(2+\alpha^2)}\right] \tag{18}$$

where w is the collapse load. Owing to the placement of the reinforcement at the centroid of the slab section, the section is isotropic and thus moments acting in both directions are equal. Therefore, Eq. (18) reduces to:

$$w = \frac{16}{l^2}\left[\frac{M_{cap}(4+\alpha)}{(2+\alpha^2)}\right] \tag{19}$$

where M_{cap} represents the moment corresponding to the collapse load. The moment capacity of the slab section at the ultimate state is determined through a mechanistic moment-rotation approach [30]. Predictions for the collapse load for the skewed slabs with comparisons to the experimental results are shown in Table 3.

Specimen	Collapse Load (kN)		Error (%)
	Experimental	Theoretical	
Skewed 25°	42.6	34.8	22.4
Skewed 45°	35.4	43.4	18.4

Table 3 – Comparison of experimental and theoretical results for the collapse load of 25° and 45° skewed UHPFRC slabs.

Collapse load estimates made by the yield line analysis are close to the experimental results with prediction errors between 18% to 23%. A possible source of error is the orientation of the plastic hinge. The assumption made is that the plastic hinge forms parallel to the skew angle, however the yield line angle may differ from the assumption made in Fig. 19 (a). The cracking shown in Fig. 10 (b) indicate a mixed mode of vertical and angular cracking which would lead to a longer plastic hinge lengths and subsequently collapse loads. The results of the error analysis show that the developed model based on the collapse mechanism can be applied to UHPFRC curved slabs.

4.2. Curved UHPFRC slabs

4.2.1. *Castigliano's Second Theorem for estimating mid-span deflections*

Similar to the skewed slab problem, the curved slabs are statically indeterminate due to the boundary conditions and geometry, however an added complexity is the out-of-plane curvature of the slab which results in an eccentricity and consequently torsional moment applied at the centre of the slab. Therefore, a robust approach is required to solve the problem. An application of Castigliano's Second Theorem (CST) [38] developed for horizontally curved bridge decks developed by Fatemi et al. [39] is modified for a radial coordinate system which is shown in Fig. 20.
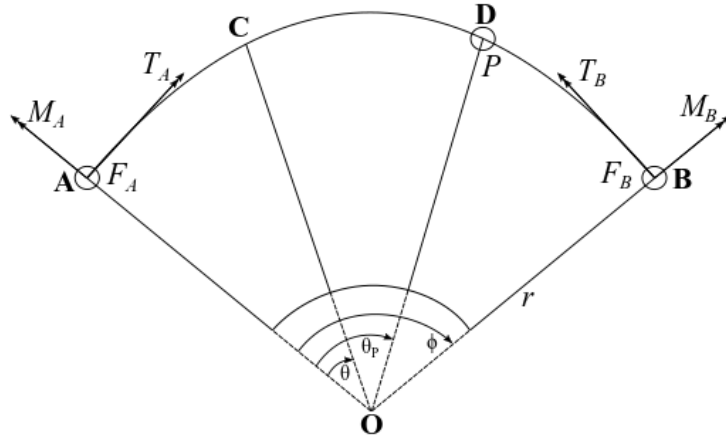
Figure 20 – Schematic diagram for the application of Castigliano's Second Theorem (CST) on curved slabs.

It is assumed that the slab section remains uniform, the slab thickness is small in comparison to the slab curvature radius r, and the supports are lumped at A and B for which there are reaction forces and bending/torsional moments (M_A, T_A, F_A, M_B, T_B, F_B) resulting from the applied point load P located at B at an angle θ_P and distance r. A radial coordinate system is applied from the origin O, and an arbitrary location C with angle θ is used to develop expressions for the bending and torsional moments:

For $0 \leq \theta \leq \theta_P$:

$$M_\theta = M_A \cos\theta + T_A \sin\theta - F_A r \sin\theta \tag{20}$$

$$T_\theta = -M_A \sin\theta + T_A \cos\theta + F_A r(1 - \cos\theta) \tag{21}$$

For $\theta_P \leq \theta \leq \phi$:

$$M_\theta = M_A \cos\theta + T_A \sin\theta - F_A r \sin\theta + Pr \sin(\theta - \theta_P) \tag{22}$$

$$T_\theta = -M_A \sin\theta + T_A \cos\theta + F_A r(1 - \cos\theta) - Pr\,(1 - \cos(\theta - \theta_P)) \tag{23}$$

The expression for the total internal strain energy is:

$$U = \int \frac{M_\theta^2}{2EI} r\, d\theta + \int \frac{T_\theta^2}{2GJ} r\, d\theta \tag{24}$$

The fixed support conditions result in zero displacements for rotations and deflection which gives rise to the following condition:

$$\frac{\partial U}{\partial M_A} = \frac{\partial U}{\partial T_A} = \frac{\partial U}{\partial F_A} = 0 \tag{25}$$

where ω_A is the bending rotation, φ_A is the torsional rotation, and Δ_A is the vertical displacement. Using Eq. (24) in conjunction with Eq. (25), the three conditions can be solved by the implementation of CST and give rise to the following equations for each of the three conditions:

$$\frac{r}{EI}\left[M_A\left(\frac{\sin^2\phi}{2}(1-m)\right) + T_A\left(\frac{\phi}{2}(1+m) - \frac{\sin 2\phi}{4}(1-m)\right) + \right.$$

$$\left. F_A r\left(\frac{\sin^2\phi}{2}(m-1) + m\left(\cos\phi - \frac{1}{2}\right)\right)\right] = \frac{Pr^2}{EI}\left[\frac{\phi}{2}\sin\theta_P(1+m) + \frac{1}{4}\cos(\phi - \right.$$

$$\left. \theta_P)(1-m) + m\cos\phi\right] \tag{26}$$

$$\frac{r}{EI}\left[M_A\left(\frac{\sin^2\phi}{2}(1-m)\right) + T_A\left(\frac{\phi}{2}(1+m) - \frac{\sin 2\phi}{4}(1-m)\right) + F_A r\left(\frac{\sin^2\phi}{2}(1-\right.\right.$$

$$\left.\left. m) + \frac{\phi}{2}(1+m) + m\sin\phi\right)\right] = \frac{Pr^2}{EI}[(m-1)\sin(\theta_P - 2\phi) - 2\phi\cos\theta_P(1+m) + $$

$$4\sin\phi] \tag{27}$$

$$\frac{r^2}{EI}\left[M_A\left(\frac{\sin^2\phi}{2}(k-1) + k\left(\cos\phi - \frac{1}{2}\right)\right) + T_A\left(\frac{\sin 2\phi}{4}(1-k) - \frac{\phi}{2}(1+k) + \right.\right.$$

$$\left.\left. k\sin\phi\right) + F_A r\left(\frac{\phi}{2}(1+3k) - (1-k)\frac{\sin 2\phi}{4} - 2k\sin\phi\right)\right] = \frac{Pr^3}{EI}\left[\frac{1}{4}\sin(\theta_P - \right.$$

$$\left. 2\phi)(1-k) + \frac{1}{2}\phi\cos\theta_P(1+k) + k\sin(\theta_P - \phi) + k(\phi - \sin\phi)\right] \tag{28}$$

where k is the bend-to-twist ratio (EI/GJ). Eqs. (26) – (28) are simplified to:

$$a_1 M_A + b_1 T_A + c_1 F_a r = d_1 Pr \tag{29}$$

$$a_2 M_A + b_2 T_A + c_2 F_a r = d_2 Pr \tag{30}$$

$$a_3 M_A + b_3 T_A + c_3 F_a r = d_3 Pr \tag{31}$$

Eqs. (29) – (31) are solved simultaneously to obtain M_A, T_A and F_A. The coefficients and expressions for M_A, T_A and F_A are found in Appendix A (Eqs. (A.1) – (A.15)). The moment area method provides a generic solution in solving for the deflections of the curved slabs, where:

$$EI\Delta_\theta = \int_0^\theta M_\theta r \sin\left(\frac{\phi}{2} - \theta\right) ds + \int_0^\theta T_\theta r \left(1 - \cos\left(\frac{\phi}{2} - \theta\right)\right) ds \quad (32)$$

and for the mid-span ($\theta = \varphi/2$ and $ds = rd\theta$), it solves to become:

$$\Delta_{mid-span} = \frac{r^2}{2EI}\left[\frac{M_A}{4}(1 - \cos\phi) + \frac{1}{4}(T_A - F_A r)(\phi - \sin\phi)\right] +$$

$$\frac{r}{2EI}\left[M_A\left(\cos\left(\frac{\phi}{2}\right) - 1\right) + T_A \sin\left(\frac{\phi}{2}\right) - F_A r\left(\sin\left(\frac{\phi}{2}\right) - \frac{\phi}{2}\right) - \cos\left(\frac{\phi}{2}\right)\left(-\frac{M_A}{4}(1 - \right.\right.$$

$$\left.\cos\phi) + \frac{(T_A - F_A r)(\phi - \sin\phi)}{4} + \frac{F_A r\phi}{2}\right) - \sin\left(\frac{\phi}{2}\right)\left(-\frac{M_A}{4}(\phi - \sin\phi) + \right.$$

$$\left.\left.\frac{(T_A - F_A r)(1 - \cos\phi)}{4} + \frac{F_A r}{2}\left(\cos\left(\frac{\phi}{2}\right) - 1\right)\right)\right] \quad (33)$$

Mid-span deflections for the curved UHPFRC slabs for differing load placements are generated using Eq. (33) and compared to the deflections found experimentally, shown in Table 4.

Specimen	Load placement	Mid-span deflection (mm)		Error (%)
		Experimental	Theoretical	
Curved 60°	E	2.04	2.27	10.1
	C	0.79	0.85	7.06
Curved 90°	E	5.61	5.79	3.11
	C	1.67	1.75	4.57

Table 4 – Comparison of experimental and theoretical results for the mid-span deflection of 60° and 90° curved UHPFRC slabs for differing load placement.

The closed-form solutions provide sufficient predictions to the mid-span deflection for the 60° and 90° curved slabs with percentage errors lying below 10.1%. The prediction errors are more accurate for the higher curvature, with those errors lying below 4.6%. The source of prediction

error between theoretical and experimental results can be primarily attributed to the non-homogeneity of UHPFRC whereas the model assumed homogenous material properties. Additionally, reaction forces are calculated for loading at the mid-span and compared to reaction forces found experimentally and are shown in Table 5.

Specimen	Corner	Reaction Forces (kN)		Error (%)
		Experimental	Theoretical	
Curved 60°	1	12.58	13.60	7.50
	2	13.71	13.60	0.81
	3	15.81	16.90	6.45
	4	16.43	16.90	2.78
Curved 90°	1	24.07	23.40	2.86
	2	25.42	23.40	8.63
	3	20.12	18.60	8.17
	4	20.87	18.60	12.2

Table 5 – Comparison of experimental and theoretical results for the reaction forces of 60° and 90° curved UHPFRC slabs.

The closed-form solutions provide sufficient predictions to the reaction forces for the 60° and 90° curved slabs with percentage errors lying below 7.5% for the 60° curved slab and 12.2% for the 90° curved slab. The results of the error analysis show that the developed model based on CST can be applied to curved slabs.

A parametric study was performed to observe the variation of bending moment and shear force for varying location curvature ratio (ϕ/θ) using the developed expressions (Eqs. (20) – (23)) for curved slabs subjected to unit loads along the slab centreline, with the results of the study shown in Figs. 21 (a) – (c).
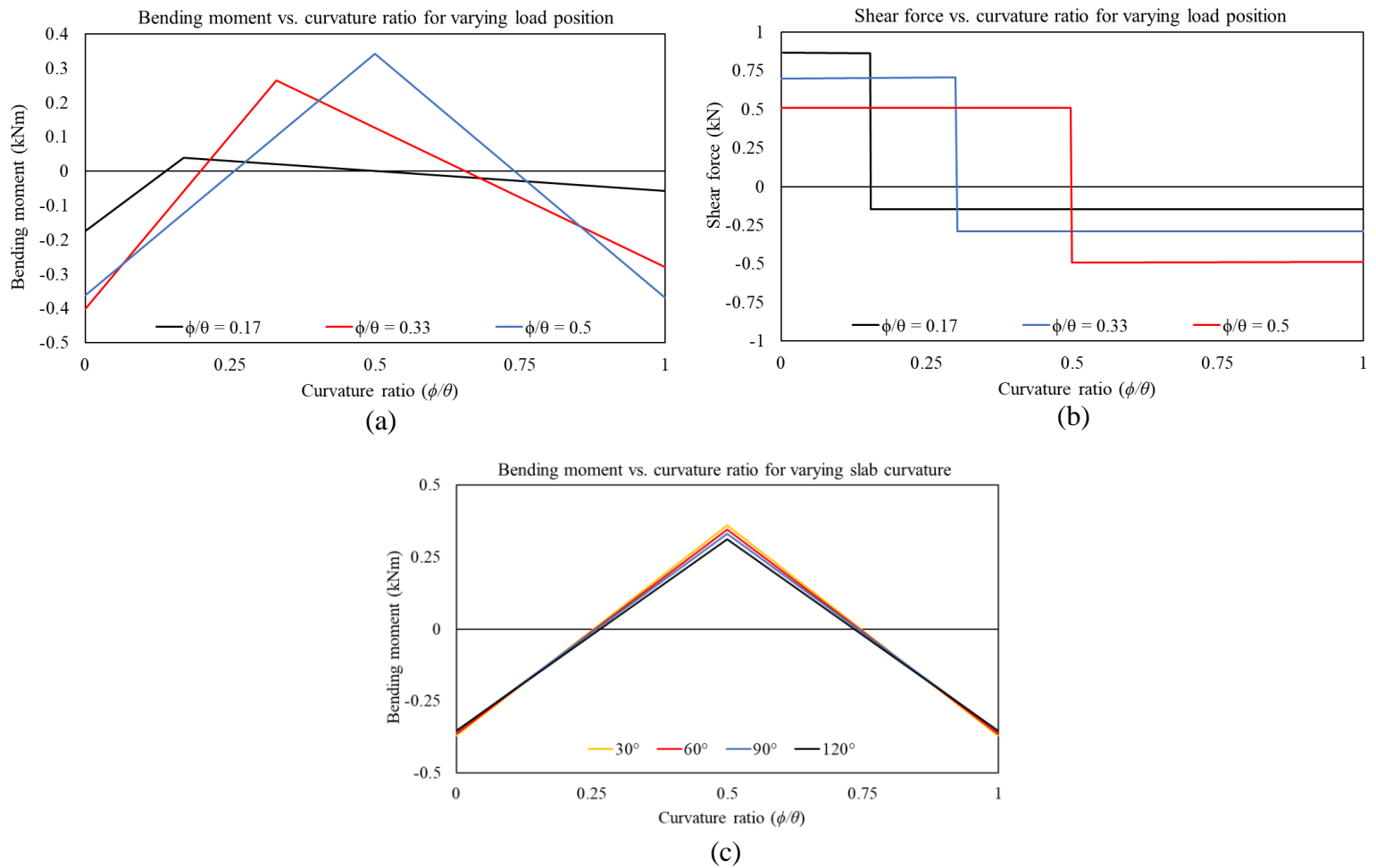
Figure 21 – Results of parametric study performed on analytical curved slab model: (a) bending moment vs. curvature ratio for varying load position; (b) shear force vs. curvature ratio for varying load position; and (c) bending moment vs. curvature ratio for varying slab curvature.

The variation in bending moment and shear distributions along the slab centreline (Fig. 21 (a)) shows that the largest magnitude of moment distribution along the curved slab centreline is for loads at the mid-span, and that the bending moment magnitude decreases the further the load is placed away from the mid-span. The shear force distribution shown Fig. 21 (b) indicates the distribution is similar to a regular slab and that curvature has minimal effect on this. Lastly, a

179

study on curvature for bending moment along the centreline (Fig. 21 (c)) shows minimal variation in bending moment magnitude at the supports, however the mid-span moment variation is more evident for varying curvatures.

5. FINITE-ELEMENT ANALYSIS

The analysis of the skewed and curved slabs using the developed closed form solutions is comparatively simple in predicting the response of the slabs however many simplifications are made in its development, and additionally the analytical techniques are not able to generate a full-range load-deflection response. A detailed finite-element analysis using a finite-element code (ABAQUS) is performed to predict the behaviour of the slabs.

5.1.   Model generation

To replicate the experimental loading setup and predict the structural behaviour of the slabs, the clamping and loading plates, in addition to the slabs, are incorporated into the FE model. All parts other than the reinforcement are modelled by 8-noded solid brick elements (C3D8) but with differing material models. To replicate the interaction between the loading and clamping plates with the slabs, a surface-to-surface hard contact interaction is implemented with a frictional factor of 0.1. The mesh reinforcement is modelled by 3D truss elements (T3D2) and are embedded and tied within the slabs. A convergence study provides the optimum element size of 20 mm for all parts. To replicate the boundary conditions in the experimental setup, the clamping plates and slabs are connected by support bolts and fixed end conditions are applied to the bottom clamping plates. The loading and clamping plates, support bolts and embedded steel reinforcement are modelled using an elastic material model, whereas the slabs are modelled using the concrete damage plasticity (CDP) model, which incorporates stiffness degradation using damage variables coupled with plastic deformations. The CDP model is the

modified form [40] of the initial model proposed by Lubliner et al. [41] by adjusting the yield function and utilising the fracture energy cracking criterion of Hillerborg et al. [42]. Operation of the CDP model requires certain parameters: Poisson's ratio (v), dilation angle (ψ) for directing plastic strain increment direction, eccentricity (ε) for controlling the deviation of the plastic potential geometry, biaxial stress ratio ($\sigma_{bsr} = \sigma_{b0}/\sigma_{c0}$), shape factor ($K_c$) for defining the failure surface geometry of the deviatoric plane, and the viscosity parameter (μ) for convergence minimisation. The values of these key parameters (Poisson's ratio an exception) are typically found from uniaxial, biaxial and triaxial tests on concrete specimens. A study conducted by Jankowiak & Lodygowski [43] identified these parameters for UHPC, and further research by Shafieifar et al. [44] successfully calibrated the parameters for the modelling of UHPFRC. The calibrated values for the current study are: $\varepsilon = 0.1$, $\mu = 0.005$, $K_c = 0.67$, $v = 0.235$, $\psi = 35°$, and $\sigma_{bsr} = 1.16$. The uniaxial stress-strain relationships for tension and compression found from testing of the UHPFRC (Figs. 6 and 7 (a)) are used by the CDP model for the finite-element simulation.

5.2.   Results

5.2.1. *Comparison of experimental and numerical results*

The results of the numerical results are summarised in Table 6 and the finite-element modelled load-deflection responses are shown in Figs. 22 (a) – (d).

Specimen	Peak load (kN)		Error (%)	Deflection at peak load (mm)		Error (%)
	Experimental	Numerical		Experimental	Numerical	
Skewed 25°	35.0	35.1	0.3	21.2	20.1	5.5
Skewed 45°	43.5	45.1	3.5	17.9	19.8	9.6
Curved 60°	34.2	35.2	2.8	14.8	13.1	13.0
Curved 90°	24.2	25.0	3.2	20.5	17.9	14.5

Table 6 – Comparison of experimental and numerical results for the peak loads and deflections at the peak loads for curved and skewed UHPFRC slabs.
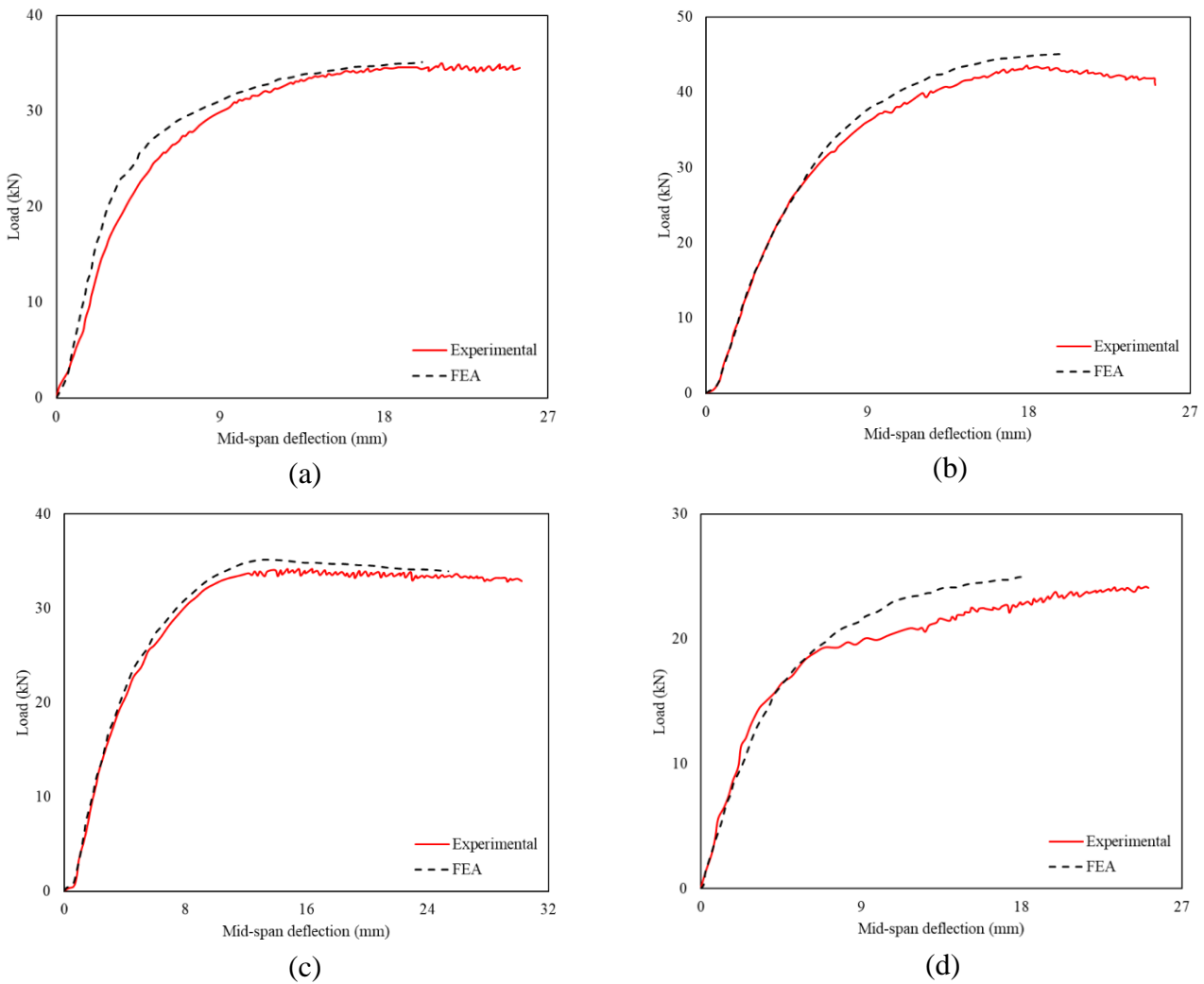

(a)

(b)

(c)

(d)

Figure 22 – Load vs. mid-span deflection relationships for: a) 25° skewed slab; b) 45° skewed slab; c) 60° curved slab; and d) 90° curved slab.

It can be seen from Figs. 22 (a) and (b) that the results of the finite element model are very accurate in predicting both the elastic and post-peak regions of loading of the UHPFRC skewed slabs and this is reinforced by Table 6 when comparing the peak loads, deflections at the peak loads and the error percentages of both skewed slab specimens. The failure criterion of the four slabs was found to be controlled by tensile damage modelled by the concrete damage plasticity model at the mid-span of the slabs. This is agreeable to the observations of the experimental program in all four slabs failing at the mid-span due to large tensile damage leading to slab collapse. The larger error percentage for deflections associated to the peak load is owed to the deflections at the peak loads being a pre-peak value. Fig. 22 (c) displays the high accuracy of the finite element model in predicting the load-deflection behaviour of the 60° curved slab specimen, with the model very closely matching the experimental results. However, the model was less accurate for modelling the structural behaviour of the 90° curved slab specimen (Fig. 22 (d)). This can be attributed to the random orientation and dispersal of steel fibres in the specimen body. This assumption can lead to non-homogeneity and result in unexpected loss of strength which would skew the experimental results.

6. CONCLUSIONS

The study in this paper presents the experimental and analytical investigation conducted on the assessment of UHPFRC reinforced curved and skewed slabs under concentrated loads. Based on the results obtained in the study, the following conclusions can be made:

(1) The asymmetrical slab skewness has a significant effect on the support reactions. An increase in skewness leads to a decrease in reaction force magnitude at the corner opposing the obtuse corner. For loads applied adjacent to the mid-span centreline, an increase in skewness results in little to no reaction force at the support opposing the acute corner.

(2) The curvature of a horizontally curved slab has a significant effect on the support reactions. An increase in curvature leads to an increase in reaction force magnitude at the inner radii supports, whilst load applied off-set to the mid-span centreline results in a reduction of reaction force magnitude at the outer radii supports for an increasing curvature.

(3) The load-deflection relationship of an asymmetrically skewed slab loaded at the mid-span is considerably affected by the skewness of the slab. An increase in skewness leads to an increase in load capacity (25% increase between 25° and 45° skew) with a larger mid-span deflection and hence ductility. The increase in skew angle shortens the load path between the two support edges which leads to a shorter lever arm. However, additional skew angles beyond 45° is recommended for further investigation to determine the critical angle range for asymmetrically skewed fixed-end slabs.

(4) The load-deflection relationship of a horizontally curved slab loaded at the mid-span is substantially affected by the curvature of the slab. A decrease in curvature leads to an increase in load capacity (40% increase between 60° and 90° curvature). The increase in curvature leads to an increasing load eccentricity between the load point and supports.

(5) The closed-form analytical solutions for fixed-end indeterminate curved and skew slabs on energy-based approaches (virtual work, yield line theory, and Castigliano's second theorem) to determine failure loads, deflections, and distributions for bending moments, shear forces, reaction forces and torsional moments. Finite-element analysis is used to model the full-range behaviour of the slabs, implementing a concrete damage plasticity model using calibrated parameters from existing studies.

(6) Predictions made by the closed-form solutions and finite-element model highlight an adequate comparison to the experimental findings and appropriate in predicting the behaviour of curved and asymmetrically skewed slabs. Prediction errors found between

the analytical models and experimental findings are affected by the non-homogeneity of the material due to the uneven fibre distribution in the slab specimens.

(7) A parametric study was performed on the closed-form analytical procedures to observe the effects of skew angle and curvature angle on slab behaviour for various material and mechanical alterations. The major findings were determining the maximum torsional moment at the midspan for an asymmetrically skewed slab occurs at a skew angle of 55° and mid-span deflections are larger for an increasing bend-to-twist ratios which is magnified further for an increasing skew angle. There is minimal variation in bending moment magnitude at the supports and mid-span for increasing curvature for horizontally curved slabs. An experimental investigation for a large range of skew angles is recommended to support the findings of the parametric study for asymmetrically skewed fixed-end slabs.

APPENDIX

The coefficients used to solve the simultaneous equations (Eqs. (29) – (31)) are:

$$a_1 = \frac{\phi}{2}(1 + m) + \frac{\sin 2\phi}{4}(1 - m) \tag{A.1}$$

$$b_1 = \frac{\sin^2 \phi}{2}(1 - m) \tag{A.2}$$

$$c_1 = \frac{\sin^2 \phi}{2}(m - 1) + m(\cos \phi - 1) \tag{A.3}$$

$$d_1 = \frac{\phi}{2}\sin\theta_P\,(1+m) + \frac{1}{4}\cos(\phi-\theta_P)\,(1-m) + m\cos\phi \qquad (A.4)$$

$$a_2 = b_1 \qquad (A.5)$$

$$b_2 = \frac{\phi}{2}(1+m) - \frac{\sin 2\phi}{4}(1-m) \qquad (A.6)$$

$$c_2 = \frac{\sin 2\phi}{4}(1-m) - \frac{\phi}{2}(1+m) + m\sin\phi \qquad (A.7)$$

$$d_2 = \sin(\theta_P - 2\phi)\,(m-1) - 2\phi\cos\theta_P\,(1+m) + 4\sin\phi \qquad (A.8)$$

$$a_3 = c_1 \qquad (A.9)$$

$$b_3 = c_2 \qquad (A.10)$$

$$c_3 = \frac{\phi}{2}(1+m) - \frac{\sin 2\phi}{4}(1-m) - 2m\sin\phi \qquad (A.11)$$

$$d_3 = \frac{1}{4}\sin(\theta_P - 2\phi)\,(1-m) + \frac{\phi}{2}\cos\theta_P\,(1+m) + m\sin(\theta_P - \phi) + m(\phi - $$

$$\sin\phi) \qquad (A.12)$$

Eqs. (A.1) – (A.12) are incorporated into Eqs. (28) – (30) to provide explicit closed-form solutions for M_a, T_a and F_a:

$$M_a = rP\,\frac{(b_2 d_1 - a_1 d_2)(c_1 c_2 - b_1 c_3) - (c_2 d_1 - b_1 d_3)(b_2 c_1 - a_1 c_2)}{(a_1 b_2 - a_1 b_1)(c_1 c_2 - b_1 c_3) - (a_1 c_2 - b_1 c_1)(b_2 c_1 - a_1 c_2)} \qquad (A.13)$$

$$T_a = rP\,\frac{(b_1 d_1 - a_1 d_2)(c_1^2 - a_1 c_3) - (c_1 d_1 - a_1 d_3)(b_1 c_1 - a_1 c_2)}{(b_1^2 - a_1 b_2)(c_1^2 - a_1 c_3) - (b_1 c_1 - a_1 c_1)(b_1 c_1 - a_1 c_2)} \qquad (A.14)$$

$$F_a = P\,\frac{(b_1 d_1 - a_1 d_2)(b_1 c_1 - a_1 c_2) - (c_1 d_1 - a_1 d_3)(b_1^2 - a_1 b_2)}{(b_1 c_1 - a_1 c_1)(b_1 c_1 - a_1 c_2) - (c_1^2 - a_1 c_3)(b_1^2 - a_1 b_2)} \qquad (A.15)$$

REFERENCES

[1] Gupta T, Kumar M. Structural Response of Concrete Skew Box-Girder Bridges. International Journal of Bridge Engineering. 2017;5(1):37-59.

[2] Deepak C, Sabeena M. Effect of skew angle on uplift and deflection of RCC skew slab. International Journal of Research in Engineering and Technology. 2015;4(05).

[3] Shea GH, Earthquake Engineering Research I. Costa Rica earthquake of April 22, 1991 : reconnaissance report. Oakland, CA: Earthquake Engineering Research Institute; 1991.

[4] Hall JF, Earthquake Engineering Research I. Northridge earthquake of January 17, 1994 : reconnaissance report. vol. 1 vol. 1. Oakland, Calif.: Earthquake Engineering Research Institute; 1995.

[5] Kawashima K, Unjoh S, Hoshikuma J, Kosa K. Damage of transportation facility due to 2010 Chile earthquake. Bridge Team Dispatched by Japan Society of Civil Engineers. 2010.

[6] Wilson T, Mahmoud H, Chen S. Seismic performance of skewed and curved reinforced concrete bridges in mountainous states. Engineering Structures. 2014;70:158-67.

[7] Maleki S. Deck modeling for seismic analysis of skewed slab-girder bridges. Engineering Structures. 2002;24(10):1315-26.

[8] Chun B-J. Skewed bridge behaviors: experimental, analytical, and numerical analysis. 2010.

[9] Okumus P, Oliva MG, Arancibia MD. Design and Performance of Highly Skewed Deck Girder Bridges. 2018.

[10] Dhar A, Mazumder M, Karmakar MCS. Effect of skew angle on longitudinal girder (support shear, moment, torsion) and deck slab of an IRC skew bridge. The Indian Concrete Journal. 2013;1(13):46-52.

[11] Menassa C, Mabsout M, Tarhini K, Frederick G. Influence of skew angle on reinforced concrete slab bridges. Journal of Bridge Engineering. 2007;12(2):205-14.

[12] Nouri G, Ahmadi Z. Influence of skew angle on continuous composite girder bridge. Journal of Bridge Engineering. 2012;17(4):617-23.

[13] Association CS. Canadian Highway Bridge Design Code. Toronto, ON, Canada 2010. p. 800.

[14] AASHTO. Guide Specification for Horizontally Curved Highway Bridges. Washington, DC: American Association of State Highway and Transportation Officials; 2003. p. 392.

[15] Zhang S, Lyons L. A thin-walled box beam finite element for curved bridge analysis. Computers & structures. 1984;18(6):1035-46.

[16] NACE International, Highway and Bridges. https://www.nace.org/resources/industries-nace-serves/highways-bridges, 2020 (accessed 24 October 2021).

[17] Emmenegger LP. Extending the Lifespan of Reinforced Concrete Bridge Decks: Historical Analysis, Modeling, and Improved Contracting: Georgia Institute of Technology; 2020.

[18] Khaksefidi S, Ghalehnovi M, De Brito J. Bond behaviour of high-strength steel rebars in normal (NSC) and ultra-high performance concrete (UHPC). Journal of Building Engineering. 2021;33:101592.

[19] Feng Y, Qi J, Wang J, Liu J, Liu J. Flexural behavior of the innovative CA-UHPC slabs with high and low reinforcement ratios. Advances in Materials Science and Engineering. 2019; 2019.

[20] Zhu Y, Zhang Y, Hussein HH, Chen G. Flexural strengthening of reinforced concrete beams or slabs using ultra-high performance concrete (UHPC): A state of the art review. Engineering Structures. 2020; 205:110035.

[21] Wiemer N, Wetzel A, Schleiting M, Krooß P, Vollmer M, Niendorf T, et al. Effect of fibre material and fibre roughness on the pullout behaviour of metallic micro fibres embedded in UHPC. Materials. 2020;13(14):3128.

[22] Bae Y, Pyo S. Ultra high performance concrete (UHPC) sleeper: Structural design and performance. Engineering Structures. 2020; 210:110374.

[23] Murugan M SR, Rajesh. J. Review of Ultra-High Performance Concrete and Cost Impact of UHPC in Durability Aspects. NTERNATIONAL JOURNAL OF ENGINEERING RESEARCH & TECHNOLOGY (IJERT). 2020; 9(3).

[24] Sobuz H, Visintin P, Ali MM, Singh M, Griffith M, Sheikh A. Manufacturing ultra-high performance concrete utilising conventional materials and production methods. Construction and Building materials. 2016;111:251-61.

[25] Xie T, Visintin P. A unified approach for mix design of concrete containing supplementary cementitious materials based on reactivity moduli. Journal of cleaner production. 2018;203:68-82.

[26] Dong Y. Performance assessment and design of ultra-high performance concrete (UHPC) structures incorporating life-cycle cost and environmental impacts. Construction and Building Materials. 2018;167:414-25.

[27] Behloul M, Lee K. Ductal® seonyu footbridge. Structural Concrete. 2003;4(4):195-201.

[28] Brühwiler E. UHPFRC technology to enhance the performance of existing concrete bridges. Structure and Infrastructure Engineering. 2020;16(1):94-105.

[29] Xie T, Ali MM, Visintin P. Behaviour and analysis of ultra high performance fibre reinforced concrete (UHPFRC) skew slabs. Engineering Structures. 2019;199:109588.

[30] Visintin P, Oehlers D, Wu C, Haskett M. A mechanics solution for hinges in RC beams with multiple cracks. Engineering Structures. 2012;36:61-9.

[31] Singh M, Sheikh A, Ali MM, Visintin P, Griffith M. Experimental and numerical study of the flexural behaviour of ultra-high performance fibre reinforced concrete beams. Construction and Building Materials. 2017;138:12-25.

[32] Bouguerra K, Ahmed E, El-Gamal S, Benmokrane B. Testing of full-scale concrete bridge deck slabs reinforced with fiber-reinforced polymer (FRP) bars. Construction and building materials. 2011;25(10):3956-65.

[33] Australia S. AS 1012.17-1997 - Methods of testing concrete Determination of the static chord modulus of elasticity and Poisson's ratio of concrete specimens (Reconfirmed 2014). Standards Australia. p. 13.

[34] Redaelli D. Testing of reinforced high performance fibre concrete members in tension. Proceedings of the 6th Int Ph D Symposium in Civil Engineering, Zurich 2006: Proceedings of the 6th Int. Ph. D. Symposium in Civil Engineering, Zurich 2006; 2006. p. 8.

[35] Moreno D, Trono W, Jen G, Ostertag C, Billington S. Tension-stiffening in reinforced high performance fiber-reinforced cement-based composites under direct tension. High Performance Fiber Reinforced Cement Composites 6: Springer; 2012. p. 263-70.

[36] Visintin P, Sturm A, Mohamed Ali M, Oehlers D. Blending macro-and micro-fibres to enhance the serviceability behaviour of UHPFRC. Australian Journal of Civil Engineering. 2018;16(2):106-21.

[37] Sindhu B, Ashwin K, Dattatreya J, SV D. Effect of skew angle on static behaviour of reinforced concrete slab bridge decks. International Journal of Research in Engineering and Technology. 2013;2(1):50-8.

[38] Timoshenko S. History of strength of materials: with a brief account of the history of theory of elasticity and theory of structures: Courier Corporation; 1983.

[39] Fatemi S, Sheikh A, Ali MM. Development and application of an analytical model for horizontally curved bridge decks. Advances in Structural Engineering. 2015;18(1):107-17.

[40] Lee J, Fenves GL. Plastic-damage model for cyclic loading of concrete structures. Journal of engineering mechanics. 1998;124(8):892-900.

[41] Lubliner J, Oliver J, Oller S, Oñate E. A plastic-damage model for concrete. International Journal of Solids and Structures. 1989;25(3):299-326.

[42] Hillerborg A, Modéer M, Petersson P-E. Analysis of crack formation and crack growth in concrete by means of fracture mechanics and finite elements. Cement and concrete research. 1976;6(6):773-81.

[43] Jankowiak T, Lodygowski T. Identification of parameters of concrete damage plasticity constitutive model. Foundations of civil and environmental engineering. 2005;6(1):53-69.

[44] Shafieifar M, Farzad M, Azizinamini A. Experimental and numerical study on mechanical properties of Ultra High Performance Concrete (UHPC). Construction and Building Materials. 2017;156:402-11.

THIS PAGE HAS BEEN LEFT INTENTIONALLY BLANK

CHAPTER 5

Concluding Remarks

In this thesis, new and innovative ultra-high performance fibre-reinforced concrete (UHPFRC) composite panels and slabs were conceptualised, developed, and produced. The theory behind the box girder and bubble deck systems were applied to develop pre-cast composite UHPFRC wind-resistant panels. Furthermore, the benefits of UHPFRC were used to develop asymmetrically skewed and curved slabs suitable for floor slabs and bridge decks. Numerical and analytical modelling were performed to predict the behaviour of the elements in the elastic and inelastic ranges, and to assess their feasibility as structurally proficient members.

Inspired by the box girder and bubble deck systems, new forms of pre-cast composite UHPFRC panels were developed in an experimental program. Six panel specimens were tested under three-point flexure, of which three were UHPC-FRP bubble deck sandwich panels and three were box-celled UHPC-steel panels. The elementary sandwich theory (EST) and advanced sandwich theory (AST) were modified to accommodate for the sandwich panels at the serviceability limit state, whereas a segmental sectional analysis was applied to predict the box-cell panel behaviour at the serviceability limit state. Finite-element analyses were performed to the box-cell panels predict the full-range structural performance. The analytical and numerical models were successful in predicting the elastic and inelastic behaviour of the box-cell and sandwich panels when compared to the experimental findings, which found the box-cell composite panel as the most effective of the two panel systems.

The box-cell panel system was further explored as a wind-resistant structural panel in an experimental study. Six box-celled UHPFRC composite panels with were fabricated and

subjected to three-point flexure and a thorough assessment of their flexural and deflection capacities by current code provisions were performed to assess the suitability of the panel system as a wind-resistant structural panel. Load and deflection criteria were found to be within the elastic region for both hogging and sagging moments, satisfying the requirements of current code provisions. The panels were found to be efficient as a main wind force resistant system (MWFRS), and the most effective section arrangement based on the code provision criteria, failure behaviour, and strength-to-weight ratio was with the addition of helically ribbed longitudinal GFRP reinforcement.

The effectiveness of the helically ribbed GFRP to the composite panels highlighted the need to critically evaluate the performance of the reinforcement when embedded in UHPFRC. An experimental program was performed to evaluate its bond-slip behaviour within UHPFRC. Seven helically ribbed GFRP reinforcement specimens and seven high-strength steel reinforcement specimens were cast in a UHPFRC block and tested under pull-out conditions. The local bond-slip relationships of the GFRP and steel specimens were experimentally evaluated, and existing theoretical models were used to develop a new multi-variable bond-slip model specifically for the GFRP used in the study. The newly established model was compared to the steel reinforcement tested in the current study and largely agreed in the bond-slip behaviour, with peak stresses, plateau widths and both softening and failure slopes closely matching for the matching reinforcement placement. Importantly, the parametric study found an increase in bond strengths at peak and failure for an increasing concrete compressive strength. Moreover, minimal variation in peak and failure stresses were predicted for low concrete cover conditions and an increase in plateau widths for increasing bar diameters, indicating negligible consequence in increasing the compressive strength of concrete for reinforcement in low cover conditions.

Lastly, the feasibility of UHPFRC as a material used in the fabrication of curved and skewed UHPFRC slabs was investigated. Four UHPFRC composite slabs, of which two were asymmetrically skewed with skew angles of 25° and 45°, and two horizontally curved with curvature angles of 60° and 90°, were fabricated and subjected to concentrated loads at designated locations along the slab. Analytical solutions based on the method of virtual work and Castigliano's second theorem were determined to predict the structural behaviour of the curved slabs within the linear elastic state. Additionally, closed-form solutions were developed based on yield-line theory in tandem with a mechanics-based moment-rotation model to predict deflections at the ultimate state, and a thorough finite-element analysis applying non-linear material and damage modelling is accomplished to obtain the full-range behaviour of the slabs. A parametric study was performed to assess the effect of skew and curvature angle on deflection, shear, bending and torsion along the slab lengths and found the maximum torsional moment at the midspan for an asymmetrically skewed slab occurred at a skew angle of 55° and mid-span deflections were larger for an increasing bend-to-twist ratios, which was magnified further for an increasing skew angle. Moreover, minimal variation in bending moment magnitude was found at the supports and mid-span for increasing curvature for the curved slabs. The generic analytical procedures and finite-element model were compared against experimental results obtained from the study and results highlighted the success in modelling the structural behaviour of the skewed and curved UHPFRC slabs, and the high capacity and ductility shown in the experimental study emphasising the suitability of UHPFRC in the development of asymmetrical skewed and horizontally curved slabs.

Recommendations

Possible extensions explored include the interfacial bond action between screw anchors and UHPC/foam layers in the proposed box-celled composite panels. This and the embedment length are heavily influential as they control the failure mode of the composite box-celled panels under flexure. Another possible extension is the behaviour of the box-celled panels under combined actions and different support conditions. This includes testing the panel system under axial loads with varying eccentricity and varying loading types, such as evenly distributed pressure loading and impact loading. This is important as it can establish the viability of the panel as a barrier element, which experience both axial and flexural actions. It is also recommended to build larger-scale specimens to perform testing as continuous spanning one-way slabs. Recommendations for the GFRP include performing experimental tests on helically ribbed GFRP reinforcement specimens embedded in UHPFRC for numerous specimens. The variation of bond – slip behaviour is largely influenced by bar diameter and concrete cover conditions, however differing rib depths, widths, and spacing have a large effect on the bond – slip behaviour and requires adjustments to the proposed model to account for. Moreover, tests for varying embedment lengths and bar diameters should be performed to better verify the outcomes of the parametric study.

Recommendations for the skewed and curved slabs include expanding the experimental investigation for a large range of skew angles for the asymmetrical skewed slabs. This is important as it would better support the findings of the parametric, where critical skewed angles were identified but not verified by the appropriate test data. Furthermore, the specimens were considered small-scale and thus another recommendation is to test numerous mid- or full-scale specimens under homogenous pressure and impact loading.